Distribution Agreement

In presenting this thesis or dissertation as a partial fulfillment of the requirements for an advanced degree from Emory University, I hereby grant to Emory University and its agents the non-exclusive license to archive, make accessible, and display my thesis or dissertation in whole or in part in all forms of media, now or hereafter known, including display on the world wide web. I understand that I may select some access restrictions as part of the online submission of this thesis or dissertation. I retain all ownership rights to the copyright of the thesis or dissertation. I also retain the right to use in future works (such as articles or books) all or part of this thesis or dissertation.

Signature:

_____ _____

Chantelle Anfuso Date

Orientation and Vibrational Dynamics of Rhenium Bipyridyl CO_2-Reduction Catalysts on Model Electrode Surfaces

By

Chantelle Anfuso

Doctor of Philosophy

Chemistry

_____

Dr. Tianquan Lian
Advisor

_____

Dr. Michael C. Heaven
Committee Member

_____

Dr. Joel M. Bowman
Committee Member

Accepted:

_____

Lisa A. Tedesco, Ph.D.
Dean of the James T. Laney School of Graduate Studies

_____

Date

Orientation and Vibrational Dynamics of Rhenium Bipyridyl CO_2-Reduction Catalysts on Model Electrode Surfaces

By

Chantelle Anfuso

B.S., University of Georgia, Athens, GA, 2005

Advisor: Tianquan Lian, Ph.D.

An abstract of
A dissertation submitted to the Faculty of the
James T. Laney School of Graduate Studies of Emory University
in partial fulfillment of the requirements for the degree of
Doctor of Philosophy
in Chemistry
2012

Abstract

Orientation and Vibrational Dynamics of Rhenium Bipyridyl CO_2-Reduction Catalysts on Model Electrode Surfaces

By Chantelle Anfuso

The average molecular orientation of several rhenium bipyridyl CO_2-reduction catalysts adsorbed onto rutile single crystalline TiO_2 surfaces has been determined using vibrational sum frequency generation spectroscopy (VSFGS). The vibrational relaxation dynamics of two such catalysts were also investigated on two model electrode surfaces using time-resolved VSFGS techniques.

Polarization-resolved VSFGS was used to determine the average molecular orientation of ReC0A on TiO_2 (001), which was found to be within 0 – 22° from the surface normal. These results were supported by Density Functional Theory (DFT) calculations of optimized adsorption geometries. The influence of the substrate on the molecular organization was investigated by monitoring the degree of surface-induced ordering for ReC0A on TiO_2 (110). ReC0A exhibited a well-defined anisotropic arrangement following the C_{2v} symmetry of the TiO_2 (110) surface, in contrast to an isotropic distribution on the more symmetric (C_4) TiO_2 (001) surface. An average orientation angle of 28° was determined for the ReC0A/TiO_2 (110) system. The influence of lengthening the molecular linkers in a similar system was determined by investigating the adsorption geometries for the series ReCnA (n = 0 – 4) on TiO_2 (001) using phase-sensitive VSFGS and DFT calculations. The orientation angles were found to be closely correlated with the average lengths of the two linking anchoring groups, with the molecules tilting more towards the TiO_2 surface with increasing linker length.

Time-resolved VSFGS was used to investigate the vibrational relaxation dynamics of the totally symmetric CO stretch of ReC0A on TiO_2 (110) and ReC0-Au. Both systems exhibited bi-exponential relaxation from the $\upsilon = 1$ state consisting of an ultrafast (sub-picosecond) initial relaxation followed by complete recovery of the ground vibrational state within tens of picoseconds. The ultrafast decay is assigned to rapid υ-υ coupling between the three CO stretching modes, and the slower decay is assigned to vibrational population relaxation from the coupled CO modes. Although both systems exhibited similar ultrafast decay rates of the excited state, the excited a’(1) mode persisted for significantly longer in ReC0A on TiO_2 compared to ReC0-Au (τ_2 = 30.35 and 14.8 ps, respectively). This is attributed to electronic interactions between ReC0A and TiO_2 not present in the ReC0-Au system.

Orientation and Vibrational Dynamics of Rhenium Bipyridyl CO_2-Reduction Catalysts on Model Electrode Surfaces

By

Chantelle Anfuso

B.S., University of Georgia, Athens, GA, 2005

Advisor: Tianquan Lian, Ph.D.

A dissertation submitted to the Faculty of the
James T. Laney School of Graduate Studies of Emory University
in partial fulfillment of the requirements for the degree of
Doctor of Philosophy
in Chemistry
2012

Acknowledgements

First and foremost, I wish to extend my deepest thanks to my advisor, Dr. Tianquan Lian, for his help and support over the last six years. He has taught me to think critically and carefully about every problem, and to question myself frequently to ensure I understand each concept fully. His willingness and desire to constantly educate himself further have inspired me to try to do the same, and I cannot thank him enough for his scientific influence. I would also like to offer my sincere thanks to the members of my graduate committee, Dr. Michael Heaven and Dr. Joel Bowman, for their helpful advice and insightful questions during my graduate career. Both of them have helped me to reflect on problems from viewpoints I might not have otherwise considered, and I am deeply grateful to them both.

I thank my many colleagues over the years, for both their varied assistance in the laboratory and their friendship and company outside of it. In particular, I would like to thank Dr. David Stockwell and Dr. Baohua Wu for introducing me to the SFG project. Dr. David Stockwell also provided me with extensive training on the laser system and has been an invaluable help to me many times, even after his departure from Emory. He, Dr. Jier Huang, and Dr. Shengye Jin all happily welcomed me to the group and I will always appreciate their approachability and friendliness. Teddy Huang, with whom I began graduate school, has always proven himself a true friend and colleague and offered his assistance at every opportunity. Ye Yang provided me with semiconductor films on a number of occasions as well as interesting conversations on many afternoons in the office. Dr. William Rodríguez-Córdoba has been immensely helpful to me, particularly through his synthesis expertise. He has provided me with many samples without which I would not have been able to complete this work. Dr. Allen Ricks wrote innumerable Labview programs for the VSFGS data collection and analysis, and was responsible for the electronics design for the time-resolved VSFGS measurements. I am deeply grateful to him for his help and training, as well as for his camaraderie in and out of the lab. I would also like to thank my other group members Dr. Abbey Issac, Nianhui Song, Haiming Zhu, Dr. Zheng Liu, Dr. Xu Xiang, Dr. Beibei Ma, Kaifeng Wu, and Nannan

Han. I have enjoyed working with each of them in my time at Emory and will greatly miss their company.

My collaborators in the group of Dr. Victor Batista at Yale University deserve special thanks for their contributions to this work. Robert C. Snoeberger, III, Dequan Xiao, and Christian Negre performed Density Functional Theory calculations and geometry optimizations to complement several of the experimental VSFGS studies. This dissertation would not be complete without their collaboration. I truly appreciate all of their hard work and interesting scientific discussions over the past few years.

I thank my entire family for their unwavering support over the years. My grandparents, brother, and sister have always encouraged me in all of my endeavors. My father continually expressed great pride in all of my accomplishments, and I still feel his encouragement today. My mother ensured I had the best schooling possible in my formative years, and urged me to pursue my education further as an adult. I credit her for her endless assistance over the last 27 years, without which I would not be where I am today.

Finally, I would like to thank my wonderful husband, Jon, who was infinitely supportive and understanding throughout my graduate career. He has tolerated me through numerous annual reports, difficult days in the laboratory, and most recently as I prepared this dissertation. His enthusiastic support has proven invaluable during these stressful times. I thank him for his indulgence and for his boundless love and encouragement.

Table of Contents

List of Figures

Chapter 6

List of Tables

Chapter 1: Introduction

1.1. General Introduction

Atmospheric levels of carbon dioxide have steadily increased since the Industrial Revolution of the late 19th century. Although CO_2 is a nontoxic, naturally occurring substance, humans' heavy reliance on fossil fuel combustion as our primary energy source has led to an excess of approximately 3.9% CO_2 with respect to the natural ''carbon cycle''.[1] This excess atmospheric carbon dioxide has been implicated as a major contributing factor to global warming, presumably from its ability to absorb infrared radiation that is reflected off of the Earth from the sun, effectively trapping excess heat.[2] Unfortunately, the continued worldwide use of fossil fuels guarantees the sustained emission of CO_2 into the atmosphere in large quantities. At the same time, the limited natural resources of fossil fuels necessitate a new source of energy for automobiles, electricity generation, and countless other applications. A cyclical recovery system (i.e. CO_2 + energy → fuel → CO_2 + energy, etc.) that utilizes CO_2 for the production of liquid fuels thus represents an ideal method for reducing the concentration of a deleterious greenhouse gas while simultaneously providing a new source of renewable energy.[3] New catalytic materials might therefore provide viable solutions to the global carbon balance by both recycling CO_2 and producing carbon neutral renewable fuels.[3-6]

To this end, the development and structural characterization of catalytic materials for selective reduction of carbon dioxide to other C_1 compounds has been extensively investigated.[1-3,5,7-10] To date, there are three primary classes of synthetic CO_2 reduction catalysts: metal complexes with (1) macrocyclic ligands, (2) phosphine ligands, and (3)

bipyridine ligands.[5] Of these, metal complexes with modified bipyridine ligands have shown the most promising catalytic efficiencies and selectivity. In particular, several rhenium bipyridyl complexes have been developed and explored for catalytic reduction of CO_2 to CO and formate.[4,11-17] Numerous studies have additionally reported enhanced catalytic turnover when these complexes are immobilized on semiconductor or metal electrodes.[18-22] The covalent attachment of these electrocatalysts on electrodes has yet to be characterized at the molecular level, despite the fact that the orientation and binding of catalysts to electrode surfaces may affect the efficiency of electron transfer and electrocatalytic reduction.[23-27] It is therefore of great fundamental and practical interest to elucidate the average molecular orientation in these adsorbate-electrode systems in order to gain a more complete understanding of the relevant electron transfer and electrocatalytic processes.

These processes are also intricately related to the rates and mechanisms of vibrational energy flow for adsorbates on electrodes.[28] In particular, the adsorption and reaction of catalysts at electrodes is directly related to vibrational energy relaxation and equilibration at the electrode surface.[29] Vibrational energy dynamics can differ significantly between molecules in solution and at the electrode surface due to the potential for coupling with the electrode in the latter case; this can subsequently stabilize or destabilize the catalytic intermediates towards reaction. Additionally, the dynamics (and catalytic activity) can vary depending on the surface and the nature of the adsorbate-substrate coupling. This is dependent on a number of parameters, including the nature of the substrate electronic structure. Metals, for instance, exhibit a continuum of electronic states, so that conduction electrons may be excited from just below to just above the

Fermi level by an arbitrarily small amount of energy in a process known as electron-hole pair (EHP) excitation.[30] Semiconductors, on the other hand, have larger, more discrete bandgaps, inhibiting this relaxation pathway. Numerous studies have focused on the flow of vibrational energy for adsorbates on surfaces and found that several relaxation pathways exist, including energy transfer to other internal vibrational modes of the adsorbate, to other nearby adsorbates, and to the surface, through either coupling to substrate phonons or through the excitation of substrate electron-hole pairs.[29,31] A detailed study of the vibrational relaxation of these complexes adsorbed on semiconductor and metal surfaces may shed light on the complicated reaction dynamics in these electrocatalytic systems.

Unfortunately, monitoring molecular structure and dynamics at interfaces has proven to be experimentally challenging. Many surface-specific techniques exist that are based on particle scattering, but these typically must be performed under high vacuum conditions, limiting their applicability. While traditional optical techniques may be applied to any interface accessible by light, they are not surface-specific, so that the response from interfacial molecules is masked by bulk contributions. However, second-order optical techniques such as sum frequency generation (SFG) are forbidden in media with inversion symmetry under the electric dipole approximation, but allowed at the interface where the inversion symmetry is necessarily broken.[32] They thus combine all the advantages typical of optical techniques with interface specificity. Similar to other optical techniques, sum frequency generation is also easily adaptable to performing time-resolved measurements.[28] For these reasons, vibrational sum frequency generation

spectroscopy (VSFGS) has been recognized in recent years as a useful technique for monitoring molecular structure and vibrational dynamics at interfaces.[33-35]

1.2. Vibrational Sum Frequency Generation Spectroscopy

1.2.1. General Description

Vibrational sum frequency generation spectroscopy (VSFGS) is a nonlinear optical technique capable of measuring surface-specific vibrational spectra of molecules at interfaces.[32-36] A second-order optical technique, it is forbidden in media with inversion symmetry but allowed at interfaces where the inversion symmetry is necessarily broken. In a typical infrared-visible SFG experiment, two fundamental laser beams of frequency ω_{IR} and ω_{vis} are spatially and temporally overlapped at a surface, producing a third coherent optical field at the sum frequency ω_{SF} ($\omega_{SF} = \omega_{IR} + \omega_{vis}$); this process is illustrated schematically in Figure 1.1. The visible beam is usually held at a fixed narrowband frequency, while the infrared beam is broadband and/or tunable. In the broadband configuration, the resulting VSFGS spectral resolution is determined by the bandwidth of the visible field, while in the tunable (narrowband) configuration, the spectral resolution is determined by the bandwidth of the infrared field. The efficiency of the SFG process is enhanced when ω_{IR} corresponds to a vibrational resonance of the interfacial molecule, yielding a vibrational SFG spectrum; however, a vibrational mode must be both IR and Raman active in order to be SFG active.

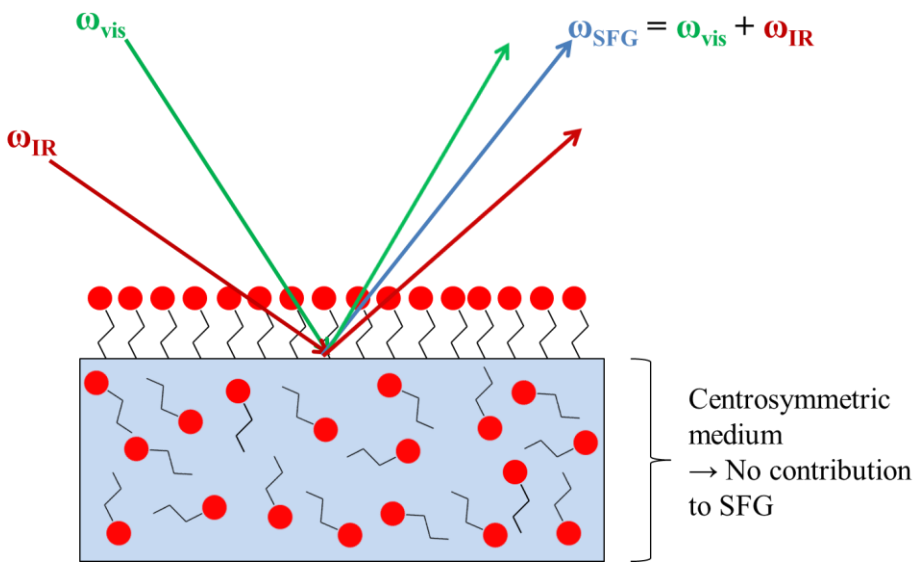

Figure 1.1. Geometry of a sum frequency generation experiment. Two beams of frequency ω_{IR} and ω_{vis} are overlapped at a surface, producing a third coherent optical field at the sum frequency ω_{SF} ($\omega_{SF} = \omega_{IR} + \omega_{vis}$). The SFG process is forbidden in media with inversion symmetry but allowed at interfaces where the inversion symmetry is necessarily broken.

One interesting property of VSFGS is its ability to determine the average conformation of molecules at an interface. Since SFG is a coherent process, the generated SF wave has a specific direction, amplitude, phase, and polarization associated with it. For an ordered layer of molecules on a surface, the last three properties are related to the response of the SF-active molecular vibrations with respect to the polarization of ω_{vis} and ω_{IR}. By monitoring the VSFGS response as a function of the fundamental and generated polarizations, the projection of the vibrational transition moment on the laboratory axis – and thus the average molecular orientation – can be determined. Additional information can be gleaned by combining the results of VSFGS with Density Functional Theory

(DFT) calculations in order to screen calculated adsorption geometries. The molecular orientation at the semiconductor surface can thus be obtained via this synergy of experiment and theory.

Although primarily used for static vibrational spectroscopy, the VSFGS technique has also been extended to include time-resolved measurements.[28,36-48] Time-resolved VSFGS (TR-VSFGS) techniques can be used on the long time scale (ms to sec) to monitor the kinetics of surface reactions and catalysis, and used on the short time scale (fs to μs) to monitor ultrafast interfacial dynamics such as surface vibrational excitations and relaxations. For kinetic studies, VSFGS spectra are typically monitored on a timescale of milliseconds or seconds as some external force, such as a bias voltage or change in pressure or temperature, is exerted on the system.[34,36,39-42,46,47,49] Dynamics studies, on the other hand, examine the evolution of a system after the application of an ultrashort laser (pump) pulse, which disturbs the equilibrium state of the system via a chemical transformation, energy transfer, or electronic/vibrational excitation.[28,36-39,41-45,48,50-58] These experiments are typically monitored on the femtosecond to microsecond time scale.

1.2.2. Historical Background

Although *vibrational* sum frequency generation was not performed until many years later, a form of electronic sum frequency generation, called second harmonic generation, was first demonstrated by Franken *et al.* in 1961 from a quartz substrate.[59] Second harmonic generation (SHG) is a particular form of SFG where $\omega_1 = \omega_2$, so that $\omega_{SF} = \omega_{SH} = 2\omega_1$. In this case, ω_1 and/or ω_{SH} is chosen to be resonant with an electronic

transition of the substrate or interfacial molecules. This technique requires only a single input frequency and was demonstrated shortly after the advent of the ruby laser in 1960. One year after Franken demonstrated SHG experimentally, Armstrong *et al.* published their now classical work which provided a general theoretical foundation for wave mixing in nonlinear media.[60] Over the next two decades, numerous SHG experiments were performed on metal and semiconductor surfaces in an attempt to confirm theoretical predictions and improve understanding of surface nonlinearity.[61-63]

It was not until the early 1980s that the possibility of employing SHG as a molecular surface probe was fully appreciated. A 1981 study by Chen *et al.* demonstrated that SHG was also capable of monitoring the adsorption and desorption of molecules on a roughened Ag electrode in an electrochemical cell.[64] Following this work, the focus of many SHG experiments shifted from the substrate itself to the adsorbed interfacial molecules. Subsequent experiments by numerous groups illustrated the wide-ranging applications of SHG, including but not limited to: monitoring adsorption and desorption kinetics at interfaces;[65-68] providing spectral and orientational information for organic monolayers and liquid crystals on surfaces;[69-72] and characterizing the symmetry of anisotropic crystalline surfaces.[73,74] These experiments were also used to refine the theory of SHG according to new observations for different systems.

The advent of using SHG as a molecular probe further pushed interest in the development of vibrational sum frequency generation spectroscopy (VSFGS). Although it requires a more complex experimental arrangement compared to SHG, the vibrational spectra VSFGS provides yield significantly more information about interfacial molecules. While SHG is typically used to access broad, often overlapping electronic transitions,

VSFGS can be used to probe discrete vibrations in order to focus on specific functional groups of the surface molecules. The conformation of multiple functional groups can be investigated in order to deduce an absolute orientation of molecules at the interface. Additionally, the ability to monitor specific molecular vibrations in time-resolved VSFGS studies eliminates the ambiguity in the transient signal from which SHG studies can suffer.

Although the fundamental theory of VSFGS had been outlined in the seminal 1962 paper by Armstrong, it was not yet experimentally demonstrated by the mid-1980s. This was primarily due to the need for tunable infrared laser sources, which were not commercially available at the time. In 1986, Shen *et al.* recorded the first sum frequency spectrum of coumarin adsorbed on fused silica, though this experiment only explored resonances in the near-IR range.[75] Vibrational SFGS was demonstrated less than a year later when Shen *et al.* obtained spectra from methanol on glass and from pentadecanoic acid on both glass and water.[76] The same year, Harris and coworkers used VSFGS to examine molecular monolayers on semiconductor and metal surfaces, namely octadecanethiol (ODT) on gold and Langmuir-Blodgett films of cadmium arachidate on silver and germanium.[77] These pioneering studies established VSFGS as a viable surface probe, and over the next two decades this technique was applied to a wide variety of interfaces, including solid/adsorbate, solid/liquid, liquid/vapor and liquid/liquid systems, as has been detailed in a number of excellent review articles.[62,63,78-86]

As tunable infrared laser sources became more readily available, the VSFGS technique became accessible to a greater number of research groups. These early tunable IR sources produced narrowband, picosecond pulses, so that procuring a VSFGS

spectrum consisted of scanning across the region of interest and recording the signal for each wavelength. This time-consuming procedure suffered from fluctuations in pulse power, duration, and spectral width, leading to poor signal-to-noise (SNR) ratios for many systems. However, in 1998, Stephenson *et al.* demonstrated a novel procedure for VSFGS in which a femtosecond broadband IR source was combined with a picosecond narrowband visible source.[87] This breakthrough allows for the simultaneous measurement of multiple vibrational modes over hundreds of wavenumbers in a single broadband (BB) VSFGS spectrum, greatly reducing data acquisition time. Additionally, since an entire VSFGS spectrum is generated with each laser shot, spectra are far less sensitive to laser fluctuations, leading to increased SNR compared to picosecond narrowband IR sources.

Although initial studies concentrated on deducing molecular orientation, time-resolved VSFGS was quickly recognized as a powerful tool for examining surface-specific catalysis, kinetics, and energy transfer, among other applications. Until recently, most dynamic TR-VSFGS studies were based on narrowband IR sources with picosecond time resolution, limiting their applicability to systems exhibiting picosecond molecular dynamics.[50,51,53,55,88-98] As described above, the use of narrowband IR pulses also means that only a single vibrational band can be probed at one time, prohibiting the simultaneous monitoring of intermediate excited states or necessitating numerous experimental runs in order to cover multiple wavelength regions. The recent advent of ultrashort ($\leq$ 150 fs) amplified pulses has opened the door to performing broadband time-resolved VSFGS (BB-TR-VSFGS) on the femtosecond time scale, making it possible to monitor ultrafast molecular dynamics at surfaces. Additionally, the ability to simultaneously monitor spectral signatures of the ground, excited, and/or transient

species is extremely instructive when deducing mechanisms of energy transfer, vibrational relaxation, etc. Several such studies have now been performed, elucidating femtosecond dynamics of interfacial systems.[28,45,48,54,56-58,99]

1.3. Catalytic Reduction of CO_2 via Transition Metal Complexes

1.3.1. General Description

The conversion of carbon dioxide into usable liquids fuels or their precursors via electrochemical reduction represents a sustainable method of utilizing CO_2 while simultaneously providing a new fuel source.[3,4] However, the direct reduction of CO_2 to form $CO_2^{\bullet-}$ is highly energetically unfavorable, having a formal reduction potential of E^0 = -1.90 V (*versus* NHE at 25°C, 1 atmosphere pressure, and 1 M concentration for the other solutes), primarily due to the large reorganization energy required to transform from the linear molecule to the bent radical anion.[5] For this reason, proton-assisted multi-electron transfer is generally regarded as a more favorable pathway to efficient CO_2 reduction. Several such processes and their formal reduction potentials are outlined in Table 1.1.[10] Although CO_2 can be directly reduced at metal electrodes, this method suffers from poor selectively, resulting in a myriad of products that are generally not useful without refinement or separation. A system that reduces CO_2 to one specific product that can be used as a liquid fuel or its precursor is thus highly desirable. As such, many research groups have focused on the development and characterization of catalysts and/or redox mediators that may selectively drive one of the reactions shown in Table 1.1.[1-3,5,7-10]

Table 1.1. CO_2 reduction pathways and their formal reduction potentials.[10]

Reaction	E^0 (V) vs. NHE
$CO_2 + 2H^+ + 2e^- \rightarrow CO + H_2O$	-0.53
$CO_2 + 2H^+ + 2e^- \rightarrow HCO_2H$	-0.61
$CO_2 + 4H^+ + 4e^- \rightarrow HCHO + H_2O$	-0.48
$CO_2 + 6H^+ + 6e^- \rightarrow CH_3OH + H_2O$	-0.38
$CO_2 + 8H^+ + 8e^- \rightarrow CH_4 + 2H_2O$	-0.24
$CO_2 + e^- \rightarrow CO_2^{\bullet -}$	-1.90

To this end, numerous transition-metal catalysts based on Ru, Re, Co, Cu, and Ni, among others, have been studied. One particularly interesting subset of these consists of transition-metal complexes with modified bipyridine ligands. These compounds show great promise as potential highly-selective electrocatalysts due to their multiple accessible redox states, which have been shown to promote proton-assisted multi-electron transfer. Additionally, it is possible to systematically tune the formal reduction potentials of these catalysts by modifying the bipyridine substituents in order to better match the potential required for CO_2 reduction. Several of these have also shown potential as photoelectrocatalysts that are capable of coupling the dark catalytic CO_2 reduction process with a light harvesting mechanism that generates the necessary redox equivalents. Transition-metal complexes are ideal for this application, owing to their broad visible absorption spectra, long-lived excited states, and ability to promote the activation of small molecules. These complexes thus act as both photosensitizers and multi-electron

redox catalysts capable of mediating the reduction of CO_2 using solar power as an energy source.

1.3.2. Rhenium Bipyridyl CO_2 Reduction Catalysts

Several tricarbonyl rhenium(I) complexes with modified bipyridine ligands have been investigated for their ability to photocatalytically and/or electrocatalytically reduce CO_2. These complexes are usually denoted $Re(L)(CO)_3X$ [L = 2,2'-bipyridine-4,4'-R], where X is typically a halide and R = H, CH_3, COOH, or some other small functional group. Tricarbonyl rhenium-based catalysts have thus far shown the highest efficiency of the transition metal-bipyridyl complexes and as such have received considerable attention.

Hawecker and coworkers first reported the photochemical reduction of CO_2 to CO and formic acid by $Re(bipy)(CO)_3Cl$ [bipy = 2,2'-bipyridine] in 1983.[100] One year later, they demonstrated the electrocatalytic selective reduction of CO_2 to CO, quoting a selective reduction potential of -1.49 V vs. SCE using a 9:1 DMF–H_2O solution.[11] The system exhibited a marked solvent dependency, where the selectivity for CO was reduced with increasing water concentration. Additionally, under an argon atmosphere, molecular hydrogen was the only reduction product. Overall, $Re(bipy)(CO)_3Cl$ exhibited high current efficiencies, excellent selectively (with correct solvent choice), and operated at moderate overpotentials, but was limited by its low turn-over frequency (TOF, 21.4 h^{-1}).

Since Hawecker's initial report, numerous groups have systematically evaluated the photo- and/or electrocatalytic properties of $Re(L)(CO)_3X$ complexes. Many of these studies concentrated on elucidating the various mechanisms of CO_2 reduction for

$Re(bipy)(CO)_3L$ with different ligands (L = halide, H, CH_3, etc.), or with modified bipyridine ligands such as 4,4′-dimethyl-2,2′-bipyridine (dmbpy). Meyer *et al.* investigated the Re(bipy)(CO)Cl complex using cyclic voltammetry (CV) and concluded that CO_2 can be reduced to CO and CO_3^{2-} via a one-electron pathway [i.e. by Re(bipy)(CO)·] or to CO via a two-electron pathway [i.e. by $Re(bipy)(CO)^-$] depending on the applied potential (-1.5 V or -1.8 V vs. SCE, respectively), both with high efficiencies.[101] A subsequent kinetic study on $Re(bipy)(CO)_3H$ led them to conclude that the reaction proceeds via CO_2 insertion into the metal-hydride bond, with the hydride transferring to CO_2.[102] Like Hawecker, they observed a dramatic solvent effect, which they interpreted as evidence for a significant degree of charge separation during the hydride transfer, whereby the polar transition state is stabilized by increasingly polar solvents despite the relatively nonpolar ground state.

Turner *et al.* investigated the electrocatalytic ability of $[Re(CO)_3(bipy)L]^n$ (n = 0, L = Cl^-, $CF_3SO_3^-$; n = +1, L = CH_3CN, $P(OEt)_3$) and determined that the reduction mechanism was highly dependent on both the ligand L and any modifications to the bipyridine ligand.[103] They proposed that ligand dissociation must take place previous to CO_2 reduction; depending on the ligand affinity, this may require one or two electrons to produce the $Re(CO)_3(bipy)$ radical or anion, respectively. They also suggested that coordination of solvent molecules on the Re center may precede the insertion of CO_2.

Kubiak *et al.* investigated the effect of varying the 4',4'-substituents to increase the bipyridyl pKa (R = CO_2H < H < Me < Bu^t < OCH_3) and found that this resulted in increasingly negative reduction potentials (-1.72 to -1.86 V).[104] Of these, the complex with R = Bu^t showed the highest catalytic efficiency, with the reduction wave at -1.83 V

exhibiting a large catalytic enhancement compared to other complexes under a CO_2 atmosphere. They attributed this to the optimum stabilization of the Re(0) radical due to the electron donating properties of the *tert*-butyl groups.

Despite this extensive research, the exact mechanism of CO_2 reduction is still unclear and has been discussed extensively in numerous articles.[3,101-103,105,106] Formate production is now reasonably understood, and is believed to occur through a multi-step process initiated by loss of the halide. Most notable is the step in which CO_2 inserts itself into a Re-H bond, after which formate is exchanged for the original halide, releasing the formate ion and regenerating the catalyst. The mechanism of carbon monoxide formation is still under debate, but is has become clear that solvent ligand coordination and the participation of a second $Re(L)(CO)_3X$ complex are important factors. There is also a well-documented undesirable side reaction of $Re(L)(CO)_3X$, wherein,the Re-H bond undergoes ligand exchange to produce hydrogen gas and the regenerated complex without reducing CO_2. The amount of hydrogen gas produced by a particular $Re(L)(CO)_3X$ complex can thus be used as a measure of its selectivity.

To date, rhenium tricarbonyl complexes have shown to be an extremely promising class of transition metal electrocatalysts and photocatalysts. They demonstrate the ability to reduce CO_2 to both carbon monoxide (CO) and formate ($HCOO^-$) with high quantum yields and selectively, as evidenced by high yields of specific products and little to no hydrogen gas production. Although numerous studies have focused on elucidating the fundamental properties of these complexes, these are typically confined to bulk systems or theoretical investigations. However, these electrocatalytic processes typically occur at the metal and semiconductor electrodes rather than in solution.[22,107] Additionally, several

heterogeneous catalytic systems have been prepared by incorporating these complexes into polymer films deposited onto electrodes.[18-21,108] These systems have shown enhanced catalytic turnover compared to related homogeneous $Re(L)(CO)_3X$ catalysts in solution. Knowledge of the covalent attachment of these electrocatalysts on electrodes may aid in a more complete understanding of their electrocatalytic behavior, as the orientation and binding of catalysts to electrode surfaces may affect the efficiency of electron transfer and electrocatalytic reduction.[23-27] These processes are also intricately related to the rates and mechanisms of vibrational energy flow for catalysts at electrodes. A technique capable of monitoring the structure and vibrational dynamics of these systems is thus highly desired.

As discussed above, vibrational sum frequency generation spectroscopy (VSFGS) is an ideal tool for these measurements. At the same time, $Re(L)(CO)_3X$ represents an ideal system to be studied by VSFGS. These complexes contain three carbonyl ligands, which exhibit three CO stretching modes: two symmetric stretches denoted a'(1) and a'(2) at 2027 cm^{-1} and 1890 cm^{-1}, respectively, and an asymmetric stretch denoted a" at 1926 cm^{-1}.[109] These vibrational modes exhibit strong Raman and IR activity, indicating they should be strongly SFG active as well. Additionally, their transition dipoles are all roughly orthogonal to each other in the molecular *xyz* frame, so measuring their projection onto the laboratory XYZ frame should allow for the unequivocal determination of the average molecular orientation. These vibrational modes have also been used previously to monitor the molecular excited and oxidized state dynamics using standard time-resolved optical techniques.[110-112110-112] Time-resolved VSFGS should thus be able to monitor the excited vibrational dynamics of these complexes at an interface.

Since CO_2 reduction is known to occur at the rhenium center, monitoring the vibrational dynamics of the carbonyl stretches should most closely approximate the vibrational energy flow during the catalytic process.

1.4. Summary and Overview

Vibrational sum frequency generation spectroscopy (VSFGS) is an important surface tool capable of elucidating a molecular-level picture of adsorbate-substrate systems. In this work, it is used to monitor the structure and dynamics of a family of rhenium bipyridyl CO_2 reduction catalysts on a model semiconductor, single crystalline TiO_2, and a model Au electrode. First, the ability to selectively prepare adsorbate-semiconductor systems with a predetermined ordering in and out of the surface plane is investigated. Specifically, the extent of in-plane molecular ordering induced by the semiconductor surface symmetry is studied by determining the molecular orientation of a single rhenium bipyridyl complex on two TiO_2 single crystalline surfaces of different symmetries (C_4 vs. C_{2v}). The dependence of the out-of-plane molecular tilt angle on the length of the adsorbate anchoring groups is also investigated by determining the molecular orientation for a series of rhenium bipyridyl complexes adsorbed on a single crystal TiO_2 surface. Finally, the ultrafast vibrational dynamics of two rhenium bipyridyl complexes are examined on metal and semiconductor surfaces in order to gain insight into the mechanism of vibrational energy flow within these model electrocatalyst-electrode systems.

The rest of this work will be organized as follows. Chapter 2 introduces the basic theoretical description of vibrational sum frequency generation spectroscopy, including a

brief description of how molecular orientation is determined from VSFGS measurements. Chapter 3 summarizes the sample preparation methods and gives a detailed description of the experimental techniques. Chapter 4 examines the orientation of a rhenium bipyridyl CO_2 reduction catalyst (ReC0A) on single crystalline TiO_2 (001) and serves as the precursor for the following two chapters. Chapter 5 compares the surface-induced ordering and molecular orientation of ReC0A on two TiO_2 single crystalline surfaces of different symmetries, (001) and (110), while Chapter 6 compares the average orientation of a series of rhenium bipyridyl complexes with anchoring groups of different lengths (ReCnA) on single crystalline TiO_2 (110). Finally, Chapter 7 investigates and compares the vibrational relaxation dynamics of two rhenium bipyridyl complexes adsorbed on gold and single crystalline TiO_2 surfaces.

1.5. References

(1) Mikkelsen, M.; Jorgensen, M.; Krebs, F. C. *Energ Environ Sci* **2010**, *3*, 43.

(2) Spinner, N. S.; Vega, J. A.; Mustain, W. E. *Catal Sci Technol* **2012**, *2*, 19.

(3) Morris, A. J.; Meyer, G. J.; Fujita, E. *Accounts of Chemical Research* **2009**, *42*, 1983.

(4) Fujita, E. H., Y.; Kita, S.; Brunschwig, B. S. In *7th International Conference on Carbon Dioxide Utilization*; Sang-Eon Park, J.-S. C., Kyu-Wan Lee, Ed.; Elsevier: Seoul, Korea, 2004.

(5) Benson, E. E.; Kubiak, C. P.; Sathrum, A. J.; Smieja, J. M. *Chem Soc Rev* **2009**, *38*, 89.

(6) Whipple, D. T.; Kenis, P. J. A. *J Phys Chem Lett* **2010**, *1*, 3451.

(7) Balazs, G. B.; Anson, F. C. *Journal of Electroanalytical Chemistry* **1993**, *361*, 149.

(8) Raebiger, J. W.; Turner, J. W.; Noll, B. C.; Curtis, C. J.; Miedaner, A.; Cox, B.; DuBois, D. L. *Organometallics* **2006**, *25*, 3345.

(9) Olah, G. A.; Goeppert, A.; Prakash, G. K. S. *J Org Chem* **2009**, *74*, 487.

(10) Finn, C.; Schnittger, S.; Yellowlees, L. J.; Love, J. B. *Chem Commun* **2012**, *48*, 1392.

(11) Hawecker, J.; Lehn, J. M.; Ziessel, R. *J Chem Soc Chem Comm* **1984**, 328.

(12) Hawecker, J.; Lehn, J. M.; Ziessel, R. *Helv Chim Acta* **1986**, *69*, 1990.

(13) Juris, A.; Campagna, S.; Bidd, I.; Lehn, J. M.; Ziessel, R. *Inorganic Chemistry* **1988**, *27*, 4007.

(14) Yam, V. W. W.; Lau, V. C. Y.; Cheung, K. K. *Organometallics* **1995**, *14*, 2749.

(15) Hayashi, Y.; Kita, S.; Brunschwig, B. S.; Fujita, E. *Journal of the American Chemical Society* **2003**, *125*, 11976.

(16) Fujita, E.; Muckerman, J. T. *Inorg Chem* **2004**, *43*, 7636.

(17) Takeda, H.; Koike, K.; Inoue, H.; Ishitani, O. *Journal of the American Chemical Society* **2008**, *130*, 2023.

(18) Otoole, T. R.; Margerum, L. D.; Westmoreland, T. D.; Vining, W. J.; Murray, R. W.; Meyer, T. J. *J Chem Soc Chem Comm* **1985**, 1416.

(19) Christensen, P.; Hamnett, A.; Muir, A. V. G.; Timney, J. A.; Higgins, S. *Journal of the Chemical Society-Faraday Transactions* **1994**, *90*, 459.

(20) Cecchet, F.; Alebbi, M.; Bignozzi, C. A.; Paolucci, F. *Inorganica Chimica Acta* **2006**, *359*, 3871.

(21) Cheung, K. C.; Guo, P.; So, M. H.; Lee, L. Y. S.; Ho, K. P.; Wong, W. L.; Lee, K. H.; Wong, W. T.; Zhou, Z. Y.; Wong, K. Y. *J Organomet Chem* **2009**, *694*, 2842.

(22) Kumar, B.; Smieja, J. M.; Kubiak, C. P. *Journal of Physical Chemistry C* **2010**, *114*, 14220.

(23) O'Regan, B.; Gratzel, M. *Nature* **1991**, *353*, 737.

(24) Kamat, P. V.; Meisel, D. *Current Opinion in Colloid & Interface Science* **2002**, *7*, 282.

(25) Adams, D. M.; Brus, L.; Chidsey, C. E. D.; Creager, S.; Creutz, C.; Kagan, C. R.; Kamat, P. V.; Lieberman, M.; Lindsay, S.; Marcus, R. A.; Metzger, R. M.; Michel-Beyerle, M. E.; Miller, J. R.; Newton, M. D.; Rolison, D. R.; Sankey, O.; Schanze, K. S.; Yardley, J.; Zhu, X. *Journal of Physical Chemistry B* **2003**, *107*, 6668.

(26) Gratzel, M. *MRS Bulletin* **2005**, *30*, 23.

(27) Prezhdo, O. V.; Duncan, W. R.; Prezhdo, V. V. *Accounts of Chemical Research* **2008**, *41*, 339.

(28) Arnolds, H.; Bonn, M. *Surf Sci Rep* **2010**, *65*, 45.

(29) Tully, J. C. *Annual Review of Physical Chemistry* **2000**, *51*, 153.

(30) Gadzuk, J. W. *Physical Review B* **1981**, *24*, 1651.

(31) Wodtke, A. M.; Tully, J. C.; Auerbach, D. J. *International Reviews in Physical Chemistry* **2004**, *23*, 513.

(32) Shen, Y. R. *The principles of nonlinear optics*; J. Wiley: New York, 1984.

(33) Zhuang, X.; Miranda, P. B.; Kim, D.; Shen, Y. R. *Physical Review B* **1999**, *59*, 12632.

(34) Lambert, A. G.; Davies, P. B.; Neivandt, D. J. *Applied Spectroscopy Reviews* **2005**, *40*, 103.

(35) Rao, Y.; Comstock, M.; Eisenthal, K. B. *Journal of Physical Chemistry B* **2006**, *110*, 1727.

(36) Wang, H. F.; Gan, W.; Lu, R.; Rao, Y.; Wu, B. H. *International Reviews in Physical Chemistry* **2005**, *24*, 191.

(37) Harris, A. L.; Rothberg, L. *Journal of Chemical Physics* **1991**, *94*, 2449.

(38) Kato, T.; Hayashi, M.; Villaeys, A. A.; Lin, S. H. *Physical Review A* **1997**, *56*, 980.

(39) Tadjeddine, A. *Surf Rev Lett* **2000**, *7*, 423.

(40) Buck, M.; Himmelhaus, M. *J Vac Sci Technol A* **2001**, *19*, 2717.

(41) Raschke, M. B.; Shen, Y. R. *Curr Opin Solid St M* **2004**, *8*, 343.

(42) Guyot-Sionnest, P. *Surface Science* **2005**, *585*, 1.

(43) McGuire, J. A.; Shen, Y. R. *Science* **2006**, *313*, 1945.

(44) Hayashi, M.; Shiu, Y. J.; Liang, K. K.; Lin, S. H.; Shen, Y. R. *Journal of Physical Chemistry A* **2007**, *111*, 9062.

(45) Ghosh, A.; Smits, M.; Bredenbeck, J.; Dijkhuizen, N.; Bonn, M. *Rev Sci Instrum* **2008**, *79*.

(46) Geiger, F. M. *Annual Review of Physical Chemistry* **2009**, *60*, 61.

(47) Ye, S.; Osawa, M. *Chem Lett* **2009**, *38*, 386.

(48) Zhang, Z.; Piatkowski, L.; Bakker, H. J.; Bonn, M. *Nat Chem* **2011**, *3*, 888.

(49) Chen, Z.; Ward, R.; Tian, Y.; Malizia, F.; Gracias, D. H.; Shen, Y. R.; Somorjai, G. A. *J Biomed Mater Res* **2002**, *62*, 254.

(50) Harris, A. L.; Levinos, N. J. *Journal of Chemical Physics* **1989**, *90*, 3878.

(51) Matranga, C.; Guyot-Sionnest, P. *J. Chem. Phys.* **2000**, *112*, 7615.

(52) Hess, C.; Wolf, M.; Roke, S.; Bonn, M. *Surface Science* **2002**, *502*, 304.

(53) Matranga, C.; Wehrenberg, B. L.; Guyot-Sionnest, P. *J. Phys. Chem. B* **2002**, *106*, 8172.

(54) Eftekhari-Bafrooei, A.; Borguet, E. *Journal of the American Chemical Society* **2009**, *131*, 12034.

(55) Han, X.; Balgar, T.; Hasselbrink, E. *Journal of Chemical Physics* **2009**, *130*.

(56) Rao, Y.; Turro, N. J.; Eisenthal, K. B. *Journal of Physical Chemistry C* **2010**, *114*, 17703.

(57) Vanselous, H.; Dewan, S.; Isaienko, O.; Borguet, E. *Abstracts of Papers of the American Chemical Society* **2011**, *242*.

(58) Nihonyanagi, S.; Eftekhari-Bafrooei, A.; Borguet, E. *Journal of Chemical Physics* **2011**, *134*.

(59) Franken, P. A.; Weinreich, G.; Peters, C. W.; Hill, A. E. *Phys Rev Lett* **1961**, *7*, 118.

(60) Armstrong, J. A.; Bloembergen, N.; Ducuing, J.; Pershan, P. S. *Phys Rev* **1962**, *127*, 1918.

(61) Shen, Y. R. *Annual Review of Physical Chemistry* **1989**, *40*, 327.

(62) Bloembergen, N. *Appl Phys B-Lasers O* **1999**, *68*, 289.

(63) Shen, Y. R. *Ieee J Sel Top Quant* **2000**, *6*, 1375.

(64) Chen, C. K.; Heinz, T. F.; Ricard, D.; Shen, Y. R. *Phys Rev Lett* **1981**, *46*, 1010.

(65) Zhu, X. D.; Shen, Y. R.; Carr, R. *Surface Science* **1985**, *163*, 114.

(66) Tom, H. W. K.; Mate, C. M.; Zhu, X. D.; Crowell, J. E.; Shen, Y. R.; Somorjai, G. A. *Surface Science* **1986**, *172*, 466.

(67) Tom, H. W. K.; Zhu, X. D.; Shen, Y. R.; Somorjai, G. A. *Surface Science* **1986**, *167*, 167.

(68) Hicks, J. M.; Urbach, L. E.; Plummer, E. W.; Dai, H. L. *Phys Rev Lett* **1988**, *61*, 2588.

(69) Heinz, T. F.; Tom, H. W. K.; Shen, Y. R. *Physical Review A* **1983**, *28*, 1883.

(70) Kemnitz, K.; Bhattacharyya, K.; Hicks, J. M.; Pinto, G. R.; Eisenthal, K. B.; Heinz, T. F. *Chemical Physics Letters* **1986**, *131*, 285.

(71) Goh, M. C.; Hicks, J. M.; Kemnitz, K.; Pinto, G. R.; Bhattacharyya, K.; Heinz, T. F.; Eisenthal, K. B. *Journal of Physical Chemistry* **1988**, *92*, 5074.

(72) Chen, W.; Feller, M. B.; Shen, Y. R. *Phys Rev Lett* **1989**, *63*, 2665.

(73) Tom, H. W. K.; Heinz, T. F.; Shen, Y. R. *Phys Rev Lett* **1983**, *51*, 1983.

(74) Heinz, T. F.; Loy, M. M. T.; Thompson, W. A. *Phys Rev Lett* **1985**, *54*, 63.

(75) Zhu, X. D.; Suhr, H.; Shen, Y. R. *Physical Review B* **1987**, *35*, 3047.

(76) Hunt, J. H.; Guyotsionnest, P.; Shen, Y. R. *Chemical Physics Letters* **1987**, *133*, 189.

(77) Harris, A. L.; Chidsey, C. E. D.; Levinos, N. J.; Loiacono, D. N. *Chemical Physics Letters* **1987**, *141*, 350.

(78) Eisenthal, K. B. *Annual Review of Physical Chemistry* **1992**, *43*, 627.

(79) Eisenthal, K. B. *Accounts of Chemical Research* **1993**, *26*, 636.

(80) Bain, C. D. *Journal of the Chemical Society, Faraday Transactions* **1995**, *91*, 1281.

(81) Eisenthal, K. B. *Chemical Reviews* **1996**, *96*, 1343.

(82) Shen, Y. R. *Solid State Commun* **1997**, *102*, 221.

(83) Miranda, P. B.; Shen, Y. R. *Journal of Physical Chemistry B* **1999**, *103*, 3292.

(84) Richmond, G. L. *Annu. Rev. Phys. Chem.* **2001**, *52*, 357.

(85) Vidal, F.; Tadjeddine, A. *Rep Prog Phys* **2005**, *68*, 1095.

(86) Shen, Y. R. *J Opt Soc Am B* **2011**, *28*, A56.

(87) Richter, L. J.; Petralli-Mallow, T. P.; Stephenson, J. C. *Optics Letters* **1998**, *23*, 1594.

(88) Morin, M.; Jakob, P.; Levinos, N. J.; Chabal, Y. J.; Harris, A. L. *Journal of Chemical Physics* **1992**, *96*, 6203.

(89) Morin, M.; Levinos, N. J.; Harris, A. L. *Journal of Chemical Physics* **1992**, *96*, 3950.

(90) Harris, A. L.; Rothberg, L.; Dhar, L.; Levinos, N. J.; Dubois, L. H. *Journal of Chemical Physics* **1991**, *94*, 2438.

(91) Harris, A. L.; Levinos, N. J.; Rothberg, L.; Dubois, L. H.; Dhar, L.; Shane, S. F.; Morin, M. *J Electron Spectrosc* **1990**, *54*, 5.

(92) Harris, A. L.; Rothberg, L.; Dubois, L. H.; Levinos, N. J.; Dhar, L. *Phys Rev Lett* **1990**, *64*, 2086.

(93) Sass, M.; Lobau, J.; Lettenberger, M.; Laubereau, A. *Chemical Physics Letters* **1999**, *311*, 13.

(94) Graener, H.; Laubereau, A. *Chemical Physics Letters* **1987**, *133*, 378.

(95) Guyotsionnest, P.; Lin, P. H.; Hiller, E. M. *Journal of Chemical Physics* **1995**, *102*, 4269.

(96) Guyotsionnest, P.; Tadjeddine, A. *Chemical Physics Letters* **1990**, *172*, 341.

(97) Han, X.; Lass, K.; Hasselbrink, E. *Journal of Physics-Condensed Matter* **2008**, *20*.

(98) Lass, K.; Han, X.; Hasselbrink, E. *Surface Science* **2006**, *600*, 4275.

(99) Eftekhari-Bafrooei, A.; Nihonyanagi, S.; Borguet, E. *Springer Series Chem* **2009**, *92*, 361.

(100) Hawecker, J.; Lehn, J. M.; Ziessel, R. *J Chem Soc Chem Comm* **1983**, 536.

(101) Sullivan, B. P.; Bolinger, C. M.; Conrad, D.; Vining, W. J.; Meyer, T. J. *J Chem Soc Chem Comm* **1985**, 1414.

(102) Sullivan, B. P.; Meyer, T. J. *Organometallics* **1986**, *5*, 1500.

(103) Johnson, F. P. A.; George, M. W.; Hartl, F.; Turner, J. J. *Organometallics* **1996**, *15*, 3374.

(104) Smieja, J. M.; Kubiak, C. P. *Inorg Chem* **2010**, *49*, 9283.

(105) Sullivan, B. P.; Meyer, T. J. *J Chem Soc Chem Comm* **1984**, 1244.

(106) Agarwal, J.; Johnson, R. P.; Li, G. H. *Journal of Physical Chemistry A* **2011**, *115*, 2877.

(107) Kumar, B.; Smieja, J. M.; Sasayama, A. F.; Kubiak, C. P. *Chem Commun* **2012**, *48*, 272.

(108) Yoshida, T.; Tsutsumida, K.; Teratani, S.; Yasufuku, K.; Kaneko, M. *J Chem Soc Chem Comm* **1993**, 631.

(109) Worl, L. A.; Duesing, R.; Chen, P.; Ciana, L. D.; Meyer, T. J. *J. Chem. Soc. Dalton Trans.* **1991**, 849.

(110) Ai, X.; Anderson, N. A.; Asbury, J. B.; Hao, E.; Lian, T. *Proceedings of SPIE-The International Society for Optical Engineering* **2003**, *5223*, 147.

(111) Wang, Y.; Asbury, J. B.; Lian, T. *J. Phys. Chem. A* **2000**, *104*, 4291.

(112) Guo, J.; She, C.; Lian, T. *J. Phys. Chem. C* **2007**, *111*, 8979.

Chapter 2. Theoretical Description of Sum Frequency Generation

This chapter gives a description of the origin of the sum frequency (SF) response and the molecular information obtained in both the homodyne- and phase sensitive-detection schemes. In a typical vibrational sum frequency generation spectroscopy (VSFGS) experiment, two optical beams, one of fixed narrowband visible frequency ω_{vis} and one of tunable and/or broadband infrared frequency ω_{IR}, are overlapped spatially and temporally at an interface. This generates a third optical beam from the surface with a frequency equal to the sum of the two incident frequencies, i.e. $\omega_{SF} = \omega_{vis} + \omega_{IR}$. The SF response is enhanced when the infrared frequency is tuned to coincide with a vibrational resonance of the interfacial molecules, so that a vibrational spectrum can be obtained by monitoring the SF intensity as a function of infrared frequency.

Although often more technically challenging, VSFGS has several advantages over other traditional optical spectroscopies. As a second-order optical technique, SFG is forbidden in media with inversion symmetry under the electric dipole approximation, but allowed at the interface where the inversion symmetry is necessarily broken. VSFGS is thus inherently surface specific, whereas linear spectroscopy techniques cannot distinguish between bulk and interfacial signals. Since many interesting reactions occur exclusively at surfaces, VSFGS allows for the selective probing of these molecules while ignoring any bulk response. Additionally, the vibrational spectrum obtained in a VSFGS experiment is up-converted from the infrared to the visible region and can thus be detected with standard CCD cameras, as opposed to more costly and noise-sensitive infrared detectors. VSFGS can also be used to determine molecular orientation at

interfaces by monitoring the intensity and polarization of the SF response as a function of the polarization of the two input fields. These properties make VSFGS a useful spectroscopic tool for examining static vibrational spectra, average molecular orientation, and molecular dynamics at interfaces.

2.1. Origins of the Nonlinear Optical Response

When an oscillating electromagnetic field **E** is applied to a medium, it exerts a force on the valence electrons of the constituent molecules and induces an electric dipole moment **μ**. For a weak electromagnetic field, the response of the molecule is linear with respect to the field and the electric dipole is given by:[1,2]

$$\boldsymbol{\mu} = \boldsymbol{\mu}_0 + \alpha \mathbf{E} \qquad (2.1)$$

where $\boldsymbol{\mu}_0$ is the permanent dipole of the molecule and α is the polarizability of the molecular electrons. For the bulk or condensed phase, the microscopic dipoles sum to generate a macroscopic polarization **P**, defined as the dipole moment per unit volume:

$$\mathbf{P} = \varepsilon_0 \chi^{(1)} \mathbf{E} \qquad (2.2)$$

where ε_0 is the permittivity of free space and $\chi^{(1)}$ is the linear susceptibility tensor. The linear susceptibility is the macroscopic average of the polarizability **α** and describes the average molecular response to the electric field **E**. As a tensor, the linear susceptibility also indicates the directionality of the induced polarization with respect to the incident field:

$$\mathbf{P}_i = \varepsilon_0 \chi_{ij}^{(1)} \mathbf{E}_j \qquad (2.3)$$

As seen in Equation 2.3, the direction of the induced polarization may be different from the applied field. It does, however, oscillate at the same frequency as the incident electric field, thus giving rise to linear optical effects such as reflection and refraction.

As the electric field **E** is increased, a nonlinear molecular response is induced. In this case, the electric dipole can be expanded as a power series in terms of the electric field strength:

$$\boldsymbol{\mu} = \boldsymbol{\mu}_0 + \alpha\mathbf{E} + \beta\mathbf{EE} + \gamma\mathbf{EEE} + \cdots \qquad (2.4)$$

where β and γ are the first- and second-order hyperpolarizabilities, respectively. For a bulk material, this induces a polarization of the form:

$$\begin{aligned}\mathbf{P} &= \varepsilon_0(\chi^{(1)}\mathbf{E} + \chi^{(2)}\mathbf{EE} + \chi^{(3)}\mathbf{EEE} + \cdots) \\ &= \varepsilon_0(\mathbf{P^{(1)}} + \mathbf{P^{(2)}} + \mathbf{P^{(3)}} + \cdots)\end{aligned} \qquad (2.5)$$

where $\chi^{(2)}$ and $\chi^{(3)}$ are the second- and third-order nonlinear susceptibility tensors, respectively. Similar to $\chi^{(1)}$, $\chi^{(2)}$ and $\chi^{(3)}$ are the macroscopic averages of β and γ and are third- and fourth-rank tensors, respectively. $\chi^{(2)}$ and $\chi^{(3)}$ are much smaller than $\chi^{(1)}$ and only become significant in the presence of a strong electromagnetic field, such as those produced by pulsed lasers.

Equation 2.5 can be used to demonstrate the origin of various higher-order optical phenomena. As the simplest case, let us consider the second-order polarization $\mathbf{P}^{(2)}$:

$$\mathbf{P}^{(2)} = \chi^{(2)}_{ijk}\mathbf{EE} \qquad (2.6)$$

where the permittivity of free space, as a constant, has been left out for brevity. Consider a situation in which two oscillating electric fields with frequencies ω_1 and ω_2 are incident on a medium. The total electric field **E** is then given by:

$$\mathbf{E} = \mathbf{E}_1\cos(\omega_1 t) + \mathbf{E}_2\cos(\omega_2 t) \qquad (2.7)$$

The induced polarization then becomes:

$$\mathbf{P}^{(2)} = \chi^{(2)}\mathbf{E}\mathbf{E} = \chi^{(2)}[\mathbf{E}_1\cos(\omega_1 t) + \mathbf{E}_2\cos(\omega_2 t)]^2 \qquad (2.8)$$

Through some expansion and trigonometric substitution, Equation 2.8 can be rearranged as:

$$\mathbf{P}^{(2)} = \chi^{(2)}\mathbf{E}\mathbf{E} = \chi^{(2)}\left\{\begin{array}{l}\mathbf{E}_1^2 + \mathbf{E}_2^2 + \mathbf{E}_1^2\cos(2\omega_1 t) + \mathbf{E}_2^2\cos(2\omega_2 t) \\ +\frac{1}{2}\mathbf{E}_1\mathbf{E}_2\cos[(\omega_1 - \omega_2)t] + \frac{1}{2}\mathbf{E}_1\mathbf{E}_2[\cos(\omega_1 + \omega_2)t]\end{array}\right\} \qquad (2.9)$$

The two incident fields thus result in a DC field with no frequency component (the first and second terms of Equation 2.9), second harmonic generation at both input frequencies (the third and fourth terms), difference frequency generation at a frequency equal to the difference between ω_1 and ω_2 (the fifth term), and sum frequency generation at a frequency equal to the sum of ω_1 and ω_2 (the last term).

Equation 2.6 can also be used to illustrate the origins of the interface specificity for second-order optical techniques. In a medium with inversion symmetry, the use of the inversion operator changes the sign of the polarization and the electric field:

$$\begin{aligned} I_{op}\mathbf{P}^{(2)} &= -\mathbf{P}^{(2)} \\ I_{op}\mathbf{E} &= -\mathbf{E} \end{aligned} \qquad (2.10)$$

Combining these two expressions with Equation 2.6, we find:

$$\begin{aligned} I_{op}\mathbf{P}^{(2)} &= -\chi_{ijk}^{(2)}\mathbf{E}_j\mathbf{E}_k \\ I_{op}(\chi_{ijk}^{(2)}\mathbf{E}_j\mathbf{E}_k) &= \chi_{ijk}^{(2)}(-\mathbf{E}_j)(-\mathbf{E}_k) = \chi_{ijk}^{(2)}\mathbf{E}_j\mathbf{E}_k \end{aligned} \qquad (2.11)$$

In order for both expressions in Equation 2.11 to be physically valid, it becomes necessary that $\chi^{(2)} = -\chi^{(2)} = 0$. Therefore, all second-order responses, such as sum frequency generation, are forbidden in a medium with inversion symmetry. At an interface, however, the inversion symmetry is necessarily broken, thus allowing second-

order effects to take place. The interfacial SFG signal therefore results solely from interfacial molecules with negligible bulk contributions.[1]

2.2. Theoretical Description of Vibrational Sum Frequency Generation Spectroscopy

As seen in Equation 2.9, a number of different processes result from the generation of a second-order polarization at an interface. However, as we are solely interested in the process of sum frequency generation, we can effectively ignore all other second-order phenomena. Therefore, following the common practice of ignoring the explicit time dependence of the incident electromagnetic fields, we can write the SF component of the second-order polarization as:[2]

$$\mathbf{P}_{SF}^{(2)} = \chi^{(2)}\mathbf{E}_1\mathbf{E}_2 \qquad (2.12)$$

As in the linear case, the electric fields and the induced polarization have a directionality associated with them, while the second-order susceptibility tensor indicates the directionality of the induced polarization with respect to the incident fields:

$$\mathbf{P}_{i,SF}^{(2)} = \chi_{ijk}^{(2)}\mathbf{E}_{j,1}\mathbf{E}_{k,2} \qquad (2.13)$$

Equation 2.13 represents only one component of $\mathbf{P}^{(2)}$; for a complete description of the SF second-order polarization, we must write:

$$\mathbf{P}_{SF}^{(2)} = \sum_{i}^{x,y,z}\mathbf{P}_{i,SF}^{(2)} = \sum_{i}^{x,y,z}\sum_{j}^{x,y,z}\sum_{k}^{x,y,z}\chi_{ijk}^{(2)}\mathbf{E}_{j,1}\mathbf{E}_{k,2} \qquad (2.14)$$

The directionality of the SF second-order polarization is important, as different components of the polarization can be selectively probed through careful choice of the polarization of the input electric fields. This is significant because it allows SFG to be

used to determine molecular orientation at interfaces, as will be described in detail in Section 2.3.

Although sum frequency generation can result from the combination of any two electric fields, in spectroscopy it is frequently used to probe specific vibrational resonances of interfacial molecules; this is referred to as vibrational sum frequency generation spectroscopy (VSFGS). In this case, two optical beams, one of fixed narrowband visible frequency ω_{vis} and one of tunable and/or broadband infrared frequency ω_{IR}, are overlapped spatially and temporally at an interface. This generates a third coherent optical beam from the surface with a frequency equal to the sum of the two incident frequencies:

$$\omega_{SF} = \omega_{vis} + \omega_{IR} \qquad (2.15)$$

The SF beam is generated at an angle θ_{SF} from the surface normal, which is determined through the conservation of momentum of the beam components parallel to the interface, known as the phase-matching condition. For a co-propagating geometry, as in the case of our experiment, this is given by:

$$n_{SF}\omega_{SF}\sin\theta_{SF} = n_{vis}\omega_{vis}\sin\theta_{vis} + n_{IR}\omega_{IR}\sin\theta_{IR} \qquad (2.16)$$

where n_i refers to the refractive index of the material the *i* beam propagates through at the appropriate wavelength, and θ_i refers to the angle the *i* beam makes with respect to the surface normal, as shown in Figure 2.1.

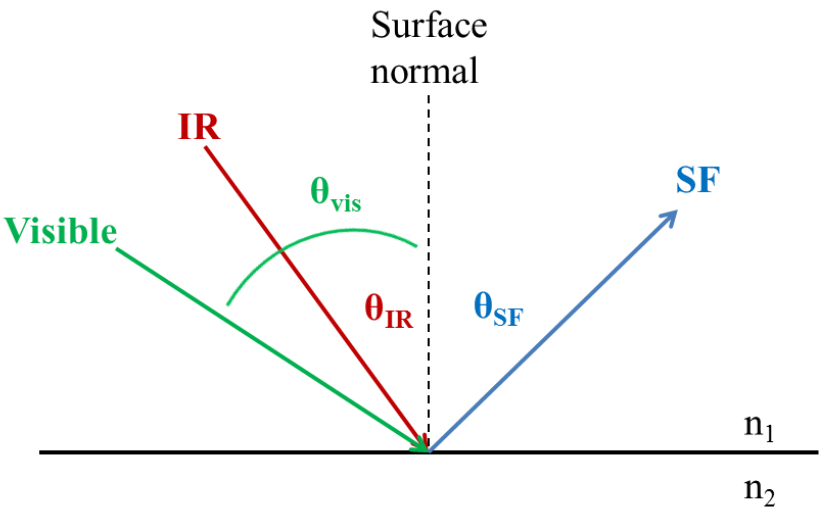

Figure 2.1. Phase-matching conditions for reflected sum frequency generation in the co-propagating geometry, indicating the beam angles with respect to the surface normal. The reflected and transmitted IR and visible beams are omitted for clarity. A transmitted SF beam is also generated, but is also omitted for clarity.

In the infrared-visible SFG configuration described here, the emitted field lies in the visible region of the electromagnetic spectrum and therefore square law detectors are used to measure the SFG signal. The intensity of the sum-frequency signal is thus given by:[1,3-6]

$$I(\omega_{SF}) \propto \left|\chi_{eff}^{(2)}\right|^2 I_{vis}(\omega_{vis}) I_{IR}(\omega_{IR}) \qquad (2.17)$$

where $I_{vis}(\omega_{vis})$ and $I_{IR}(\omega_{IR})$ are the intensities of the two incident electric fields. The effective nonlinear susceptibility $\chi_{eff}^{(2)}$ takes the form of:

$$\chi_{eff}^{(2)} = \left[\hat{\mathbf{e}}(\omega)\cdot\mathbf{L}(\omega)\right]\cdot\chi^{(2)} : \left[\mathbf{L}(\omega_1)\cdot\hat{\mathbf{e}}(\omega_1)\right]\left[\mathbf{L}(\omega_2)\cdot\hat{\mathbf{e}}(\omega_2)\right] \qquad (2.18)$$

where $\hat{\mathbf{e}}(\Omega)$ is the unit polarization vector, $\mathbf{L}(\Omega)$ is the Fresnel factor at frequency Ω, and $\chi^{(2)}$ is the nonlinear susceptibility tensor. $\chi^{(2)}$ can typically be decomposed into a sum of resonant ($\chi_R^{(2)}$) and nonresonant ($\chi_{NR}^{(2)}$) terms:

$$\chi^{(2)} = \chi_{NR}^{(2)} + \chi_R^{(2)} e^{i\phi} \qquad (2.19)$$

where the $e^{i\varphi}$ term denotes the phase difference between the resonant and nonresonant contributions. The nonresonant portion of the susceptibility may result from both the interfacial molecules and the media on either side of the interface, and is typically considered to be the result of electronic transitions. The resonant portion of the nonlinear susceptibility results solely from the interfacial molecules and is a measure of their response to the incident electric fields. More specifically, $\chi_R^{(2)}$ is defined as the macroscopic average of the microscopic molecular hyperpolarizability elements β. The elements of the resonant portion of $\chi^{(2)}$ are thus given by:

$$\chi_{ijk}^{(2)} = N_s \sum_{\alpha\beta\gamma=abc} \langle R(\psi)R(\theta)R(\phi)\rangle \beta_{\alpha\beta\gamma} \qquad (2.20)$$

where N_s is the molecule number density, $R(\Omega)$ is a rotation transformation matrix used to transform from the molecular coordinates (α,β,γ) to the laboratory coordinates (x,y,z) through the Euler angles (ψ, θ, ϕ), and the operator $\langle\ \rangle$ denotes an orientational ensemble average.

The full expression for the hyperpolarizability elements $\beta_{\alpha\beta\gamma}$ can be derived using perturbation theory.[7] In the case of SFG where the infrared frequency is in resonance with a molecular vibration, the hyperpolarizability elements take the form:[1,7]

$$\beta_{\alpha\beta\gamma}(-\omega_{sum};\omega_{vis},\omega_{IR}) = \frac{1}{2\hbar}\sum_n \frac{\mathbf{M}_{\alpha\beta}\mathbf{T}_\gamma}{(\omega_n - \omega_{IR} - i\Gamma_n)} \qquad (2.21)$$

where ω_{IR} is the frequency of the incident tunable infrared beam, ω_n and Γ_n are the frequency and damping constant of the n^{th} vibrational mode, respectively, $\boldsymbol{M}_{\alpha\beta}$ is the Raman transition moment, and $\boldsymbol{T}_\gamma$ is the infrared transition moment. The sum is over all vibrational modes of the interfacial molecules. Equation 2.21 demonstrates the primary selection rule of SFG, which states that a transition must be both Raman and infrared active in order to be SF active. The exact forms of $\boldsymbol{T}_\gamma$ and $\boldsymbol{M}_{\alpha\beta}$ for a given vibrational mode are:

$$\mathbf{T}_\gamma = \langle v|\boldsymbol{\mu}_\gamma|g\rangle \tag{2.22}$$

$$\mathbf{M}_{\alpha\beta} = \sum_s \left[\frac{\langle g|\boldsymbol{\mu}_\alpha|s\rangle\langle s|\boldsymbol{\mu}_\beta|v\rangle}{h(\omega_{SF} - \omega_{sg})} - \frac{\langle g|\boldsymbol{\mu}_\beta|s\rangle\langle s|\boldsymbol{\mu}_\alpha|v\rangle}{h(\omega_{vis} + \omega_{sg})} \right] \tag{2.23}$$

where $\boldsymbol{\mu}$ is the electric dipole operator, $|g\rangle$ is the ground state, $|v\rangle$ is the excited vibrational state, and $|s\rangle$ is any other state in the system.

Although sum frequency signal can in theory be generated from a bare interface, the signal is greatly enhanced when an incident or sum frequency is in resonance with an allowed molecular transition. In infrared-visible VSFGS, this is easily demonstrated by combining Equations 2.19, 2.20, and 2.21, with some simplifications, and examining the case when ω_{IR} approaches the resonant frequency of a single vibrational mode q:

$$\chi^{(2)} \propto \chi^{(2)}_{NR} + \frac{A_q}{\omega_{IR} - \omega_q + i\Gamma_q} e^{i\phi} \tag{2.24}$$

where A_q is the amplitude of the resonant SF-active vibration. As the infrared frequency ω_{IR} approaches the resonant frequency ω_q, the denominator approaches zero and $\chi^{(2)}$ is resonantly enhanced. This process is shown pictorially in Figure 2.2; this figure also illustrates the established relationship between $\chi^{(2)}$ and the infrared and Raman transition

moments. Equation 2.24 can be used to fit experimental VSFGS data in order to determine the relevant spectral parameters, i.e. A_q, ω_q, and Γ_q, for each resonant vibrational mode.

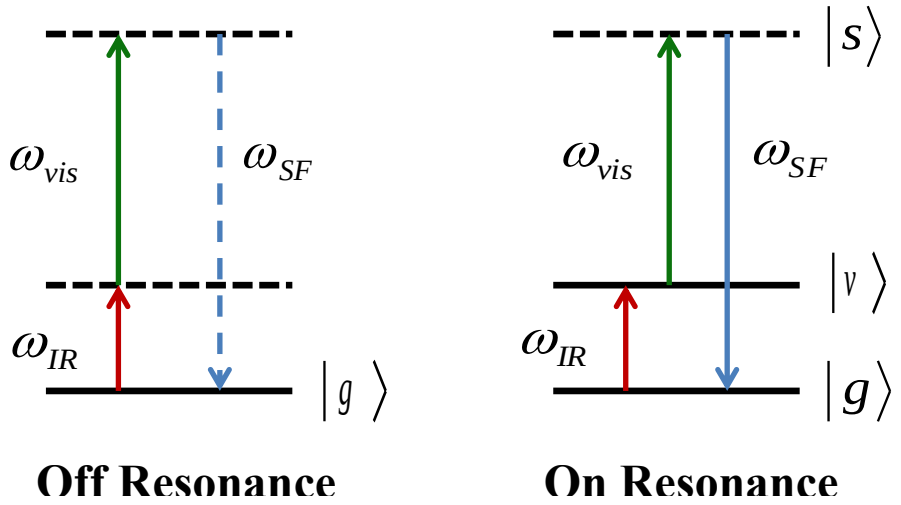

Figure 2.2. Schematic energy level diagram for infrared-visible sum frequency generation. In the off resonance case, the incident beam energies do not coincide with any molecular transitions, and the SFG response is minimal. In the on resonance case, the IR frequency is in resonance with a molecular vibration, and the SF signal is resonantly enhanced. In the on resonance diagram, the arrows are displaced to illustrate that the SF process consists of an infrared transition and an anti-Stokes Raman transition.

2.3. Using Vibrational Sum Frequency Generation Spectroscopy to Determine Molecular Orientation

As SFG is forbidden in any centrosymmetric environment, any interfacial molecular system that produces a net SFG response must have a macroscopic average orientation associated with it. All orientation information is contained in the $\chi^{(2)}_{ijk}$

elements, as shown in Equation 2.20, which relate the molecular coordinates (α,β,γ) to the laboratory coordinates (x,y,z) through three orientation angles (θ, ψ, φ). Knowledge of the $\chi^{(2)}_{ijk}$ and $\beta_{\alpha\beta\gamma}$ elements therefore allows for the determination of the average molecular orientation.

Although there are a total of 27 $\chi^{(2)}_{ijk}$ elements, this number can typically be greatly reduced depending on the symmetry properties of the interface.[1,8] As a common example, consider a surface with C_∞ symmetry, where z points towards the surface normal and x lies in the incidence plane. In this case, x = -x and y = -y, so that a reversal of the axis system should produce no effect in a contributing $\chi^{(2)}_{ijk}$ element. However, a fundamental tensor rule states that if the axis system is reversed, the corresponding tensor element must also change sign. By combining these two constraints, it can be shown that only four independent nonzero components of $\chi^{(2)}_{ijk}$ remain: $\chi_{xxz} = \chi_{yyz}$, $\chi_{xzx} = \chi_{yzy}$, $\chi_{zxx} = \chi_{zyy}$, and χ_{zzz}. Similar arguments can be used to deduce the nonzero $\chi^{(2)}_{ijk}$ elements for any surface symmetry.

Once the nonzero $\chi^{(2)}_{ijk}$ elements have been determined, these may be selectively measured through careful selection of the polarization of the incident and detected electric fields. When calculating properties at surfaces, electromagnetic waves are typically separated into components that are polarized parallel (*p*-polarized) and perpendicular (*s*-polarized) to the plane of incidence. According to the commonly adapted axis system, *p*-polarized light probes molecular transitions along the x- and z-axes, while *s*-polarized light exclusively probes those along the y-axis.

Considering the previous example of a surface with C_∞ symmetry, the four independent $\chi^{(2)}_{ijk}$ components can be determined by measuring the sum-frequency signal at four different input and output polarizations: SSP (*s*-polarized sum-frequency field, *s*-polarized visible field, and *p*-polarized infrared field, respectively), SPS, PSS, and PPP. The effective nonlinear susceptibilities for these polarization combinations are given by:[5]

$$\chi^{(2)}_{eff,SSP} = L_{yy}(\omega\omega)_{yy}(\omega_1)L_{zz}(\omega_2)\sin\beta_2\chi_{yyz} \qquad (2.25a)$$

$$\chi^{(2)}_{eff,SPS} = L_{yy}(\omega\omega)_{zz}(\omega_1)L_{yy}(\omega_2)\sin\beta_1\chi_{yzy} \qquad (2.25b)$$

$$\chi^{(2)}_{eff,PSS} = L_{zz}(\omega\omega)_{yy}(\omega_1)L_{yy}(\omega_2)\sin\beta\chi_{zyy} \qquad (2.25c)$$

$$\begin{aligned}\chi^{(2)}_{eff,PPP} = &-L_{xx}(\omega\omega)_{xx}(\omega_1)L_{zz}(\omega_2)\cos\beta\cos\beta_1\sin\beta_2\chi_{xxz}\\ &-L_{xx}(\omega\omega)_{zz}(\omega_1)L_{xx}(\omega_2)\cos\beta\sin\beta_1\cos\beta_2\chi_{xzx}\\ &+L_{zz}(\omega\omega)_{xx}(\omega_1)L_{xx}(\omega_2)\sin\beta\cos\beta_1\cos\beta_2\chi_{zxx}\\ &+L_{zz}(\omega\omega)_{zz}(\omega_1)L_{zz}(\omega_2)\sin\beta\sin\beta_1\sin\beta_2\chi_{zzz}\end{aligned} \qquad (2.25d)$$

where β's are the incident angles of the denoted optical field and L_{ii} are Fresnel factors which take into account the reflection and refraction of the fields at the interface:[3,5]

$$L_{xx}(\Omega) = \frac{2n_1(\Omega)\cos\gamma}{n_1(\Omega)\cos\gamma + n_2(\Omega)\cos\beta} \qquad (2.26a)$$

$$L_{yy}(\Omega) = \frac{2n_1(\Omega)\cos\beta}{n_1(\Omega)\cos\beta + n_2(\Omega)\cos\gamma} \qquad (2.26b)$$

$$L_{zz}(\Omega) = \frac{2n_2(\Omega)\cos\beta}{n_1(\Omega)\cos\gamma + n_2(\Omega)\cos\beta}\left(\frac{n_1(\Omega)}{n'(\Omega)}\right) \qquad (2.26c)$$

where $n_i(\Omega)$ is the refractive index of medium *i*, β is the incidence angle of the beam of interest, and γ is the refracted angle. The term $n'(\Omega)$ is considered to be an effective refractive index that describes the dielectric response of the interfacial layer.[9,10] Since the

calculated orientation is relatively sensitive to the value of $n'(\Omega)$, it is important to carefully consider this parameter.[5,9-14]

Experimentally, $n'(\Omega)$ cannot be accurately determined, and therefore several methods exist to approximate its value. The simplest involve making one of several assumptions: that $n'(\Omega)$ is equal to the bulk refractive index of either interfacial media, the average between the two, or the bulk refractive index of the interfacial molecules. However, all of these methods have been shown to be problematic and generally are not considered to be valid.[15] More quantitative approaches have also been used to estimate this parameter. Shen and co-workers have shown in several classical papers that the effective dielectric constant $\varepsilon'(\Omega)$, where $\varepsilon'(\Omega) = [n'(\Omega)]^2$, can be defined as the ratio between the microscopic local electric field correction factors at the interface, i.e. $\varepsilon'(\Omega) = l_{||}/l_{\perp}$.[5,9,13] These local field correction factors can be determined using a point-dipole model, but this requires previous knowledge of the molecular orientation. Instead, some simple assumptions can be made about the electric field at the interface, and in general the value of $n'(\Omega)$ can be estimated by:[5]

$$\left(\frac{1}{n'}\right)^2 = \frac{4n_2^2 + 2}{n_2^2(n_2^2 + 5)} \qquad (2.27)$$

where each refractive index is evaluated at the appropriate frequency.

For a vibrational transition within a particular molecular system, each independent $\chi_{ijk}^{(2)}$ element can be written in terms of the corresponding nonvanishing $\beta_{\alpha\beta\gamma}$ elements. Although there are 27 of these, the symmetry of the molecule or vibrational mode can be used to greatly reduce the number of nonzero elements.[4,7,16] Indeed, tables of nonzero $\beta_{\alpha\beta\gamma}$ elements for several different molecular symmetries have been compiled

by various authors.[7,16] Several methods are used to determine the remaining $\beta_{\alpha\beta\gamma}$ elements for each resonant transition, including the bond additivity model[4,13,17,18] and quantum mechanical calculations.[19-21] Each of these methods is known to have specific benefits and drawbacks, which must be considered carefully for each molecular system. Once the relevant $\beta_{\alpha\beta\gamma}$ elements are known, the measured SFG spectra at various input and output polarizations can be fit as a function of the orientation angles (θ, ψ, φ). Frequently a surface or molecular system is chosen so as to simplify the number of orientation angles. For our example of an azimuthally isotropic surface (i.e. C_∞ symmetry), the $\chi^{(2)}_{ijk}$ terms should contain only the tilt angle θ between the probed transition and the surface normal. The ratios of the sum-frequency signal with different polarization combinations can thus be used to determine this orientation angle θ.[5] The details of the orientation analysis for the different systems studied here will be detailed in the corresponding chapters.

2.4. Theory of Time-Resolved Vibrational Sum Frequency Generation Spectroscopy

We can expand upon Equation 2.24 to outline the theory of time-resolved VSFGS (TR-VSFGS). Specifically, we wish to consider the case in which the sample is first excited by an intense infrared pump at a resonant frequency, and VSFGS is used to subsequently probe the system as various delay times after the pump pulse. We can define the nonlinear susceptibility in this case as:

$$\chi^{(2)} = \chi^{(2)}_{NR} + \sum_q \frac{A_q (N_{0,q} - N_{1,q})}{\omega_{IR} - \omega_q + i\Gamma_q} e^{i\phi_q} \qquad (2.28)$$

where ω_{IR} is the frequency of the incident IR pulse and A_q, ω_q, and Γ_q are the amplitude, frequency, and linewidth of the resonant SF mode, respectively. As seen in Equation 2.25, the nonlinear susceptibility is a function of the population difference between the ground and first excited vibrational states, $\Delta N = N_{0,q} - N_{1,q}$. Although this is always true, this term is frequently neglected in static VSFGS since in the absence of an excitation pump pulse, the population of the first excited state is assumed to be negligible and so $N_{0,q} = N_T = 1$. Assuming we are monitoring a single vibrational mode, we can rewrite Equation 2.25 for the unpumped system as:

$$\chi_{un}^{(2)} = \chi_{NR}^{(2)} + \frac{A_{01}}{\omega_{IR} - \omega_{01} + i\Gamma_{01}} e^{i\varphi} \quad (2.29)$$

where A_{01}, ω_{01}, and Γ_{01} are the amplitude, frequency, and linewidth of the $0 \rightarrow 1$ transition of the resonant SF mode.

In the presence of an intense IR pump pulse, molecules in the ground vibrational state $v = 0$ are excited to the first excited vibrational state $v = 1$ in a two-step process: first, a vibrational coherence between the two vibrational states is established, and then population is transferred to the excited $v = 1$ state. The molecules then undergo a third interaction with a time-delayed infrared probe pulse, and their response is detected via a fourth interaction with an upconverting visible pulse. IR pump-SF probe spectroscopy is thus a fourth-order process where the molecular response can be monitored as a function of time by varying the delay between the pump and probe infrared pulses.

Following excitation, the nonlinear susceptibility $\chi^{(2)}$ evolves over time. Specifically, the population transfer from the $v = 0$ to the $v = 1$ state induces a ground state bleach (GSB) at probe frequencies corresponding to the $0 \rightarrow 1$ transition and an excited-state absorption (EA) at probe frequencies corresponding to the $1 \rightarrow 2$ transition.

Additional bands may appear over time due to the coupling of the initially excited mode with other nearby modes in the molecule. Assuming the pump intensity is sufficiently low that only a single vibrational mode is directly excited, the nonlinear susceptibility after excitation becomes:

$$\chi_p^{(2)} = \chi_{NR}^{(2)} + \left(\frac{A_{01}(N_0 - N_1)}{\omega_{IR} - \omega_{01} + i\Gamma_{01}} + \frac{A_{12}(N_1 - N_2)}{\omega_{IR} - \omega_{12} + i\Gamma_{12}} + \frac{A_{01}^c(N_1^c - N_{11})}{\omega_{IR} - \omega_{01}^c + i\Gamma_{01}^c}\right)e^{i\phi} \tag{2.30}$$

where A_{12}, ω_{12}, and Γ_{12} are the amplitude, frequency, and linewidth of the $1 \rightarrow 2$ transition of the resonant SF mode, N_1^C is the population of the coupled mode, and A_{01}^C, ω_{01}^C, and Γ_{01}^C are the amplitude, frequency, and linewidth of the $0 \rightarrow 1$ transition with one quantum of vibration in the coupled mode. Here, we have made the assumption that all three resonant terms will have approximately the same phase with respect to the nonresonant background.

The IR pump-SF probe signal is thus given by:

$$\begin{aligned}\Delta I &\propto \left|\chi_p^{(2)}\right|^2 - \left|\chi_{un}^{(2)}\right|^2 \\ &\propto \left|\chi_{NR}^{(2)} + \left(\frac{A_{01}(N_0 - N_1)}{\omega_{IR} - \omega_{01} + i\Gamma_{01}} + \frac{A_{12}(N_1 - N_2)}{\omega_{IR} - \omega_{12} + i\Gamma_{12}} + \frac{A_{01}^c(N_1^c - N_{11})}{\omega_{IR} - \omega_{01}^c + i\Gamma_{01}^c}\right)e^{i\phi}\right|^2 \\ &\quad - \left|\chi_{NR}^{(2)} + \left(\frac{A_{01}}{\omega_{IR} - \omega_{01} + i\Gamma_{01}}\right)e^{i\phi}\right|^2\end{aligned} \tag{2.31}$$

Equation 2.28 can be used to describe the origins of the transient response in TR-VSFGS spectra for a given adsorbate-substrate system. Depending on the magnitude of the nonresonant background, it is possible to simplify this expression for both small and large values of $\chi_{NR}^{(2)}$, though the final manifestation will be slightly different for each scenario. This will be described in detail for both ReC0A/TiO_2 (110) and ReC0-Au in Chapter 7.

2.5. References

(1) Shen, Y. R. *The principles of nonlinear optics*; J. Wiley: New York, 1984.

(2) Lambert, A. G.; Davies, P. B.; Neivandt, D. J. *Applied Spectroscopy Reviews* **2005**, *40*, 103.

(3) Feller, M. B.; Chen, W.; Shen, Y. R. *Physical Review A: Atomic, Molecular, and Optical Physics* **1991**, *43*, 6778.

(4) Hirose, C.; Akamatsu, N.; Domen, K. *Journal of Chemical Physics* **1992**, *96*, 997.

(5) Zhuang, X.; Miranda, P. B.; Kim, D.; Shen, Y. R. *Physical Review B* **1999**, *59*, 12632.

(6) Rao, Y.; Tao, Y. S.; Wang, H. F. *Journal of Chemical Physics* **2003**, *119*, 5226.

(7) Moad, A. J.; Simpson, G. J. *Journal of Physical Chemistry B* **2004**, *108*, 3548.

(8) Hirose, C.; Akamatsu, N.; Domen, K. *Appl Spectrosc* **1992**, *46*, 1051.

(9) Ye, P. X.; Shen, Y. R. *Physical Review B* **1983**, *28*, 4288.

(10) Bell, G. R.; Bain, C. D.; Ward, R. N. *Journal of the Chemical Society-Faraday Transactions* **1996**, *92*, 515.

(11) Zhang, T. G.; Zhang, C. H.; Wong, G. K. *J Opt Soc Am B* **1990**, *7*, 902.

(12) Braun, R.; Casson, B. D.; Bain, C. D. *Chemical Physics Letters* **1995**, *245*, 326.

(13) Wei, X.; Hong, S. C.; Zhuang, X. W.; Goto, T.; Shen, Y. R. *Phys Rev E* **2000**, *62*, 5160.

(14) Ekhoff, J. A.; Rowlen, K. L. *Anal Chem* **2002**, *74*, 5954.

(15) Wang, H. F.; Gan, W.; Lu, R.; Rao, Y.; Wu, B. H. *International Reviews in Physical Chemistry* **2005**, *24*, 191.

(16) Dick, B. *Chemical Physics* **1985**, *96*, 199.

(17) Yamamoto, H.; Akamatsu, N.; Wada, A.; Domen, K.; Hirose, C. *J Electron Spectrosc* **1993**, *64-5*, 507.

(18) Hirose, C.; Yamamoto, H.; Akamatsu, N.; Domen, K. *Journal of Physical Chemistry* **1993**, *97*, 10064.

(19) van Gisbergen, S. J. A.; Snijders, J. G.; Baerends, E. J. *Journal of Chemical Physics* **1998**, *109*, 10644.

(20) Quinet, O.; Champagne, B. *Int J Quantum Chem* **2001**, *85*, 463.

(21) Champagne, B.; Fischer, P.; Buckingham, A. D. *Chemical Physics Letters* **2000**, *331*, 83.

Chapter 3. Experimental Methods

This chapter outlines the experimental methods used for sample preparation, data collection, and data processing. All VSFGS experiments were carried out using the same laser system, though different detection schemes were employed for different experiments.

3.1. Sample Preparation

3.1.1. Molecular Adsorbates – Re bipyridyl complexes

Re(dcbpy)$(CO)_3$Cl [dcbpy = 2,2'-bipyridine-4,4'-$(COOH)_2$] (ReC0A). The transition metal complex ReC0A was prepared by Dr. William Rodriguez in a one-step reaction based on the method reported by Meyer *et al.*[1] Briefly, equimolar mixtures of 4,4'-$(COOH)_2$-bpy and $Re(CO)_5Cl$ were added to 50 mL of ethylene glycol dimethyl ester and heated at reflux for 4 h. The mixture was then cooled at room temperature and small portions of hexane were added with continuous stirring. The complexes precipitated as an orange solid which was filtered and dried in air. The reaction is essentially quantitative before recrystallization. Figure 3.1 shows the schematic structure of this complex.

Re(Lp)$(CO)_3$Cl [Lp = 2,2'-bipyridine-4,4'-bis-nCH_2-COOH] (ReCnA). ReCnA complexes were prepared according to published procedures by Dr. Joseph T. Hupp`s group at Northwestern University.[2,3] Figure 3.1 shows the schematic structure of these complexes.

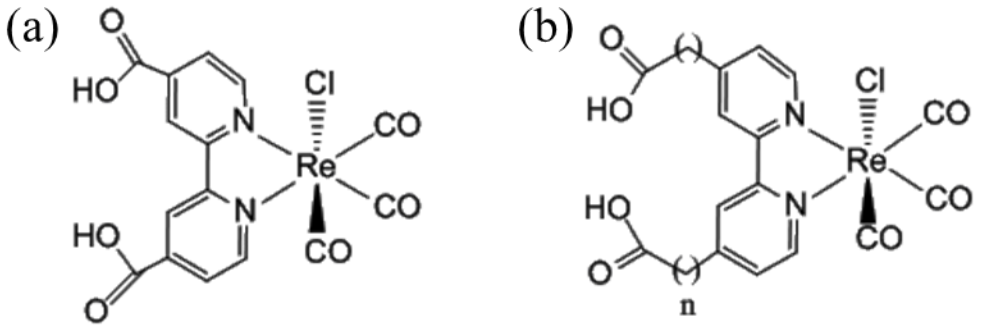

Figure 3.1. Schematic structures of (a) ReC0A and (b) ReCnA.

3.1.2. Preparation of TiO_2 Single Crystal Substrates

Rutile (001), (110), and (100) TiO_2 single crystals were purchased from Commercial Crystal Laboratories, Inc. Prior to initial use, the crystals were sonicated in piranha solution (3:1 H_2SO_4/H_2O_2) for one hour, followed by a MilliQ (18 MΩ) water rinse. They were then placed in 1 M NaOH solution for 5 minutes, followed by another MilliQ rinse. The crystals were then placed in 1 M HCl solution and exposed to UV radiation for 10 minutes. After the UV treatment, the crystals were rinsed with ethanol and subsequently sensitized with the molecular adsorbates of interest. After preparation, the sensitized samples were stored in a dark, dry environment in order to preserve sample integrity for as long as possible. Between experiments, the crystals were cleaned by immersion in 1 M HCl for 5 minutes followed by immersion in 0.2 M NaOH for 5 minutes. This process was repeated a total of three times, rinsing the crystal with MilliQ water between each immersion. After cleaning, the previously outlined procedure for UV irradiation and sensitization were followed. Periodically, after the cleaning procedure but before sensitization, the single crystals were imaged by atomic force microscopy (AFM)

to ensure that clean, flat surfaces were still being produced. Figure 3.2 shows a representative AFM image of the TiO_2 (001) single crystal surface.

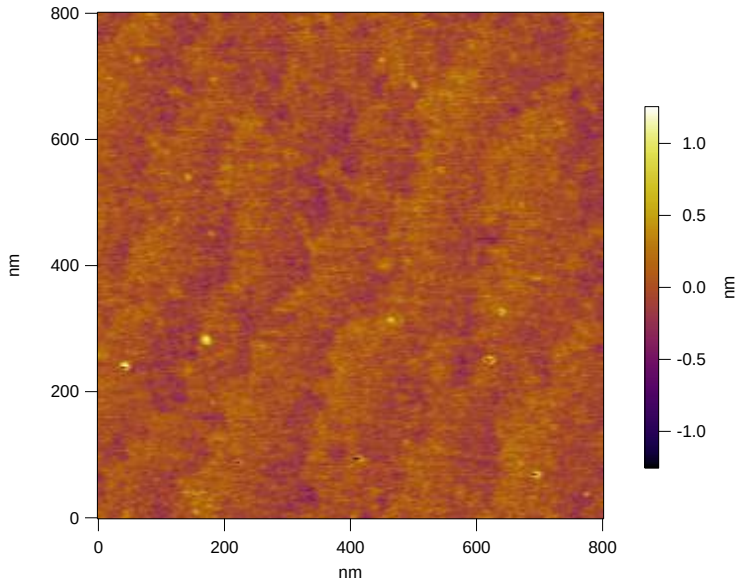

Figure 3.2. AFM image (800 nm x 800 nm) of TiO_2 (001) single crystal surface.

3.1.3. Sensitization of Rutile TiO_2 Single Crystals

Rutile (001), (110), and (100) TiO_2 single crystals were sensitized by immersion in ethanolic solutions of each sensitizer molecule. The TiO_2 crystals were typically sensitized overnight, and then washed with ethanol to remove any nonadsorbed molecules remaining on the TiO_2 surface prior to use. After preparation, the samples were stored in a dark, dry environment in order to preserve sample integrity for as long as possible. The adsorbate coverage levels were controlled by both the immersion time and adsorbate solution concentration. The concentration of each adsorbate solution was monitored by its UV-visible absorption and controlled to be the same for each molecule investigated.

3.1.4. Preparation of Au Films

Gold films were prepared on clean sapphire substrates via sputter coating. Sapphire windows (1" diameter) were first sonicated in piranha solution (3:1 H_2SO_4/H_2O_2) for 1 hour, washed with DI water, and then sonicated in DI water for 1 hour. Au films were deposited on the cleaned sapphire windows using an EMS 550X Sputter Coater**.** The deposition rate for the Au films was 15 nm per minute at a current of 50 mA; all samples were sputter coated at an Argon pressure of 1 x 10^{-1} mbar for 12 minutes, resulting in a film thickness of 180 nm. The films were subsequently flame annealed to produce a smooth, crystalline surface.

3.1.5. Chemisorption of a Rhenium Bipyridyl Complex on Gold Substrates

The rhenium bipyridyl complex ReC0A was chemisorbed onto gold substrates by Dr. William Rodriguez in a two-step process based on published procedures.[4] First, a self-assembled monolayer (SAM) was prepared on gold. The synthesis of the self-assembled monolayer was achieved following the procedures reported by Pan *et al.* with slight modifications.[5] Briefly, the SAM was prepared by immersing a gold substrate into a 1 mM solution of 11-mercapto-1-undecanol in absolute ethanol for 7 days at room temperature with constant stirring. After this period, the gold film/SAM sample was rinsed several times with absolute ethanol, ultrasonically cleaned in ethanol for 2 minutes, and dried in a flow of pure argon gas.

The second step involved the reaction of the ReC0A complex with the SAMs on gold. The functionalization of the SAMs was performed by esterification of the OH terminal groups of the thiol adsorbed on gold and the carboxylic groups of the ReC0A

complex. The procedure was performed in inert argon atmosphere. A freshly prepared SAM/gold sample was immersed in a ReC0A dry tetrahydrofuran (THF) solution (0.1 mg/ml) containing *N*-(3-Dimethylaminopropyl)-*N′*-ethylcarbodiimide hydrochloride, EDC (50 mg/ml), and 4-dimethylaminopyridine, DMAP (0.1 mg/ml). The reaction was stirred at 50 °C for 24 h. The substrate was subsequently rinsed several times with THF, taken out of the argon box, thoroughly washed with DMF, and dried in a flow of pure argon gas. The functionalization of the SAMs is illustrated in Figure 3.3.

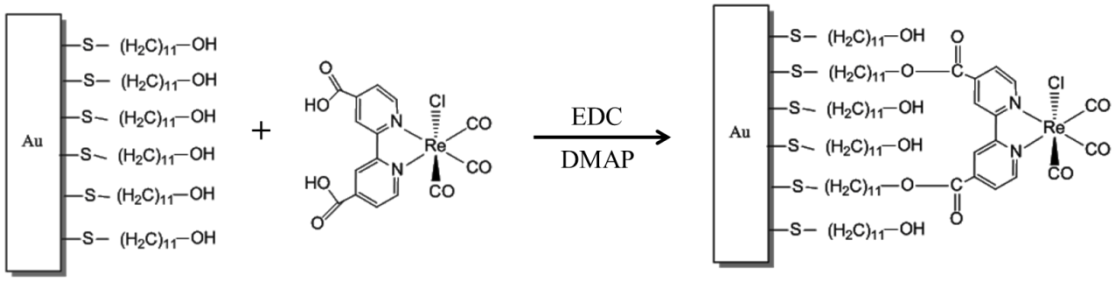

Figure 3.3. Functionalization of SAMs on gold with ReC0A as described in the text.

3.2. Static Vibrational Sum Frequency Generation Spectroscopy Measurements

Briefly, the vibrational sum frequency generation spectroscopy (VSFGS) measurements were carried out using a 1 kHz Spitfire Pro Ti:Sapphire regenerative amplifier system (Spectra Physics) producing 120 fs pulses at 800 nm with pulse energies of 4 mJ. Half of the fundamental was used to pump a TOPAS-C (Light Conversion) optical parametric amplifier (OPA), which produces tunable IR pulses with energies of 10 – 20 μJ and typical bandwidths of ~200 cm^{-1}. The remaining 2 mJ of the 800 nm fundamental beam was filtered with a narrowband interference filter (CVI F01-800-UNBLK-1.00) to narrow the spectral bandwidth to ~12 cm^{-1} (< 1 nm) centered at 799

nm. Alternatively, the remaining 2 mJ of 800 nm could be used to pump an SHBC/TOPAS-400-WL OPA (Light Conversion) system, producing tunable picosecond visible pulses from 480 – 800 nm with typical pulse energies of > 50 μJ and bandwidths of ~10 cm^{-1}. For both visible schemes, the visible pulses were filtered to 2 – 10 μJ using a variable-ND filter wheel and spatially and temporally overlapped with the IR at the sample. The temporal overlap between the IR (~150 fs) and visible (~1 ps) pulses was controlled with a variable delay stage in order to suppress any nonresonant SFG signals for certain samples.[6] The specifics of the sample stage differed depending on the particular experiment, as described in detail below. In general, after the sample stage, the reflected sum frequency signal was collimated and filtered to remove any residual IR and fundamental visible photons before being refocused onto the slit of an imaging spectrograph (Acton Instruments SpectraPro 300i, 1200 groove/mm grating) and detected with an air-cooled CCD camera (Princeton Instruments VersArray 512B, 512 x 512 pixels) operating at -40.0°C. The polarizations of the IR, visible, and SFG beams were controlled with polarizer/half-waveplate combinations. Figure 3.4 shows a schematic diagram of the experimental set-up. Each component of the VSFGS spectrometer will be discussed below in further detail.

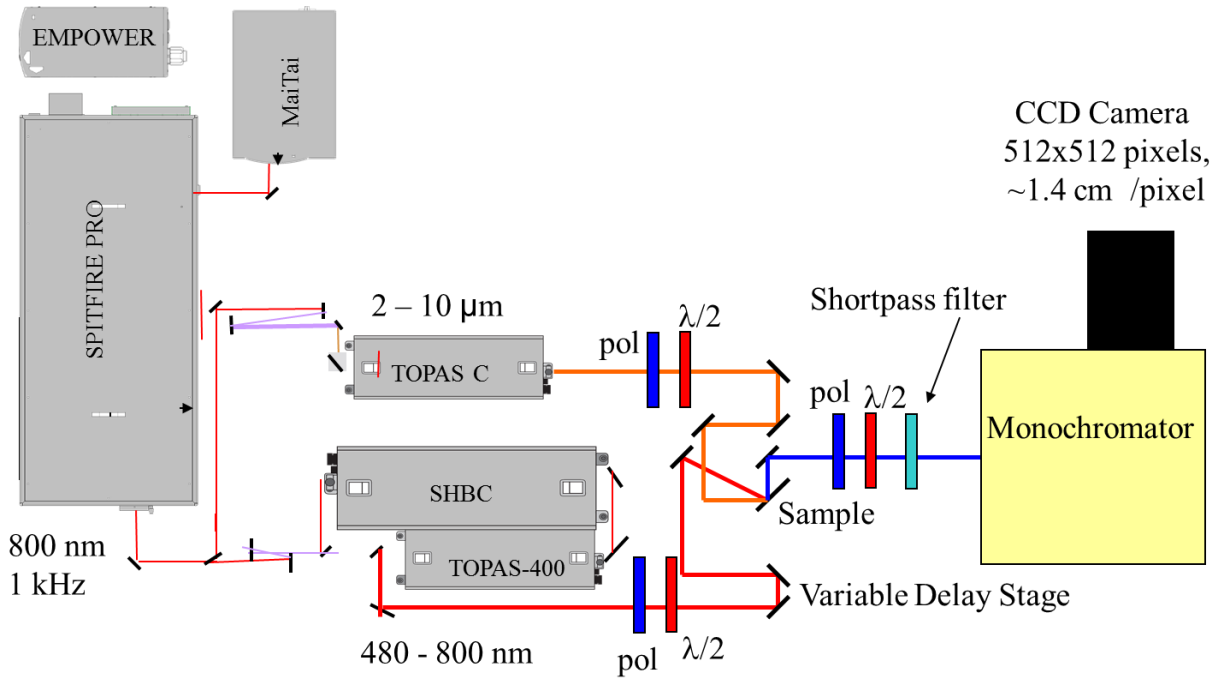

Figure 3.4. Schematic diagram of the VSFGS experimental set-up.

3.2.1. The Laser Source

The laser source was a Ti:Sapphire chirped pulse regeneratively amplified laser system (Spectra Physics). Overall, the system produces 800 nm pulses with pulsewidths of 120 fs and pulse energies of 4 mJ at a 1 kHz repetition rate. The laser system consists of three main components: a diode-pumped mode-locked Ti:Sapphire oscillator (Mai Tai, seed source); a diode-pumped solid state Nd:YLF laser (Empower, pump source); and a Ti:Sapphire regenerative amplifier (Spitfire Pro).

The Mai Tai is a diode-pumped, actively-modelocked Ti:Sapphire oscillator operating at 800 nm with a 80 MHz repetition rate. Briefly, a high-power, fiber-coupled diode laser module is used to end-pump a vanadate lasing medium, producing 15 W of 1064 nm. This is frequency doubled in an LBO crystal to produce 532 nm, which is then used to pump a Ti:Sapphire lasing medium in a folded cavity. The Ti:Sapphire cavity is

modelocked using an acousto-optic modulator (AOM) and produces an 80 MHz train of 800 nm pulses with pulsewidths of < 100 fs and an average power of ~700 mW. The output of the Mai Tai is used as a seed source for the Spitfire Pro regenerative amplifier.

The Empower is a diode-pumped, Q-switched Nd:YLF laser system operating at 1054 nm with a 1 kHz repetition rate. The output is frequency doubled in a temperature-controlled LBO crystal to 527 nm, producing pulses with typical pulse energies of > 20 mJ and an average output power of > 20 W. The output of the Empower is used as a pump source for the Spitfire Pro regenerative amplifier.

The Spitfire Pro can be divided into three internal sections: the stretcher, the regenerative amplifier, and the compressor. The seed pulses from the Mai Tai Ti:Sapphire oscillator entire the Spitfire and are directed into the stretcher, where a double-pass grating-curved mirror pair is used to stretch the pulses to produce positively-chirped pulses of picosecond duration. The chirped pulses then enter the regenerative amplifier portion of the Spitfire Pro, where individual pulses are selected to be trapped inside the amplifier using two Pockels cells (PC). Specifically, Pockels cell 1 (PC1) is used to either trap or reject the initial seed pulses, and Pockels cell 2 (PC2) is used to eject the amplified pulses at specific times when they reach the maximum power possible inside the regenerative amplifier. Since the repetition rate of the seed source (80 MHz) is much higher than the overall system output (1 kHz), the vast majority of pulses are rejected before amplification and are directed into a beam dump. The seed pulses trapped within the amplifier cavity are amplified in a Ti:Sapphire crystal pumped by the Empower output beam. The correct timing of the two PCs is critical to achieving maximum output power with the greatest stability from the Spitfire Pro system. After the

amplified pulses are ejected from the amplifier, they are directed into the compressor, which uses a double-pass grating-curved mirror pair to compress the pulses back down to ~120 fs and reverse the frequency-chirping induced in the stretcher. After compression, the amplified, 120 fs pulses centered at 800 nm (~12 nm FWHM) leave the Spitfire Pro system with an average power of 4 mJ at a repetition rate of 1 kHz.

3.2.2. Generation of Tunable Broadband Infrared Pulses

Tunable broadband infrared pulses were generated using a traveling-wave optical parametric amplifier (TOPAS-C, Light Conversion) pumped by 2 mJ of the fundamental 800 nm output of the Spitfire Pro system. The beam diameter of the fundamental was first reduced with a mirror telescope from ~10 cm to ~5 cm. The beam was then directed into the TOPAS-C, where it is divided into two parts by passing through an 80/20 beam splitter. The higher energy (80%) portion of the beam is termed the amplifier and is used in the final stage of the TOPAS-C. The lower energy (20%) portion of the beam is further split with a 50/50 beam splitter. Half is focused into a calcium fluoride (CaF_2) window to generate a white-light continuum (WLC), which is then spatially and temporally overlapped with the remaining half (termed the pre-amplifier) in a β-barium borate (BBO) crystal. In a process called parametric amplification, a portion of the 800 nm beam interacts with two near-IR frequencies present in the WLC, leading to an amplification of these so-called signal (S) and idler (I) frequencies and a corresponding de-amplification of the pre-amplifier pulse. The sum of the signal and idler frequencies, where the signal is the beam of higher frequency, is equal to the frequency of the fundamental 800 nm beam (i.e. $\omega_S + \omega_I = \omega_{800}$). The particular signal and idler frequencies that are generated are

determined by the angle of the BBO crystal according to phase matching conditions. After this pre-amplifier stage, the generated signal and idler beams are spatially and temporally overlapped with the amplifier beam in a second BBO crystal, further amplifying them. The amplifier pump beam is removed using a dichroic mirror and the signal and idler beams are collinearly ejected from the TOPAS-C with overall output intensities of > 500 mW (signal + idler).

To generate tunable infrared pulses, the near-IR signal and idler were combined in a $AgGaS_2$ crystal, where they undergo difference frequency generation (DFG):

$$\omega_{IR} = \omega_{DFG} = \omega_{sig} - \omega_{idl} \qquad (3.1)$$

Before arriving at the DFG crystal, the signal and idler beams passed through a time-correction plate, which adjusts the relative timing of the two pulses to optimize their temporal overlap. The frequency of the ultimate infrared output is determined by the frequency of the signal and idler beams and the angle of the $AgGaS_2$ crystal according to phase matching conditions. Thus, the angles of the BBO and $AgGaS_2$ crystals must be tuned in concert to generate the desired IR frequency. All three crystals, as well as two internal delay stages which control the WLC-pre-amplifier timing and the S+I-amplifier timing, were computer controlled using software provided by Light Conversion. The TOPAS-C has an overall tuning range of 2800 – 10000 nm and an output power of ~2 – 15 mW, depending on the selected IR frequency.

The leftover signal and idler beams were separated from the generated IR beam after passing through a ZnSe filter set at the Brewster angle. The IR beam was then directed to the sample stage using gold mirrors, where the alignment was optimized through the use of liquid crystal paper. The polarization of the IR beam was controlled

using a silicon thin-film polarizer and a frequency-tunable CaF_2 waveplate. All experiments reported here were performed using an IR frequency at or near ~5000 nm.

3.2.3. Generation of Narrowband Visible Pulses

Narrowband visible pulses are necessary for the broadband vibrational sum frequency generation spectroscopy (BB-VSFGS) experiment, as the spectral bandwidth of the visible pulse determines the spectral resolution in the resulting VSFGS spectrum. These narrowband visible pulses were generated using two different methods, depending on the experiment. In one scheme, 2 mJ of 800 nm was filtered with a narrowband interference filter (CVI F01-800-UNBLK-1.00) to narrow the spectral bandwidth to ~12 cm^{-1} (< 1 nm) centered at 799 nm. The throughput of the interference filter is ~20%, yielding ~40 μJ pulses. These were filtered to 2 – 10 μJ using a variable-ND filter wheel before being focused onto the sample.

The other method of generating narrowband visible pulses involved the use of a second harmonic bandwidth compressor (SHBC, Light Conversion) combined with a traveling-wave OPA (TOPAS-400-WL, Light Conversion) pumped with the 400 nm output of the SHBC. The SHBC is a nonlinear optical device used to generate a narrow bandwidth (3 – 10 cm^{-1}) second harmonic (SH) pulse when pumped by an intense transform-limited (or nearly transform-limited) femtosecond or picosecond pulse with a bandwidth of 20 – 500 cm^{-1}. For the system described here, the input beam was an 800 nm pulse (~120 fs) with a bandwidth of ~12 nm (~200 cm^{-1}), and the output was a 400 nm pulse (~2 ps) pulse with a bandwidth of ~0.5 nm (~7 cm^{-1}). The bandwidth narrowing was accomplished by utilizing the effect of pulse chirp elimination through second

harmonic generation (SHG) when the two input beams exhibit opposite temporal chirps, as illustrated in Figure 3.5. Upon entering the SHBC, the input beam is split by a 50/50 beam splitter, and the two resulting beams are then sent through separate pulse stretching arms. The pulse stretching is accomplished via grating-cylindrical lens pairs for each arm. In the first arm, the cylindrical lens is positioned so that the distance between the cylindrical lens and the grating is smaller than the focal length of the lens, i.e. $L < f$, yielding a positively chirped picosecond pulse. In the second arm, the cylindrical lens is positioned so that the distance between the cylindrical lens and the grating is larger than the focal length of the lens, i.e. $L > f$, yielding a negatively chirped picosecond pulse. The two oppositely-chirped pulses are then recombined in a BBO crystal, yielding a narrow bandwidth, chirp-free 400 nm pulse, as illustrated in Figure 3.5. In our configuration, the final output of the SHBC was ~2 ps pulses at 400 nm with pulse energies of 800 μJ.

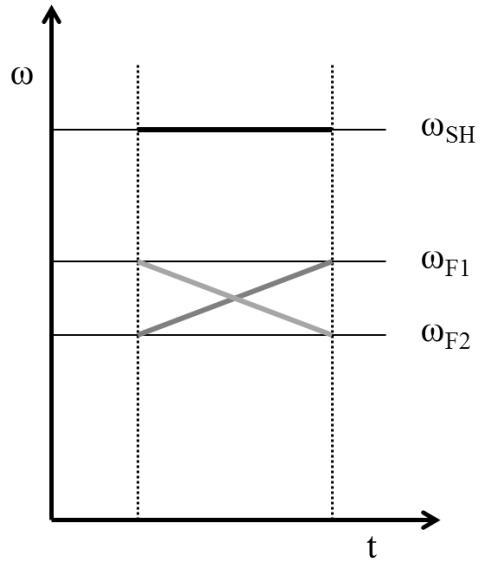

Figure 3.5. Illustration of pulse chirp elimination through second harmonic generation (SHG) when the two input beams (ω_{F1} and ω_{F2}) exhibit opposite temporal chirps.

A small (~5%) portion of the SHBC input beam is separated with a beam splitter and sent through a separate delay arm. This arm is used to generate a white-light continuum (WLC) by focusing the 800 nm into a CaF_2 plate. The WLC is then used to seed the TOPAS-400-WL (Light Conversion) system, which is a three stage optical parametric amplifier pumped by the picosecond 400 nm output of the SHBC. Similar to the TOPAS-C, the TOPAS-400-WL combines the white light continuum in a nonlinear crystal (BBO) with an amplifier beam in three stages, leading to an amplification of so-called signal (S) and idler (I) frequencies and a corresponding de-amplification of the pre-amplifier and amplifier beams. In the TOPAS-400-WL, the signal and idler frequencies are in the visible and near IR, respectively, and the sum of their frequencies is equal to the frequency of the pump pulse (400 nm).

When pumped by 800 mW of 400 nm (2 ps pulsewidth), the TOPAS-400-WL produced tunable signal and idler beams with frequency ranges of at 480 – 800 nm and 800 – 2400 nm, respectively, with typical pulse energies of > 50 μJ and bandwidths of ~10 cm^{-1}. The idler beam was discarded into a beam dump, and the desired signal frequency was filtered to 2 – 10 μJ using a variable-ND filter wheel and spatially and temporally overlapped with the IR at the sample. The desired signal wavelength was generated through careful selection of the BBO crystal angle and the timing between the WLC and amplifier beams in all three stages of amplification. All crystal tuning and delay stage positioning was computer-controlled using software provided by Light Conversion.

3.2.4. Sample Stage

3.2.4.1. Static Homodyne-detected Vibrational Sum Frequency Generation Spectroscopy Measurements

The visible and IR beams were spatially and temporally overlapped at the sample surface. Initial alignment of the IR beam was accomplished using liquid crystal paper, while the visible beam could be aligned visually. The height of the beams was controlled through the use of irises along the beam path. The visible beam was sent through a manual delay stage prior to the sample in order to control the timing between the visible and IR beams. The visible and IR beams were focused onto the sample using convex lenses, producing average beam sizes of ~200 μm and ~150 μm, respectively. The lenses were positioned so that the beams were focused just before the sample surface in order to prevent focusing in the substrate and subsequent production of large white-light or nonresonant signals.

The sample stage alignment was performed in the horizontal plane (i.e. all beams parallel to the laser table), so that the sample was positioned perpendicular to the laser table. The sample was positioned on a three-dimensional rotation-translation stage. This allowed for the translation of the sample to minimize signal degradation, as well as rotation of the sample to vary the angle of the visible and IR beams with respect to the sample surface normal. The angle between the visible and IR beams was held constant during a given experiment, but was changed between experiments for convenience of alignment for a particular experimental set-up.

Temporal overlap was accomplished by spatially overlapping the two beams in a BBO crystal at the sample stage and looking for the resulting SFG signal as the visible

delay time was scanned. The BBO crystal was then replaced by a reference sample with a large nonresonant signal, such as z-cut quartz, in order to optimize the spatial and temporal overlap. The reflected SFG signal from the reference sample was collected using a collimating lens and directed towards the imaging spectrometer with broadband visible dielectric mirrors. The direction of the reflected SF beam could be deduced from the incident angles of the visible and infrared beams according to their phase-matching conditions (given in Equation 2.16).

For experiments where the VSFGS signal was monitored as a function of the sample azimuthal angle, the sample was placed in a mirror mount attached to a motorized rotation mount (perpendicular to the laser table) on the three-dimensional rotation-translation sample stage. To ensure that any change in the VSFGS signal resulted solely from the molecular alignment on the sample, and not from a change in sample position, a beam from a HeNe laser was reflected off of the sample stage onto a grid across the table. The position of the reflected beam was monitored as a function of the sample rotation angle, and the sample alignment was adjusted with the mirror mount until the reflected beam did not change position as the sample rotated. During data collection, the motorized rotation mount was computer controlled using a user-defined LabView program, so that VSFSGS spectra were collected at varying degree integrals. The experiment was then repeated for a sample with a large nonresonant signal and no azimuthal dependence, such as gold, to ensure that the sample position (and thus SFG intensity) remained unchanged as the sample mount rotated.

3.2.4.2. Static Phase Sensitive-detected Vibrational Sum Frequency Generation Spectroscopy Measurements

Phase sensitive-detected vibrational sum frequency generation spectroscopy (PS-VSFGS) measurements were carried out on the same laser system as the HD-VSFGS measurements and with an identical experimental design up to the sample stage. After the sample stage, the reflected IR, visible and SFG beams were collected by a spherical mirror and refocused onto a piece of y-cut quartz in order to generate the local oscillator signal. A 2 mm thick CaF_2 window was placed in the sample SF beam path in order to delay the sample SF beam by approximately 3.8 ps with respect to the local oscillator. The local oscillator and signal beams were then collimated and filtered to remove any remaining visible and IR light. Figure 3.6 shows a schematic diagram of the PS-VSFGS portion of the experimental set-up.

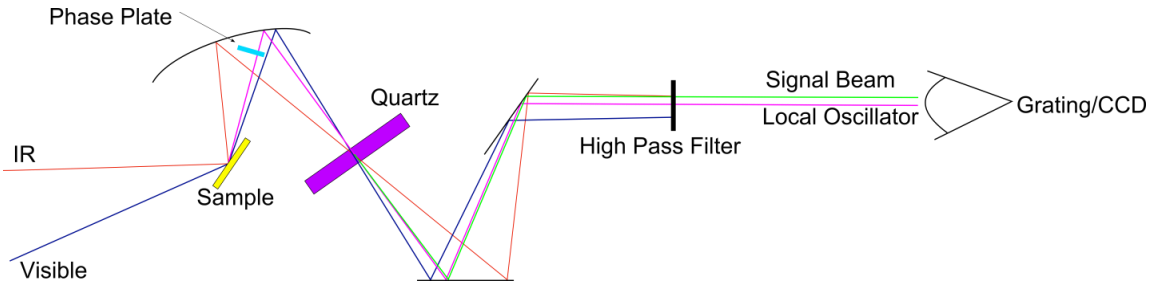

Figure 3.6. Schematic diagram of the PS-VSFGS portion of the experimental set-up.

3.2.5. Detecting Generated Sum Frequency Pulses

After the sample stage, all reflected beams were sent through a bandpass filter to remove any residual fundamental visible light; the choice of filter for a particular experiment was based on the frequency of the generated SF beam compared to the

incident visible beam. Any residual IR light was assumed to be negligible and did not interfere with signal detection. The SF beam was sent through an achromatic half waveplate designed for 400 – 800 nm (Thorlabs) and a CaF_2 Glenn-Taylor polarizer before being focused onto the entrance slit of the imaging spectrograph (Acton Instruments SpectraPro 300i, 1200 groove/mm grating) with a 100 mm convex lens. The spectrograph served to spatially separate the SF signal as a function of frequency, directing it onto an air-cooled CCD camera (Princeton Instruments VersArray 512B, 512 x 512 pixels) operating at -40.0°C.

Due to the low efficiency of the SF process, efforts were made to increase the signal-to-noise ratio (SNR) when collecting VSFGS spectra. In order to reduce the dark count noise from the CCD camera, only those strips of pixels that were illuminated by the SF signal were binned together to create a spectrum; typically, this consisted of < 10 strips out of a possible 512. In order to reduce the read noise from the CCD, scans were often collected with 5 or 10 second acquisition times. Additionally, 10 – 20 scans were typically collected and then averaged together. Background scans were taken by collecting data for an identical amount of time and number of scans, but with the visible and/or IR beams blocked, in order to quantify the amount of background radiation being detected; these background scans were subsequently subtracted from the collected spectra, significantly improving the SNR. Since the spectral resolution of our VSFGS experiment was given by the visible bandwidth (~10 cm^{-1}), yet the resolution of the CCD was 1.2 cm^{-1}, the collected signal was also averaged across ~10 cm^{-1}. This preserved the actual resolution of the experiment while simultaneously improving the spectral appearance.

3.3. Time-Resolved Measurements

3.3.1. IR-Pump SFG-Probe Homodyne-detected Vibrational Sum Frequency Generation Spectroscopy Measurements

Pump-probe VSFGS measurements were carried out on the same laser system as the static HD-VSFGS measurements and with a similar experimental design. For these experiments, the visible pulse was generated by frequency-narrowing 2 mJ of the fundamental 800 nm with a narrowband interference filter (CVI F01-800-UNBLK-1.00) to narrow the spectral bandwidth to ~12 cm^{-1} (< 1 nm) centered at 799 nm. This method was used over the SHBC/TOPAS-400 OPA due to its better stability. The IR pulses were generated using the TOPAS-C OPA and the resulting output was then split using a 50/50 broadband IR beamsplitter. Half of this was used as the probe VSFG beam; it was typically attenuated using Ge filters and aligned on the sample as described previously. The remaining portion of the generated IR was sent through a computer controlled delay stage and overlapped at the sample with the probe visible and IR beams. Every other pump pulse was blocked by a synchronized chopper (New Focus 3500) operating at 500 Hz. The reflected VSFG signal was collimated and filtered before being refocused onto the slit of the imaging spectrograph and detected with the CCD. The pumped and unpumped VSFG signals were spatially separated using a galvanometric servocontrolled optical scanning mirror. The galvanomirror was supplied with a 500 Hz sinusoid voltage from a function generator, synchronized with the optical chopper, which caused the mirror to oscillate about its axis. This caused a spatial separation between the pumped and unpumped VSFG signals on the CCD camera; the magnitude of this separation could be controlled through the amplitude of the generated sinusoidal voltage. The pumped and

unpumped spectra could thus be separately binned in order to compare the spectra with and without IR excitation.

The spatial and temporal overlap of the pump and probe beams was optimized by monitoring the IR-IR-visible (IIV) SFG intensity from a gold substrate.[7] The instrument response function was characterized by scanning the delay of the pump IR with respect to the probe SFG pulse pair and recording the resulting IIV-SFG intensity. Typically, the instrument response function was well fit by a Gaussian function with ~180 fs fwhm. A typical pump-probe IIV-SFG cross-correlation trace shown in Figure 3.7.

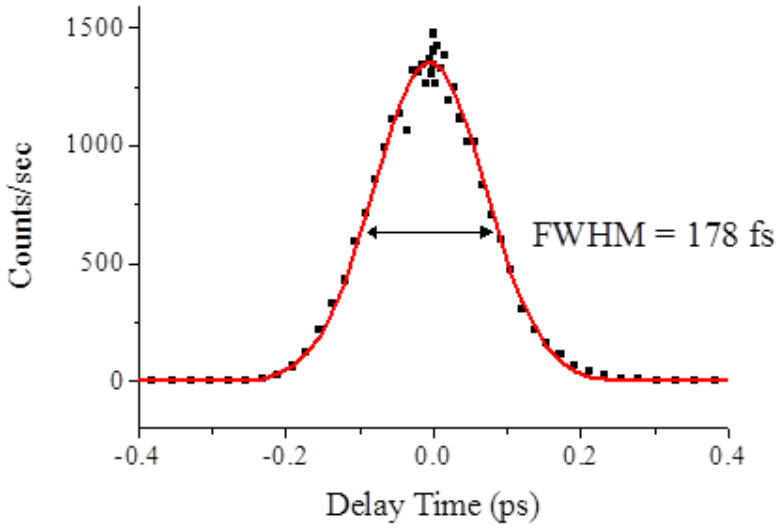

Figure 3.7. Typical IIV-SFG cross-correlation trace of Au as a function of the pump-probe delay time.

3.3.2. Ultrafast Mid-Infrared Transient Absorption Measurements

Ultrafast experiments were carried out in a standard IR pump-IR probe transient absorption scheme according to published procedures.[8-11] The tunable infrared

spectrometer is based on a regeneratively amplified Ti:Sapphire laser system (Coherent Legend, 800 nm, 150 fs, 2.5 mJ/pulse, 1 KHz repetition rate) and an optical parametric amplifier (OPA). An IR-OPA (Clark-MXR) was pumped at 800 nm (1 mJ/pulse) to produce signal and idler outputs at 1380 and 1903 nm, respectively. The signal and idler were collinearly mixed in an $AgGaS_2$ crystal to produce, by difference-frequency generation, tunable mid-IR pulses with a full width at half-maximum (FWHM) of ~120 cm^{-1} and pulse energy of ~2 μJ at 5000 nm. The mid-IR pulses were split with an 80/20 beamsplitter to produce pump and probe pulses, respectively. The IR probe pulses were attenuated with a beam splitter and ND filters (to ~10 nJ) and chirp-corrected with Ge windows before the sample. The pump and probe beam diameters at the sample were ~350 and 175 μm, respectively, as measured by pinhole transmission. After the sample, the probe (centered at 2000 cm^{-1}) was dispersed in a spectrometer with a resolution of 1.5 nm (15.4 cm^{-1} at 2000 cm^{-1}) and detected with a 32-element mercury cadmium telluride (MCT) array detector. Every other pump pulse was blocked by a synchronized chopper (New Focus 3500) at 500 Hz, and the absorbance change was calculated from sequential pumped vs. unpumped probe pulses.

The instrument response function and zero time delay were determined with a thin Si wafer, which gives an instantaneous mid-IR absorption response after excitation. Typically, the instrument response function was well fit by a Gaussian function with 160 fs fwhm.

3.4. Density Functional Theory Calculations (performed by Victor Batista *et al.* at Yale University)

3.4.1. Density Functional Theory (DFT) Calculations of ReC0A on TiO_2 (001)

DFT calculations were performed by Robert C. Snoeberger, III *et al* with the Vienna Ab Initio Simulation Package.[12,13] Electron exchange and correlation were modeled using the PW91/GGA[14] density function. All calculations employed a plane-wave basis truncated with a 270 eV cutoff, single k-point sampling, and ultrasoft Vanderbilt[15] pseudopotentials. Default convergence criteria were utilized for both the electronic energy and nuclear geometry optimizations.

A three-dimensional periodic slab with dimensions of 1.38 by 0.92 nm^2 in the [010] and [100] directions and a vacuum along the [001] direction was used to represent the TiO_2 (001) surface. The yielded an adsorbate coverage of 0.79 adsorbate/nm^2. The TiO_2 slab contained six layers of atoms and was 0.73 nm thick. The Ti and O atoms were held fixed at their crystal structure positions when calculating the geometry relaxation of the ReC0A adsorbate.[16]

3.4.2. PS-VSFGS Spectra Simulation

A detailed description of the procedure for simulating the VSFG spectra using the *ab initio* parameters of polarizability derivatives and dipole moment derivatives with respect to normal mode coordinates can be found in the previous work of Batista *et al*.[17] For this work, Dequan Xiao *et al.* calculated the χ_{eff} signal for the PPP polarization combination,[18] referring to a P-polarized sum-frequency field, P-polarized visible field, and P-polarized IR field. Before simulating the PS-VSFGS spectra, energy minimization

and normal mode analysis were performed for ReC0A at the density functional theory level, using the B3LYP functional and the LAN2DZ basis set. Dipole derivatives of each vibrational mode were obtained using the keyword "iop(7/33=1)" during a frequency calculation, and polarizability derivatives were obtained by performing the Raman vibrational analysis with the "polar" keyword. All of the above calculations were performed using the Gaussian 09 program.[19]

3.4.3. Density Functional Theory (DFT) calculations of ReCnA on TiO_2 (001)

DFT calculations were performed by Dequan Xiao *et al.* at Yale University. Initially, the plane of the bipyridine chromophore (without the Re metal, Cl and CO ligands) was oriented near the predicted angles deduced from the PS-VSFGS spectra while maintaining a reasonable distance with respect to the rutile TiO_2 (001) surface. A three-dimensional periodic slab with a vacuum in the [001] direction was used to represent the TiO_2 (001) surface. Next, the orientation of the anchoring groups (i.e. $-CH_2-$ and $-COO^-$) was optimized with a MM+ force field implemented in the Hyperchem computational package.[20] The final structure determined in this way was used as an initial guess for a full optimization using the Density Functional Tight-binding (DFTB) theory implemented in DFTB+ computational code.[21] After optimization at the DFTB level, subsequent DFT calculations were performed with the Vienna *Ab Initio* Simulation Package.[13] Electron exchange and correlation were described using the PW91/GGA density functional.[22] All calculations employed a plane-wave basis truncated with a 400 eV cutoff, single k-point sampling, and ultrasoft Vanderbilt[15] pseudopotentials. Default

convergence criteria were utilized for both the electronic energy and nuclear geometry optimizations.

3.5. Vibrational Sum Frequency Generation Spectroscopy Signal Processing Methods

3.5.1. Static Homodyne-detected Vibrational Sum Frequency Generation Spectroscopy

Although detected in the visible range, IR-visible SFG spectra are typically represented in the infrared region so that the resonant enhancement as a function of the IR wavelength can be easily discerned. The appropriate infrared wavelengths can be easily calculated via Equation 3.3:

$$\omega_{IR}(cm^{-1}) = (\frac{1}{\lambda_{SFG}} - \frac{1}{\lambda_{vis}}) \times 10^{7} \qquad (3.3)$$

Sample SFG spectra were also corrected as a function of IR intensity. SFG nonresonant spectra from gold were obtained previous to collecting sample data for each IR wavelength window used. The nonresonant, broadband gold spectra are assumed to represent the IR window generated by the TOPAS-C and were thus used to normalize the sample SFG spectra for IR intensity.

3.5.2. Static Phase Sensitive-detected Vibrational Sum Frequency Generation Spectroscopy

In PS-VSFGS, the obtained spectrum is in fact an interferogram resulting from the interference between the sample SFG signal and the local oscillator (LO) SFG signal.

In order to extract the relevant molecular information, a signal processing procedure was developed based on published procedures.[23-25]

The information contained in the PS-VSFGS spectrum is:

$$I_{PS-VSFGS} = \left|\chi_s^{(2)} E_{Vis} E_{IR}\right|^2 + \left|\chi_{lo}^{(2)} E_{Vis} E_{IR}\right|^2 + 2\,\mathrm{Re}[\chi_{lo}^{(2)} \chi_s^{(2)} E_{vis}^2 E_{IR}^2 e^{i2\pi\omega\tau}] \qquad (3.4)$$

where the first two terms are the homodyne contributions from the sample and LO, respectively, and the last term (the so-called "cross-term") contains the desired $\chi_s^{(2)}$ information. Each interferogram was first inverse Fourier transformed into the time domain in order to separate the homodyne contributions centered at t = 0 from the cross-terms centered at t = ± τ, where τ is the delay between the sample and LO SFG signals. The cross-term at t = τ was subsequently isolated through the implementation of a boxcar function, and the resulting real and imaginary spectra were then Fourier transformed back into the frequency domain.

After the removal of the homodyne contributions, the spectra must still be corrected in order to remove the LO portion of the cross-term, as well as any effects of the frequency-dependent incident beam intensities. This was accomplished by normalizing each sample spectrum against a standard sample of known $\chi^{(2)}$; in this case, a gold film was used. Since gold exhibits no resonance in the investigated spectral region, its response is both flat and real, so that $\chi_{Au}^{(2)}$ can be considered a constant. The sample spectra were therefore normalized by the processed gold spectrum to yield the $\chi_s^{(2)}$ of interest:

$$\frac{\chi_{lo}^{(2)} \chi_s^{(2)} E_{vis}^2 E_{IR}^2 e^{i2\pi\omega\tau}}{\chi_{lo}^{(2)} \chi_{Au}^{(2)} E_{vis}^2 E_{IR}^2 e^{i2\pi\omega\tau}} e^{i\phi} = \frac{\chi_s^{(2)}}{\chi_{Au}^{(2)}} e^{i\phi} \qquad (3.5)$$

The $e^{i\phi}$ term is included to describe any phase difference between the sample and gold spectra which can result from slightly different positioning between the ReCnA/TiO_2 and gold samples. This phase difference was subsequently corrected by the application of a phasing factor for all data presented here. The resulting $\chi_s^{(2)}$ contains both real and imaginary parts, where the latter corresponds to the resonant molecular response and the former is the derivative of the imaginary part plus any nonresonant response.

3.6. References

(1) Pfennig, B. W.; Chen, P. Y.; Meyer, T. J. *Inorg Chem* **1996**, *35*, 2898.

(2) Walters, K. A.; Gaal, D. A.; Hupp, J. T. *Journal of Physical Chemistry B* **2002**, *106*, 5139.

(3) Yan, S. G.; Prieskorn, J. S.; Kim, Y.; Hupp, J. T. *Journal of Physical Chemistry B* **2000**, *104*, 10871.

(4) Liu, G.-k., Xiamen University, 1996.

(5) Pan, S.; Castner, D. G.; Ratner, B. D. *Langmuir* **1998**, *14*, 3545.

(6) Lagutchev, A.; Hambir, S. A.; Dlott, D. D. *Journal of Physical Chemistry C* **2007**, *111*, 13645.

(7) Ghosh, A.; Smits, M.; Bredenbeck, J.; Dijkhuizen, N.; Bonn, M. *Rev Sci Instrum* **2008**, *79*.

(8) Anderson, N. A.; Asbury, J. B.; Hao, E.; Ai, X.; Lian, T. *Proceedings - Electrochemical Society* **2001**, *2001-10*, 97.

(9) Wang, Y.; Asbury, J. B.; Lian, T. *J. Phys. Chem. A* **2000**, *104*, 4291.

(10) Ghosh, H. N.; Asbury, J. B.; Weng, Y.; Lian, T. *J. Phys. Chem. B* **1998**, *102*, 10208.

(11) Huang, J.; Stockwell, D.; Boulesbaa, A.; Guo, J.; Lian, T. *J. Phys. Chem. C* **2008**, *112*, 5203.

(12) Anfuso, C. L.; Snoeberger, R. C.; Ricks, A. M.; Liu, W. M.; Xiao, D. Q.; Batista, V. S.; Lian, T. Q. *Journal of the American Chemical Society* **2011**, *133*, 6922.

(13) Kresse, G.; Furthmuller, J. *Physical Review B* **1996**, *54*, 11169.

(14) Perdew, J. P. In *Electronic Structure of Solids '91*; P. Ziesche, H. E., Ed.; Akademie Verlag: Berlin, 1991, p 11.

(15) Vanderbilt, D. *Physical Review B* **1990**, *41*, 7892.

(16) Swope, R. J.; Smyth, J. R.; Larson, A. C. *American Mineralogist* **1995**, *80*, 448.

(17) Xiao, D. F., L.; Batista, V. S.; Yan, E. C. Y. *Journal of Molecular Biology* **2012; in press**.

(18) Zhuang, X.; Miranda, P. B.; Kim, D.; Shen, Y. R. *Physical Review B* **1999**, *59*, 12632.

(19) Frisch, M. J. T., G. W.; Schlegel, H. B.; Scuseria, G. E.; Robb, M. A.; Cheeseman, J. R.; Scalmani, G.; Barone, V.; Mennucci, B.; Petersson, G. A.; Nakatsuji, H.; Caricato, M.; Li, X.; Hratchian, H. P.; Izmaylov, A. F.; Bloino, J.; Zheng, G.; Sonnenberg, J. L.; Hada, M.; Ehara, M.; Toyota, K.; Fukuda, R.; Hasegawa, J.; Ishida, M.; Nakajima, T.; Honda, Y.; Kitao, O.; Nakai, H.; Vreven, T.; Montgomery, J. A., Jr.; Peralta, J. E.; Ogliaro, F.; Bearpark, M.; Heyd, J. J.; Brothers, E.; Kudin, K. N.; Staroverov, V. N.; Kobayashi, R.; Normand, J.; Raghavachari, K.; Rendell, A.; Burant, J.

C.; Iyengar, S. S.; Tomasi, J.; Cossi, M.; Rega, N.; Millam, J. M.; Klene, M.; Knox, J. E.; Cross, J. B.; Bakken, V.; Adamo, C.; Jaramillo, J.; Gomperts, R.; Stratmann, R. E.; Yazyev, O.; Austin, A. J.; Cammi, R.; Pomelli, C.; Ochterski, J. W.; Martin, R. L.; Morokuma, K.; Zakrzewski, V. G.; Voth, G. A.; Salvador, P.; Dannenberg, J. J.; Dapprich, S.; Daniels, A. D.; Farkas, O.; Foresman, J. B.; Ortiz, J. V.; Cioslowski, J.; Fox, D.; Revision A.1 ed.; Gaussian, Inc.: Wallingford, CT, 2009.

(20) Hypercube, I. 1115 NW 4th Street, Gainesville, Florida 32601, USA.

(21) Aradi, B.; Hourahine, B.; Frauenheim, T. *Journal of Physical Chemistry A* **2007**, *111*, 5678.

(22) Perdew, J. P. In *Electronic Structure of Solids '91*; P. Ziesche, H. E., Ed.; Akademie Verlag, Ed. Berlin, 1991, p 11.

(23) Yamaguchi, S.; Tahara, T. *Journal of Chemical Physics* **2008**, *129*.

(24) Nihonyanagi, S.; Yamaguchi, S.; Tahara, T. *Journal of Chemical Physics* **2009**, *130*.

(25) Stiopkin, I. V.; Jayathilake, H. D.; Bordenyuk, A. N.; Benderskii, A. V. *Journal of the American Chemical Society* **2008**, *130*, 2271.

Chapter 4. Orientation of a Rhenium Bipyridyl CO_2-Reduction Catalyst Adsorbed onto Rutile Single Crystalline TiO_2 (001)

4.1. Introduction

Knowledge of the orientation and binding of molecules to semiconductor surfaces is vital to elucidating the mechanism of electron transfer (ET) in catalysis, molecular electronics, and dye-sensitized solar cells (DSSCs).[1-5] In these systems, the rate of electron transfer is typically described using Marcus theory, where a determining factor in the ET rate is the matrix element describing the coupling between the donor and acceptor electronic states.[6-9] This coupling is directly correlated with the adsorption geometry of the molecule as it anchors to the semiconductor surface. It is therefore of great fundamental and practical interest to elucidate the average molecular orientation in adsorbate-semiconductor systems, in order to gain a more complete understanding of the electron transfer process.

Previously, our group investigated the electron transfer properties of numerous adsorbate-semiconductor systems using transient infrared and visible pump-probe absorption spectroscopy.[10-14] These systems were typically characterized for their potential use in dye-sensitized solar cells (DSSCs). One such system consists of a series of rhenium bipyridyl complexes, $Re(L)(CO)_3Cl$ [L = 2,2'-bipyridine-4,4'-$(CH_2)_n$-COOH, n = 0 – 4] (abbreviated as ReCnA). These molecules are known to adsorb to the semiconductor surface through their carboxylate anchoring groups, which are attached to the bipyridine ligands through methyl spacers of varying lengths (n-CH_2 units).[11,15,16] These complexes have been shown to inject electrons into the semiconductor at different

rates depending on the value of n.[11,16] However, it is currently unclear if increasing the number of methyl linkers has a significant effect on the average conformation of these complexes on the surface. As a change in the molecular orientation would certainly affect the electron transfer rate, elucidation of the average molecular orientation of the ReCnA series on a semiconductor may aid in gaining a more complete understanding of the electronic coupling in these systems.

This system is also of particular interest due to its potential use as a catalyst for the selective reduction of CO_2 to CO, which is currently a problem of great technological concern.[17] Several tricarbonyl rhenium complexes with modified bipyridine ligands have been developed and explored for the photo- and electrocatalytic reduction of CO_2.[18-26] Interestingly, a rhenium bipyridyl complex was recently shown to have increased catalytic reductive ability when adsorbed to TiO_2 electrodes.[27] However, the covalent attachment of these electrocatalysts on semiconductor electrodes has yet to be characterized at the molecular level. The development of similar photodriven CO_2 reduction systems will likely involve the attachment of catalysts to semiconductor photoelectrodes. As such, a study on the conformation of ReC0A and other molecules in the ReCnA series on a semiconductor surface should prove generally useful in the design and improvement of reductive catalytic systems.

Perhaps the most well-characterized semiconductor in the areas of electron transfer and catalysis is titanium dioxide, or TiO_2, which has been extensively studied,[28-38] including numerous studies on electron transfer at the molecule/TiO_2 interface.[5,10,39-41] Indeed, both electron transfer and catalytic studies of the rhenium bipyridine complexes mentioned here have involved their immobilization on nanocrystalline TiO_2. However,

nanocrystalline TiO_2 consists of numerous facets and crevices on the nanometer or even micron scale, depending on its preparation, presumably leading to a large range of molecular orientations. To gain a fundamental understanding of the molecule-semiconductor interactions, it is more useful to study a more ordered surface, such as single crystalline TiO_2. Single crystal TiO_2 has an atomically flat, well-characterized surface that has been studied both experimentally and theoretically.[28,31,34] Its ability to adsorb sensitizing dyes similar to ReCnA has also been investigated.[42-47] The ReCnA/TiO_2 single crystal interface therefore represents a model system which preserves many features desirable in an electrocatalyst or DSSC while still retaining the structural simplicity necessary for thorough spectroscopic and theoretical characterization.

Vibrational sum frequency generation spectroscopy (VSFGS) has been recognized in recent years as a useful technique for determining molecular orientation at interfaces.[48-50] A second-order optical technique, it is forbidden in media with inversion symmetry but allowed at interfaces where the inversion symmetry is necessarily broken. For an ordered layer of molecules on a surface, the VSFG signal depends on the polarization of $\omega_{vis,}$ $\omega_{IR,}$ and ω_{SF} with respect to the vibrational and/or electronic transition moment. By monitoring the VSFG response as a function of fundamental and generated polarizations, the projection of the transition moment on the laboratory axis can be determined. These results can then be used to screen calculated adsorption geometries. The molecular orientation at the semiconductor surface can thus be obtained via this synergy of experiment and theory.

In this work, we have investigated the average molecular orientation of ReC0A on a rutile TiO_2 (001) single crystal using vibrational sum frequency generation

spectroscopy; the structure of ReC0A is shown in Figure 4.1. The (001) surface was chosen for its C_4 symmetry, which simplifies the analysis compared to less symmetric TiO_2 cuts. ReC0A was chosen for the initial orientation studies in order to establish the experimental technique needed to determine the molecular orientation.

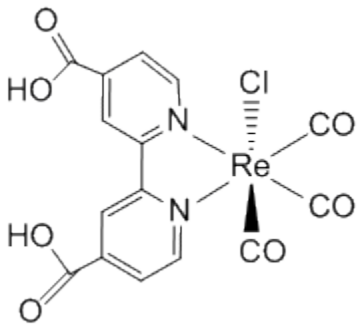

Figure 4.1. Schematic structure of ReC0A.

4.2. Results and Discussion

4.2.1. Static UV-visible and FTIR absorption spectra of ReC0A on nanocrystalline TiO_2

Figure 4.2 shows the UV-visible and FTIR spectra of ReC0A on nanocrystalline TiO_2. The UV-visible absorption spectrum shows a low-lying metal-to-ligand-charge-transfer (MLCT) band from the d-orbitals of Re(I) to the π^* orbital of bipyridine at approximately 420 nm. The FTIR spectrum exhibits three CO stretching modes: a symmetric a'(1) stretch at 2040 cm^{-1} and an unresolved band at ~1925 cm^{-1} consisting of an anti-symmetric a" stretch and a symmetric a'(2) stretch.[51] Fitting the 1925 cm^{-1} band to two Gaussian functions gives the a" mode at ~1940 cm^{-1} and the a'(2) at ~1910 cm^{-1}. These three carbonyl stretches are ideal probes in VSFGS due to their strong IR and

Raman cross sections and their position in between the congested fingerprint and C-H stretching regions. Additionally, their transition dipole moments lie reasonably orthogonal to each other in the molecular *xyz* axis system. Since the SF signal intensity is critically dependent on the orientation of the dipoles with respect to the incident IR polarization, these bands make an ideal system for determining the average molecular orientation of ReC0A on TiO_2 (001).

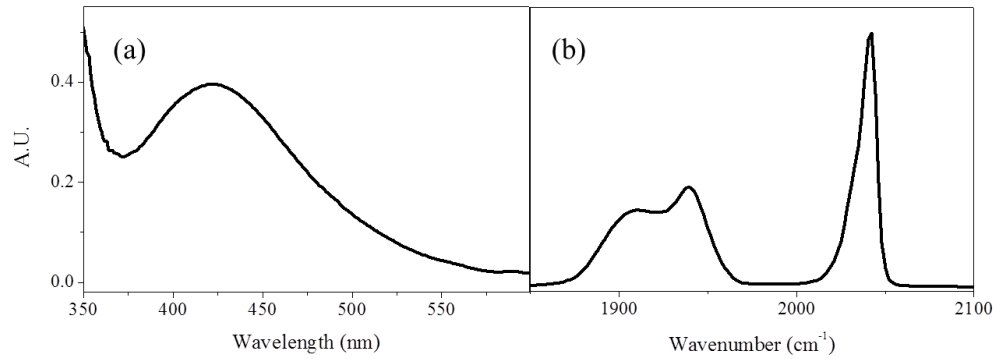

Figure 4.2. (a) UV-visible absorption spectrum of ReC0A on nanocrystalline TiO_2, showing the Re(I)-to-π* MLCT band at 420 nm. (b) FTIR spectrum of ReC0A on nanocrystalline TiO_2, showing a symmetric a'(1) stretch at 2040 cm^{-1} and an unresolved band at ~1925 cm^{-1} consisting of an anti-symmetric a" stretch at 1939 cm^{-1} and a symmetric a'(2) stretch at 1910 cm^{-1}.

4.2.2. VSFGS spectra of ReC0A on TiO_2 (001)

4.2.2.1. Spectral Processing Details

The vibrational sum frequency generation spectroscopy spectrum of ReC0A on TiO_2 (001) in the PPP polarization combination (indicating the polarization of the sum frequency, visible, and infrared fields, respectively) is shown in Figure 4.3a. In general, the intensity of a VSFGS spectrum is given by:

$$I(\omega_{SF}) \propto \left|\chi_{eff}^{(2)}\right|^2 I_{vis}(\omega_{vis}) I_{IR}(\omega_{IR}) \qquad (4.1)$$

where $I_{vis}(\omega_{vis})$ and $I_{IR}(\omega_{IR})$ are the intensities of the two incident electric fields. When using a broadband IR source, which does not exhibit a flat intensity over the investigated spectral region, it is necessary to normalize the VSFGS spectrum for the incident IR intensity. The incident visible intensity, being spectrally narrow, is assumed to be a constant as a function of frequency. Typically, the IR intensity is approximated from the SFG response of a sample which exhibits no vibrational resonances in the investigated spectral region. In this case, the SFG nonresonant spectrum of gold was obtained previous to collecting sample data and assumed to represent the incident IR spectrum. Using this method, Figure 4.3b shows the IR spectrum used to generate the ReC0A/TiO_2 (001) VSFGS spectrum shown in Figure 4.3a. Figure 4.3c shows the ReC0A/TiO_2 (001) VSFGS spectrum after it has been normalized by the IR spectral intensity shown in Figure 4.3b. This normalized spectrum is an accurate representation of the ReC0A $\chi^{(2)}$ response generated in the PPP polarization combination. Measurements of the $\chi^{(2)}$ response for multiple polarization combinations can be used to determine the average molecular orientation of ReC0A on TiO_2 (001).

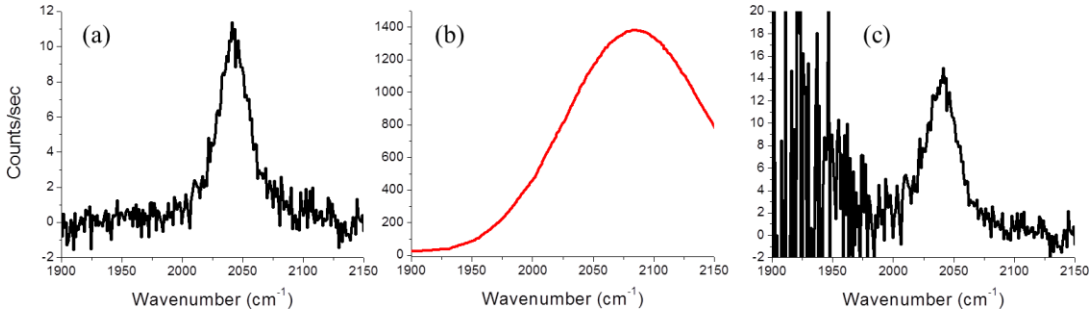

Figure 4.3. (a) VSFGS spectrum of ReC0A on TiO_2 (001) in the PPP polarization combination. (b) SFG nonresonant spectrum of gold (PPP) using the same incident IR window used to collect the spectrum in (a). The gold nonresonant response is flat over this spectral region and is assumed to represent the IR intensity. (c) VSFGS spectrum of ReC0A on TiO_2 (001) shown in (a) after normalization for IR intensity. The noise enhancement below 2000 cm^{-1} is due to the low IR intensity in this spectral region.

Figure 4.3c also illustrates a problem that can arise as a result of the limited IR bandwidth. Since the IR spectral window is centered at ~2075 cm^{-1}, the region below ~2000 cm^{-1} exhibits excessive noise enhancement in the normalized VSFGS spectrum, because the mid-IR intensity is below threshold levels for sufficient SF signal generation. In order to properly investigate all three carbonyl stretches for ReC0A, it is therefore necessary to collect VSFGS spectra using several IR windows. Once again, a gold standard sample was used to collect wavelength-independent nonresonant SFG spectra at different IR peak wavelengths in the PPP polarization combination. Since the gold SF response is flat over the investigated spectral region, these spectra were used to normalize the VSFGS spectra of ReC0A/TiO_2 (001) in every polarization combination. The nonresonant gold spectra thus provide a method of intensity normalization and scaling

without compromising data quality due to low IR intensity at certain frequencies. The normalized ReC0A/TiO_2 (001) VSFGS spectra could then be pieced together over several spectral windows.

Finally, the resolution of the instrumentation must be compared with the actual spectral resolution of the experiment. In our experiment, the VSFGS spectra are detected with a CCD camera with a horizontal resolution of approximately 1.2 cm^{-1}. However, the spectral resolution in a VSFGS experiment is determined by the bandwidth of the upconverting visible pulse; in this case, approximately 10 – 12 cm^{-1}. Therefore, after normalization, all VSFGS spectra were adjacently averaged over 10 cm^{-1} in order to reduce noise and more accurately reflect the resolution of the experiment.

4.2.2.2. Processed VSFGS Spectra of ReC0A on TiO_2 (001)

Figure 4.4 shows the normalized and averaged ReC0A/TiO_2 (001) VSFGS spectra when ω_{SF} = 690 nm for the PPP, SSP, and SPS polarization combinations, along with the FTIR spectrum of ReC0A on nanocrystalline TiO_2. No discernible signal is seen in either the SSP or the SPS polarization combination for any vibrational modes. The PPP spectrum shows a clear peak at ~2040 cm^{-1}, corresponding to the totally symmetric a'(1) stretch, while the two lower frequency modes are absent.

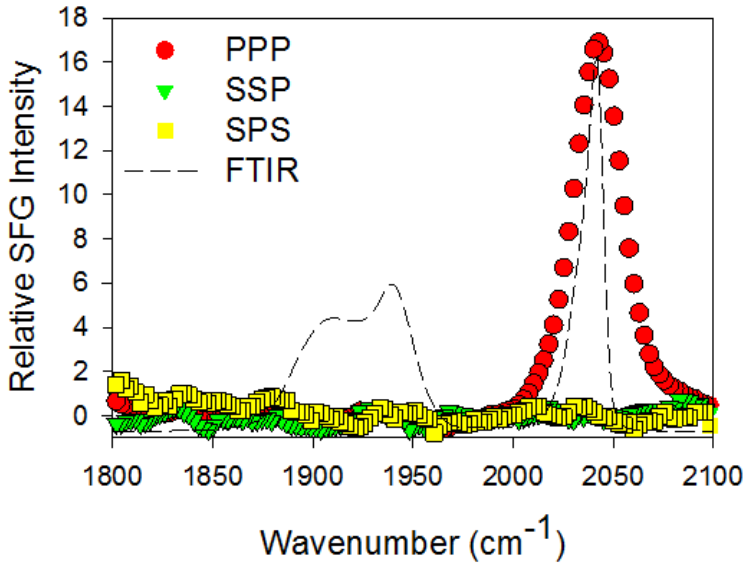

Figure 4.4. VSFGS spectra of ReC0A on TiO_2 (001) when ω_{SF} = 690 nm for three polarization combinations: PPP (red circles), SSP (green triangles), and SPS (yellow squares). Also shown for comparison is the FTIR spectrum of ReC0A on nanocrystalline TiO_2 (black dashed line).

Several factors may contribute to the lack of the lower frequency modes. Assuming the molecules are oriented randomly around the TiO_2 surface normal, vibrations perpendicular to the surface normal will have no net contribution for a surface with C_4 symmetry, which may lead to the absence of certain modes. Additionally, vibrational/electronic coupling may preferentially enhance certain vibrations in the SFG spectrum in double resonance or near-double resonance conditions. Doubly resonant enhancement of the SFG signal can occur if ω_{IR} is resonant with a vibrational mode and either ω_{vis} or ω_{SF} is near an electronic transition of the molecule. The magnitude of this enhancement depends on the coupling of the vibrational and electronic transitions.[52,53]

Doubly resonant SFG spectra thus yield information about the vibrational modes and vibrational/electronic coupling of a molecule at an interface.

4.2.2.3. Doubly-resonant VSFGS Study

As discussed in detail in Chapter 2, in infrared-visible VSFGS where the incident infrared frequency is in resonance with a particular vibrational mode of the molecule, the SF response is proportional to the product of the IR and anti-Stokes Raman transition moments for that mode. In the case where either ω_{vis} or ω_{SF} approaches an electronic transition of the molecule, the Raman polarizability also becomes resonant. The molecule thus no longer goes through a so-called virtual state during the SF process, but rather through a resonant electronic transition of the molecule, as shown in Figure 4.5. The vibrational modes associated with this electronic transition thus exhibit a greatly enhanced SF response, as determined by their Frank-Condon overlap. According to the Borne-Oppenheimer approximation, only totally symmetric vibrational modes can be efficiently excited under doubly-resonant or near-doubly-resonant VSFGS conditions.[54]

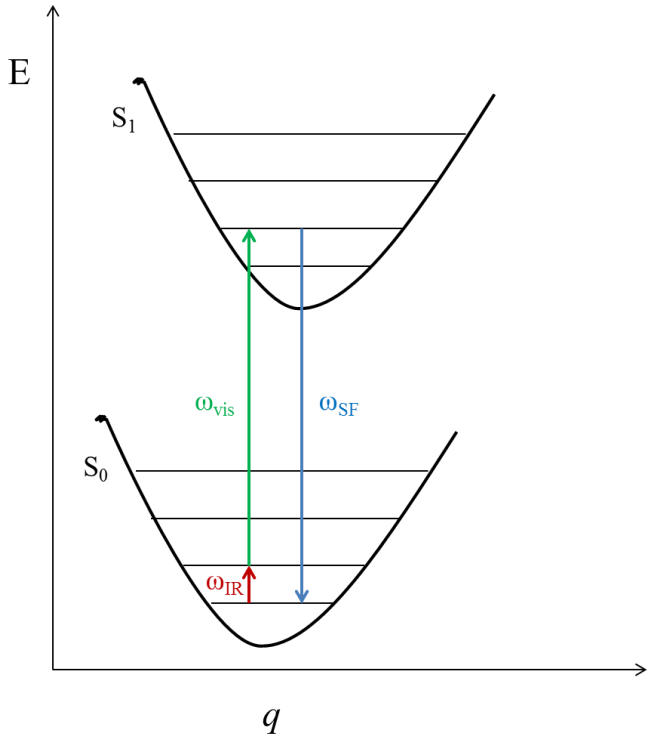

Figure 4.5. Model potential energy diagram for the doubly-resonant SF process as a function of normal coordinate *q*.

In this context, one possible explanation for the lack of the lower frequency modes is near-resonance of the ω_{SF} beam with the MLCT transition at ~420 nm.[48,50,55,56] Raman spectra of related complexes show that while all three CO stretching modes are active when the excitation beam is off-resonant with the electronic transition (λ_{ex} = 1064 nm), only the a'(1) mode is significantly enhanced when the excitation beam is near or at resonance.[57] This has been attributed to a negligible change in equilibrium position of the a" and a'(2) modes between the ground and the metal(Re)-to-ligand(bpy) charge transfer (MLCT) excited state.[58] Additionally, the a'(1) stretch has a large projection along the 420 nm MLCT transition moment, whereas the a" and a'(2) modes are nearly perpendicular to it. Consequently only the a'(1) mode would be expected to be enhanced

by coupling with the MLCT transition. To investigate the extent of resonant enhancement due to the MLCT transition, we have examined the dependence of the SFG spectra on ω_{SF}.

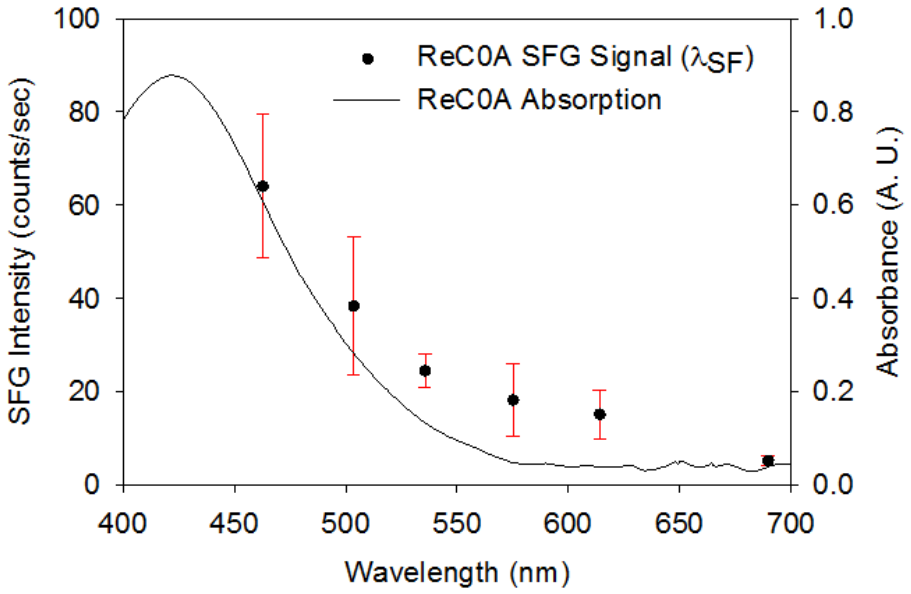

Figure 4.6. VSFGS intensity of ReC0A on TiO_2 (001) at 2040 cm^{-1} in the PPP polarization combination as a function of the sum frequency wavelength (black circles, left axis). The intensities have been corrected for grating and CCD efficiencies. The larger errors bars at shorter wavelengths can be attributed to sample degradation which led to larger variations in peak intensity. Also shown for comparison is the UV-visible absorption spectrum of ReC0A on nanocrystalline TiO_2 (solid black line, right axis).

Figure 4.6 shows the UV-visible absorption spectrum of ReC0A on nanocrystalline TiO_2 compared with the SFG peak intensity at 2040 cm^{-1} (PPP) as a function of the sum frequency wavelength. The larger errors bars at shorter wavelengths can be attributed to sample degradation which led to variations in peak intensity. There is

a clear increase in the SFG signal as the sum frequency approaches the MLCT band at ~420 nm. This increase correlates well with the UV-vis spectrum, indicating that the SFG signal of the a'(1) mode may be enhanced due to coupling with the MLCT band. SFG polarization spectra of ReCOA/TiO_2 (001) recorded with λ_{SF} = 500 nm also show a lack of intensity of the a" and a'(2) modes for all polarization combinations and an identical polarization dependence of the a'(1) mode, as shown in Figure 4.7. In the case of the selective enhancement of the a'(1) mode, the other modes may remain too weak to detect with our current signal-to-noise. This near-resonance effect may thus explain the lack of the lower frequency modes in the VSFGS spectra.

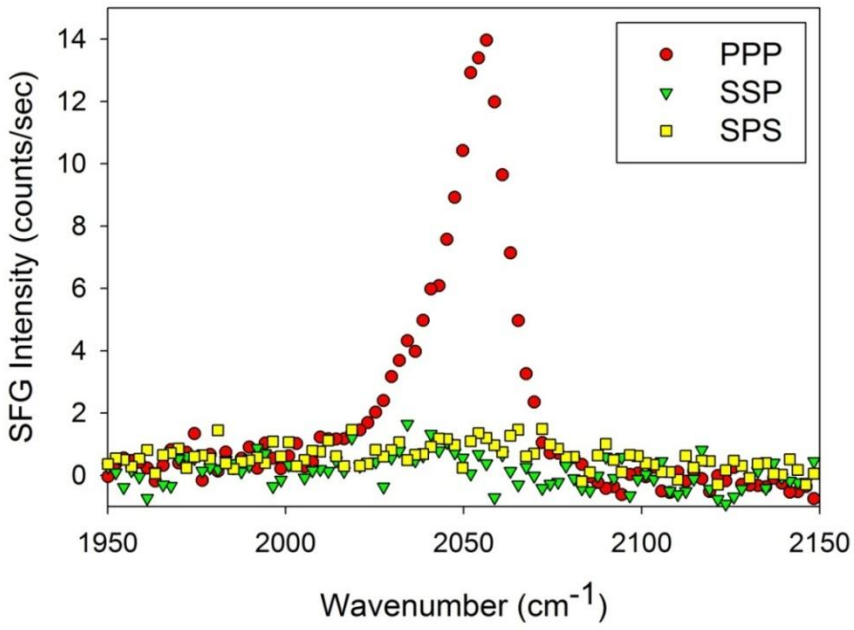

Figure 4.7. SFG spectra of the a'(1) symmetric stretch of ReC0A on TiO_2 (001) as a function of ω_{IR} with λ_{SF} = 500 nm for three polarization combinations: PPP (red circles), SSP (green triangles), and SPS (yellow squares). The polarization dependence is identical to that when λ_{SF} = 690 nm (shown in Figure 4.4).

4.2.3. Orientation Analysis of ReC0A on TiO_2 (001)

4.2.3.1. Theoretical Considerations

In order to determine the orientation of ReC0A from the SFG spectra, the SFG response of the totally symmetric a'(1) stretch at 2040 cm^{-1} was modeled as a function of orientation angle for the three polarization combinations. The orientation angle is defined as the average tilt angle between the molecular c-axis and the TiO_2 surface normal (z-axis), as illustrated in Figure 4.8. Although the details of the orientation analysis are described in Chapter 2, they will be briefly outlined here in relation to the specific system of ReC0A on TiO_2 (001).

The intensity of the sum frequency signal is given by Equation 4.1. The effective nonlinear susceptibility $\chi_{eff}^{(2)}$ is related to individual susceptibility elements $\chi^{(2)}_{ijk}$ (i,j,k = x,y,z) by:

$$\chi_{eff}^{(2)} = \left[\hat{\mathbf{e}}(\omega)\cdot\mathbf{L}(\omega)\right]\cdot\chi^{(2)}:\left[\mathbf{L}(\omega_1)\cdot\hat{\mathbf{e}}(\omega_1)\right]\left[\mathbf{L}(\omega_2)\cdot\hat{\mathbf{e}}(\omega_2)\right] \qquad (4.2)$$

where $\hat{\mathbf{e}}(\Omega)$ is the unit polarization vector, $\mathbf{L}(\Omega)$ is the Fresnel factor at frequency Ω, and $\chi^{(2)}$ is the nonlinear susceptibility tensor. Although there are 27 $\chi^{(2)}$ elements, for a molecule containing a mirror plane on a surface with C_4 symmetry – as in the case of ReC0A/TiO_2 (001) – only four independent nonzero $\chi^{(2)}_{ijk}$ elements remain: χ_{zzz}, χ_{xxz} = χ_{yyz}, χ_{xzx} = χ_{yzy}, and χ_{zxx} = χ_{zyy}, where z is the surface normal.[59] These independent components can be determined by measuring the sum-frequency signal using four different input and output polarizations: SSP, SPS, PSS, and PPP.

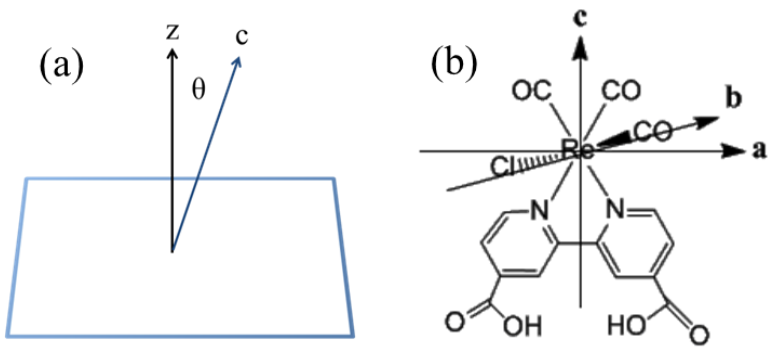

Figure 4.8. (a) Illustration of the average molecular orientation θ, defined as the average tilt angle between the molecular c-axis and the TiO_2 surface normal (z-axis). (b) Molecular axis system for ReC0A. The b-c plane forms the symmetry plane of the molecule; the a-axis is perpendicular to this plane.

For a given molecule at an interface, the nonzero $\chi^{(2)}_{ijk}$ elements are related to the second order hyperpolarizability elements $\beta^{(2)}_{\alpha\beta\gamma}$ according to:

$$\chi^{(2)}_{ijk} = N_s \sum_{\alpha\beta\gamma=abc} \langle R(\psi)R(\theta)R(\phi)\rangle \beta_{\alpha\beta\gamma} \qquad (4.3)$$

where N_s is the molecule number density, $R(\Omega)$ is a rotation transformation matrix used to transform from the molecular coordinates ($\alpha\ \beta,\gamma$) to the laboratory coordinates (x,y,z) through the Euler angles ($\theta,\ \psi\ ,\phi$), and the operator $\langle\ \rangle$ denotes an orientational ensemble average. Individual $\beta^{(2)}_{\alpha\beta\gamma}$ elements are proportional to the product of the IR and Raman transition dipole moments for a particular vibrational transition. In the case of the totally symmetric a'(1) stretch of ReC0A on TiO_2 (001), we can assume that the Raman transition obtains most of its character from the nearby MLCT band at 420 nm. This postulation is strengthened by the results of the near-doubly-resonant study shown in Figure 4.6. In this case, the Raman transition lies primarily along the c-axis of the molecule (as shown in Figure 4.8b). The IR transition dipole of the a'(1) mode,

meanwhile, lies in the c-b plane at an angle of 28° from the c-axis.[60] Therefore, we can identify two dominant hyperpolarizability elements for the totally symmetric a'(1) mode: β_{ccc} and β_{ccb}.

Assuming these two hyperpolarizability elements, expressions for the relevant $\chi^{(2)}$ elements can be written using Equation 4.3. To determine the necessary $\chi^{(2)}$ elements as a function of the orientation angle θ, we must average over the relevant ϕ and ψ angles. It is reasonable to assume that ReC0A may bind along any row of Ti atoms, so that the value of ϕ will always be ($n\pi/4$), where *n* is an integer. Additionally, the molecule is known to bind to the surface with two functional groups and thus is not free to rotate, so that ψ = 0 or π. Using these values of ϕ and ψ, we can generate the appropriate $\chi^{(2)}$ elements as a function of the orientation angle and hyperpolarizability elements:

$$\chi_{zzz} = \cos^3(\theta) \cdot \beta_{ccc} \tag{4.4}$$

$$\chi_{xxz} = \chi_{xzx} = \chi_{zxx} = \frac{1}{2}\cos(\theta)\sin^2(\theta) \cdot \beta_{ccc} \tag{4.5}$$

As seen in Equation 4.5, β_{ccb} does not contribute to the $\chi^{(2)}$ elements. These terms go to zero due to the assumption that the configurations with ψ = 0 and ψ = π are equally likely, which is conceptually equivalent to imposing a C_2 rotation for the molecule. In this case, according to symmetry arguments, all contributions with an odd number of *b* elements would go to zero.[61] Using these $\chi^{(2)}$ elements, the relative PPP, SSP, and SPS intensities were simulated as a function of orientation angle; these results are shown in Figure 4.9.

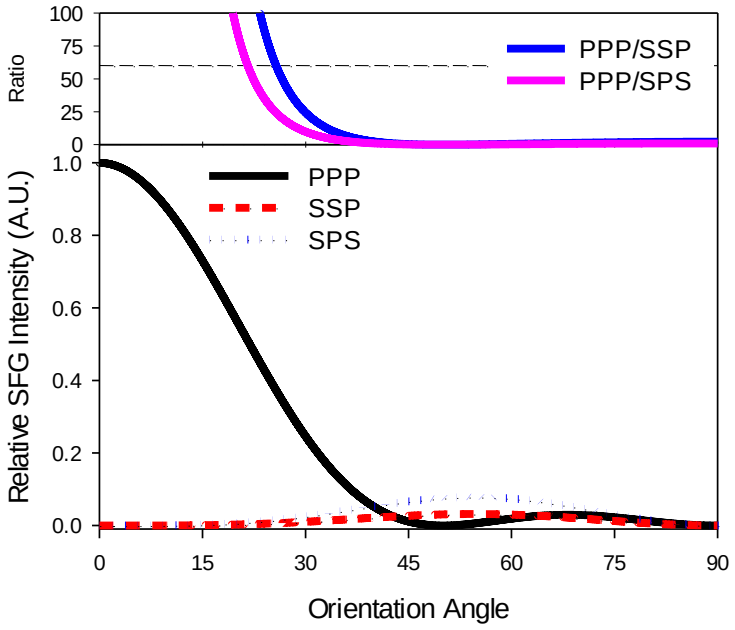

Figure 4.9. (lower trace) Modeled SFG intensity for the three polarization combinations as a function of the orientation angle: PPP (solid black line), SSP (red dashed line), and SPS (dotted blue line). (upper trace) Predicted PPP/SSP and PPP/SPS ratios as a function of orientation angle.

4.2.3.2. Molecular Orientation Determination

The lower trace of Figure 4.9 shows the predicted relative SF intensities of the totally symmetric a'(1) stretch at 2040 cm^{-1} in the PPP, SSP, and SPS polarization combinations as a function of orientation angle. The upper trace displays the predicted PPP/SSP and PPP/SPS ratios, which can be used to deduce the average molecular orientation angle. According to this model the SFG signal in the PPP combination should be dominant at smaller orientation angles (i.e. closer to the surface normal), whereas at larger orientation angles the a'(1) mode should show appreciable signal in all three polarization combinations. As our signal-to-noise is sufficient to detect a minimum

PPP/SPS ratio of 60:1, this analysis yields an orientation angle θ of ~0 – 22° from the surface normal.

4.2.4. Density Functional Theory (DFT) calculations of ReC0A on TiO_2 (001)

In support of the experimental work, DFT calculations were performed by Robert C. Snoeberger, III *et al.* in the Victor Batista group at Yale University in order to obtain an atomistic model of the ReC0A/TiO_2 (001) interface.[62] Several possible ReC0A binding motifs were investigated, and two optimized geometries with similar energetics were found, as shown in Figure 4.10. Both exhibit orientation angles that lie within the experimentally determined range of 0 – 22°. Both structures bind to the TiO_2 surface by ligation of the carboxylate groups to tetracoordinated Ti centers. However, one optimized structure predicts that both carboxylate linkers of ReC0A are coordinated to Ti atoms in a monodentate mode (Figure 4.10a), whereas the other predicts an optimized structure where one linker is coordinated to a Ti ion in a monodentate mode while the other is interacting with a bridging hydroxyl and only semi-coordinated to the Ti ion (Figure 4.10b). The tridentate isomer (Figure 4.10b) is predicted to be the global minimum and have an orientation angle of 11.7°, while the bidentate isomer (Figure 4.10a) is calculated to be 4.85 kcal/mol higher in energy with an orientation angle of 0.9°. Both structures are energetically equivalent within the assumed error of the computation and it is likely that the observed SFG signal results from a combination of the two isomers. Overall, the DFT calculations agree very well with the experimental data and predict an orientation angle in the range of 0 – 22°.

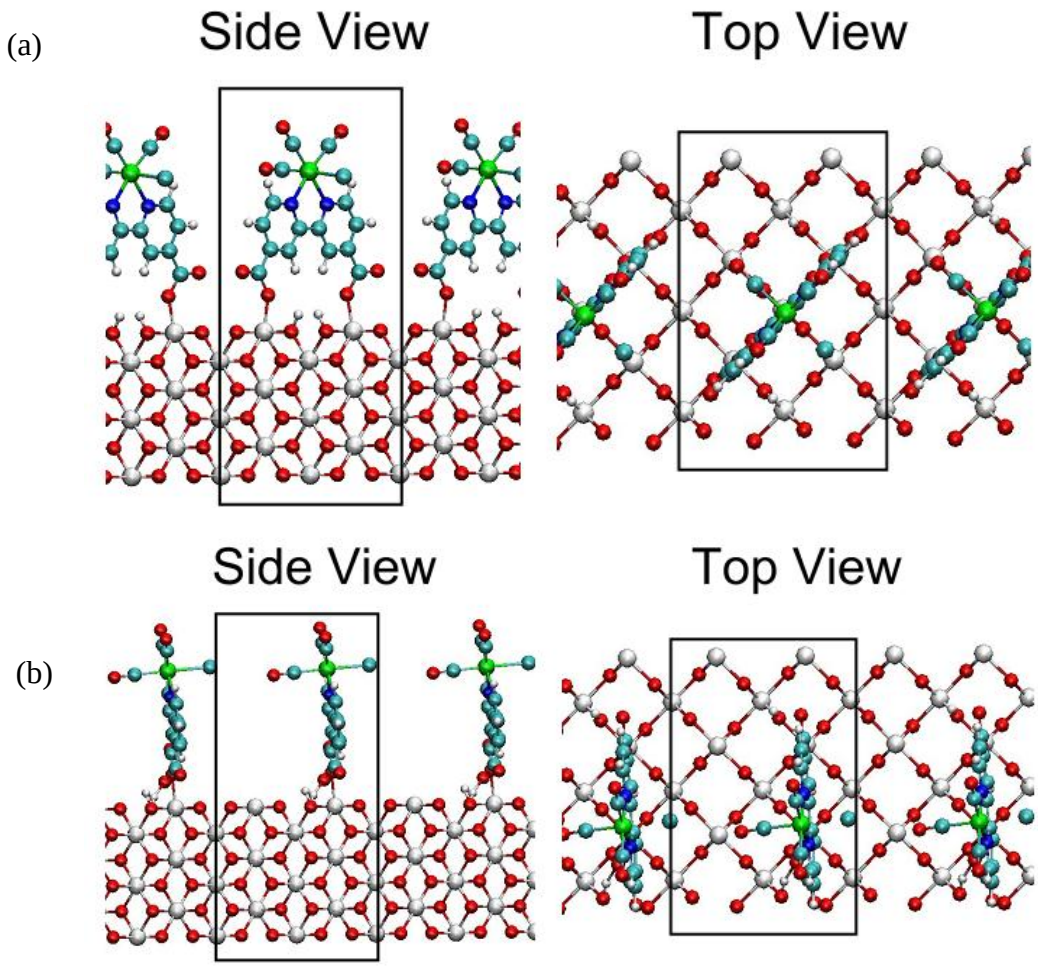

Figure 4.10. Calculated absorption geometries for ReC0A in the (a) monodentate and (b) tridentate binding motifs. The tridentate isomer (b) is predicted to be the global minimum and have an orientation angle of 11.7°, while the bidentate isomer (a) is calculated to be 4.85 kcal/mol higher in energy with an orientation angle of 0.9°. Both structures are energetically equivalent within the assumed error of the computation and it is likely that the observed SFG signal is from a combination of the two.

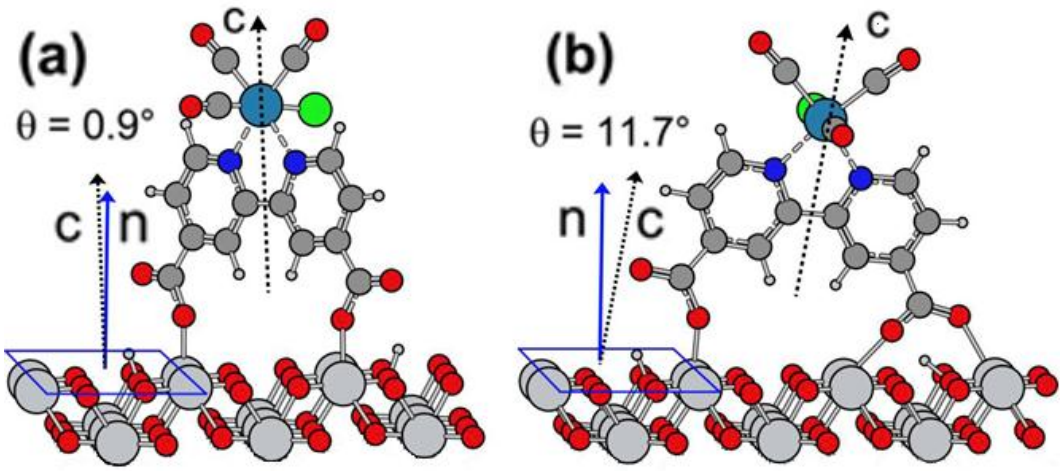

Figure 4.11. Calculated adsorption geometries for ReC0A on TiO_2 (001) in the (a) monodentate and (b) tridentate binding motifs.

Figure 4.11 illustrates the orientation angle of both predicted isomers in relation to the surface normal of TiO_2. The calculations for both isomers indicate that the a" and a'(2) modes are nearly perpendicular to the surface normal (z-axis in laboratory frame). Since TiO_2 (001) has C_4 symmetry, the molecules are assumed to be randomly orientated in the x-y plane. In this case, the system effectively becomes centrosymmetric for these two vibrational transitions, and thus the the $\chi^{(2)}_{ijk}$ elements associated with the a" and a'(2) modes vanish. As an illustrative example, let us consider a molecule where the a" mode projects exactly onto the molecular x axis. Due to the C_4 symmetry of the system, we can expect that there is another molecule where the a" mode projects exactly onto the negative x axis. Since the $\chi^{(2)}_{ijk}$ elements are an orientational average of the hyperpolarizability elements, these two molecules thus cancel each other out and the related $\chi^{(2)}_{ijk}$ elements will average to zero. Thus, in the case where the a" and a'(2) modes are nearly perpendicular to the surface normal, these modes would be expected to

have little to no VSFG activity in any polarization combination. This is another possible explanation for the absence of the a" and a'(2) modes in the VSFG spectra.

4.3. Summary

VSFG spectroscopy has been used to determine the adsorption geometry of the model electrocatalyst and molecular adsorber ReC0A on a single crystal TiO_2 (001) surface. SFG spectra of ReC0A/TiO_2 (001) revealed a single vibrational band corresponding to the totally symmetric a'(1) mode. The polarization dependence of this band indicates a molecular orientation angle θ of 0 – 22° from the surface normal. A collaboration with Batista *et al.* allowed for the comparison of these experimental results with predicted adsorption geometries from DFT calculations. They found that two calculated structures displayed orientation angles that fall within the experimentally determined range, resulting from a bidentate (θ = 0.9°) or tridentate (θ = 11.7°) binding linkage of the carboxylate groups to the TiO_2 (001) surface. The upright orientation of ReC0A on TiO_2 leaves the rhenium atom exposed for maximum reductive capacity. This detailed understanding of the interfacial structure in this model system allows for a better understanding of the mechanism of electron transfer and catalysis at the molecule/semiconductor interface, and may aid in the design of more efficient and stable catalysts.

4.4 References

(1) O'Regan, B.; Gratzel, M. *Nature* **1991**, *353*, 737.

(2) Kamat, P. V.; Meisel, D. *Current Opinion in Colloid & Interface Science* **2002**, *7*, 282.

(3) Adams, D. M.; Brus, L.; Chidsey, C. E. D.; Creager, S.; Creutz, C.; Kagan, C. R.; Kamat, P. V.; Lieberman, M.; Lindsay, S.; Marcus, R. A.; Metzger, R. M.; Michel-Beyerle, M. E.; Miller, J. R.; Newton, M. D.; Rolison, D. R.; Sankey, O.; Schanze, K. S.; Yardley, J.; Zhu, X. *Journal of Physical Chemistry B* **2003**, *107*, 6668.

(4) Gratzel, M. *MRS Bulletin* **2005**, *30*, 23.

(5) Prezhdo, O. V.; Duncan, W. R.; Prezhdo, V. V. *Accounts of Chemical Research* **2008**, *41*, 339.

(6) Marcus, R. A. *J. Chem. Phys.* **1965**, *43*, 679.

(7) Gao, Y. Q.; Georgievskii, Y.; Marcus, R. A. *J. Chem. Phys.* **2000**, *112*, 3358.

(8) Gao, Y. Q.; Marcus, R. A. *J. Chem. Phys.* **2000**, *113*, 6351.

(9) Gosavi, S.; Marcus, R. A. *J. Phys. Chem. B* **2000**, *104*, 2067.

(10) Asbury, J. B.; Hao, E.; Wang, Y.; Ghosh, H. N.; Lian, T. *J. Phys. Chem. B* **2001**, *105*, 4545.

(11) Anderson, N. A.; Ai, X.; Chen, D.; Mohler, D. L.; Lian, T. *Journal of Physical Chemistry B* **2003**, *107*, 14231.

(12) She, C.; Anderson, N. A.; Guo, J.; Liu, F.; Goh, W.; Chen, D.-T.; Mohler, D. L.; Tian, Z.-Q.; Hupp, J.; Lian, T. *J. Phys. Chem. B.* **2005**, *109*, 19345.

(13) Huang, J.; Stockwell, D.; Boulesbaa, A.; Guo, J.; Lian, T. *J. Phys. Chem. C* **2008**, *112*, 5203.

(14) Stockwell, D.; Yang, Y.; Huang, J.; Anfuso, C.; Huang, Z. Q.; Lian, T. Q. *Journal of Physical Chemistry C* **2010**, *114*, 6560.

(15) She, C. A., Neil A.; Guo, Jianchang; Liu, Fang; Goh, Wan-Hee; Chen, Dai-Tao; Mohler, Debra L.; Tian, Zhong-Qun; Hupp, Joseph T.; Lian, Tianquan. *Journal of Physical Chemistry B* **2005**, *109*, 19345.

(16) She, C.; Guo, J.; Irle, S.; Morokuma, K.; Mohler, D. L.; Zabri, H.; Odobel, F.; Youm, K.-T.; Liu, F.; Hupp, J. T.; Lian, T. *Journal of Physical Chemistry A* **2007**, *111*, 6832.

(17) Benson, E. E.; Kubiak, C. P.; Sathrum, A. J.; Smieja, J. M. *Chem Soc Rev* **2009**, *38*, 89.

(18) Hawecker, J.; Lehn, J. M.; Ziessel, R. *J Chem Soc Chem Comm* **1984**, 328.

(19) Hawecker, J.; Lehn, J. M.; Ziessel, R. *Helv Chim Acta* **1986**, *69*, 1990.

(20) Juris, A.; Campagna, S.; Bidd, I.; Lehn, J. M.; Ziessel, R. *Inorg Chem* **1988**, *27*, 4007.

(21) Yam, V. W. W.; Lau, V. C. Y.; Cheung, K. K. *Organometallics* **1995**, *14*, 2749.

(22) Hayashi, Y.; Kita, S.; Brunschwig, B. S.; Fujita, E. *Journal of the American Chemical Society* **2003**, *125*, 11976.

(23) Fujita, E.; Hayashi, Y.; Kita, S.; Brunschwig, B. S. *Carbon Dioxide Utilization for Global Sustainability* **2004**, *153*, 271.

(24) Fujita, E.; Muckerman, J. T. *Inorg Chem* **2004**, *43*, 7636.

(25) Takeda, H.; Koike, K.; Inoue, H.; Ishitani, O. *Journal of the American Chemical Society* **2008**, *130*, 2023.

(26) Smieja, J. M.; Kubiak, C. P. *Inorg Chem* **2010**, *49*, 9283.

(27) Cecchet, F.; Alebbi, M.; Bignozzi, C. A.; Paolucci, F. *Inorganica Chimica Acta* **2006**, *359*, 3871.

(28) Breckenridge, R. G.; Hosler, W. R. *Phys Rev* **1953**, *91*, 793.

(29) Kormann, C.; Bahnemann, D. W.; Hoffmann, M. R. *Journal of Physical Chemistry* **1988**, *92*, 5196.

(30) Diebold, U.; Lehman, J.; Mahmoud, T.; Kuhn, M.; Leonardelli, G.; Hebenstreit, W.; Schmid, M.; Varga, P. *Surf. Sci.* **1998**, *411*, 137.

(31) Diebold, U. *Surf. Sci. Rep.* **2003**, *48*, 53.

(32) Diebold, U.; Ruzycki, N.; Herman, G. S.; Selloni, A. *Catalysis Today* **2003**, *85*, 93.

(33) Dulub, O.; Di Valentin, C.; Selloni, A.; Diebold, U. *Surface Science* **2006**, *600*, 4407.

(34) Gong, X. Q.; Khorshidi, N.; Stierle, A.; Vonk, V.; Ellinger, C.; Dosch, H.; Cheng, H. Z.; Selloni, A.; He, Y. B.; Dulub, O.; Diebold, U. *Surface Science* **2009**, *603*, 138.

(35) Kiwiet, N. J.; Fox, M. A. *Journal Of the Electrochemical Society* **1990**, *137*, 561.

(36) Ruizlopez, M. F.; Munozpaez, A. *Journal of Physics-Condensed Matter* **1991**, *3*, 8981.

(37) Sorantin, P. I.; Scharz, K. *Inorg. Chem.* **1992**, *31*, 567.

(38) Onda, K.; Li, B.; Petek, H. *Physical Review B* **2004**, *70*.

(39) Pellnor, M.; Myllyperkio, P.; Korppi-Tommola, J.; Yartsev, A.; Sundstrom, V. *Chemical Physics Letters* **2008**, *462*, 205.

(40) Duncan, W. R.; Prezhdo, O. V. *Annu. Rev. Phys. Chem.* **2007**, *58*, 143.

(41) Gundlach, L.; Ernstorfer, R.; Willig, F. *Appl. Phys. A: Mater. Sci. Process.* **2007**, *88*, 481.

(42) Fillinger, A.; Soltz, D.; Parkinson, B. A. *Journal of the Electrochemical Society* **2002**, *149*, A1146.

(43) Lu, Y.; Jaeckel, B.; Parkinson, B. A. *Langmuir* **2006**, *22*, 4472.

(44) Lu, Y.; Spitler, M. T.; Parkinson, B. A. *Journal of Physical Chemistry B* **2006**, *110*, 25273.

(45) Lu, Y.; Spitler, M. T.; Parkinson, B. A. *Langmuir* **2007**, *23*, 11637.

(46) Lu, Y. F.; Choi, D. J.; Nelson, J.; Yang, O. B.; Parkinson, B. A. *Journal of the Electrochemical Society* **2006**, *153*, E131.

(47) Ushiroda, S.; Ruzycki, N.; Lu, Y.; Spitler, M. T.; Parkinson, B. A. *Journal of the American Chemical Society* **2005**, *127*, 5158.

(48) Zhuang, X.; Miranda, P. B.; Kim, D.; Shen, Y. R. *Physical Review B* **1999**, *59*, 12632.

(49) Lambert, A. G.; Davies, P. B.; Neivandt, D. J. *Applied Spectroscopy Reviews* **2005**, *40*, 103.

(50) Rao, Y.; Comstock, M.; Eisenthal, K. B. *Journal of Physical Chemistry B* **2006**, *110*, 1727.

(51) Asbury, J. B.; Wang, Y.; Lian, T. *Bull. Chem. Soc. Japan* **2002**, *75*, 973.

(52) Raschke, M. B.; Hayashi, M.; Lin, S. H.; Shen, Y. R. *Chemical Physics Letters* **2002**, *359*, 367.

(53) Hayashi, M.; Lin, S. H.; Raschke, M. B.; Shen, Y. R. *Journal of Physical Chemistry A* **2002**, *106*, 2271.

(54) Busson, B.; Tadjeddine, A. *Journal of Physical Chemistry C* **2008**, *112*, 11813.

(55) Wang, H. F.; Gan, W.; Lu, R.; Rao, Y.; Wu, B. H. *International Reviews in Physical Chemistry* **2005**, *24*, 191.

(56) Richmond, G. L. *Annu. Rev. Phys. Chem.* **2001**, *52*, 357.

(57) Waterland, M. R.; Howell, S. L.; Gordon, K. C. *Journal of Physical Chemistry A* **2007**, *111*, 4604.

(58) Gamelin, D. R.; George, M. W.; Glyn, P.; Grevels, F.-W.; Johnson, F. P. A.; Klotzbuecher, W.; Morrison, S. L.; Russell, G.; Schaffner, K.; Turner, J. J. *Inorg. Chem.* **1994**, *33*, 3246.

(59) Dick, B. *Chemical Physics* **1985**, *96*, 199.

(60) Gamelin, D. R.; George, M. W.; Glyn, P.; Grevels, F. W.; Johnson, F. P. A.; Klotzbucher, W.; Morrison, S. L.; Russell, G.; Schaffner, K.; Turner, J. J. *Inorg. Chem.* **1994**, *33*, 3246.

(61) Moad, A. J.; Simpson, G. J. *Journal of Physical Chemistry B* **2004**, *108*, 3548.

(62) Anfuso, C. L.; Snoeberger, R. C.; Ricks, A. M.; Liu, W. M.; Xiao, D. Q.; Batista, V. S.; Lian, T. Q. *Journal of the American Chemical Society* **2011**, *133*, 6922.

Chapter 5: Surface-Induced Ordering of a Rhenium Bipyridyl CO_2-Reduction Catalyst on Rutile TiO_2 Surfaces

5.1. Introduction

Vibrational sum frequency generation spectroscopy (VSFGS) has been recognized in recent years as a useful technique for determining average molecular conformation at interfaces.[1-4] A second-order optical technique, it is forbidden in media with inversion symmetry but allowed at interfaces where inversion symmetry is necessarily broken. VSFGS is thus surface-specific, giving it a distinct advantage over other optical techniques and making it an ideal tool for elucidating a molecular-level picture of molecule-semiconductor systems. Although it is typically used to determine the average molecular tilt angle for molecules on isotropic surfaces, it can also be used to determine the degree of anisotropy in interfacial systems. Specifically, by monitoring the molecular sum frequency response as a function of the surface azimuthal angle, the anisotropic orientation distribution can be deduced.[5-12] Such experiments have thus far primarily focused on polymer surfaces, and in particular polyimide surfaces for use in liquid crystal displays.[5-10] Typically, the polymer sample is mechanically rubbed in order to induce a preferential alignment of the polymer backbone along the rubbing direction, which VSFGS is used to characterize. However, few studies to date have focused on molecular ordering that is induced by the underlying substrate rather than by a mechanical or chemical force. Recently, Shen *et al*. investigated the protonated R-plane $(1\,\bar{1}\,02)$ sapphire surface and found that VSFGS spectra of the OH groups exhibited the C_{1v} symmetry of the sapphire surface.[12] This was followed by a similar study on the

ethanol vapor/$(1\bar{1}02)$ sapphire and ethanol liquid/$(1\bar{1}02)$ sapphire interfaces, which also reported VSFGS spectra with the C_{1v} symmetry of the sapphire surface.[11] These studies indicate the potential to control molecular ordering at an interface through careful selection of a substrate, which can be subsequently characterized using VSFGS techniques.

Such studies have very interesting implications for photocatalytic and electrocatalytic systems, whose performance is often highly dependent on the microscopic ordering of catalytic molecules on a scaffolding support system.[13-16] Of particular interest is the molecule-semiconductor electrode interface, which is relevant in many types of catalytic systems.[17-21] Since the average molecular orientation in these systems can significantly affect their catalytic performance, the ability to control the molecular ordering through careful selection of the underlying substrate may prove advantageous. An investigation of catalytic molecules on surfaces with identical chemical structures but different symmetries may elucidate how the average molecular alignment depends on the surface ordering. These studies may aid in the development of beneficially ordered photocatalytic and electrocatalytic systems and therefore are of great practical interest.

$Re(CO)_3Cl(dcbpy)$ (dcbpy = 4,4′-dicarboxy-2,2′-bipyridine) (ReC0A) and several derivatives have been explored in recent years for catalytic reduction of CO_2 to CO.[22-30] Binding of a rhenium bipyridyl complex to TiO_2 electrodes has also been shown to increase catalytic reductive ability.[20] Characterizing the ReC0A/TiO_2 interface is thus important to fully understanding this important catalytic system. Chapter 4 details an investigation of the orientation of ReC0A on single crystalline TiO_2 (001) using a

combination of vibrational sum frequency generation spectroscopy (VSFGS) and Density Functional Theory (DFT) calculations, wherein the results show that the complex exhibits an isotropic distribution on the surface with an average molecular tilt angle of 0 – 22°.[31] In that study, the (001) surface was chosen for its high level of symmetry (C_4), which simplified the VSFGS analysis. In this Chapter, we have extended upon the previous work by investigating the average molecular orientation of ReC0A on the anisotropic (110) surface (C_{2v}) in order to determine the extent of molecular ordering induced by the surface symmetry. We show that ReC0A has a well-defined anisotropic arrangement following the structure of the TiO_2 (110) surface, in contrast to an isotropic distribution on the more symmetric TiO_2 (001) surface.

5.2 Results and Discussion

5.2.1. VSFGS Spectra of ReC0A on TiO_2 (001) and (110)

Figure 5.1 shows the VSFGS spectra of ReC0A on TiO_2 (001) and (110) in the carbonyl stretching region in the PPP polarization combination (indicating the polarization of the sum frequency, visible, and infrared fields, respectively) when the azimuthal angle $\Psi = 90°$. Also shown is an illustration of the surface geometry that defines the angle Ψ. Both spectra exhibit a SF-active band at 2040 cm^{-1} that can be assigned to the totally symmetric a' carbonyl stretch[31] with no other spectral features in the region investigated. The ReC0A/TiO_2 (110) system exhibits a significantly larger (approximately a factor of three) resonant response for this particular azimuthal angle.

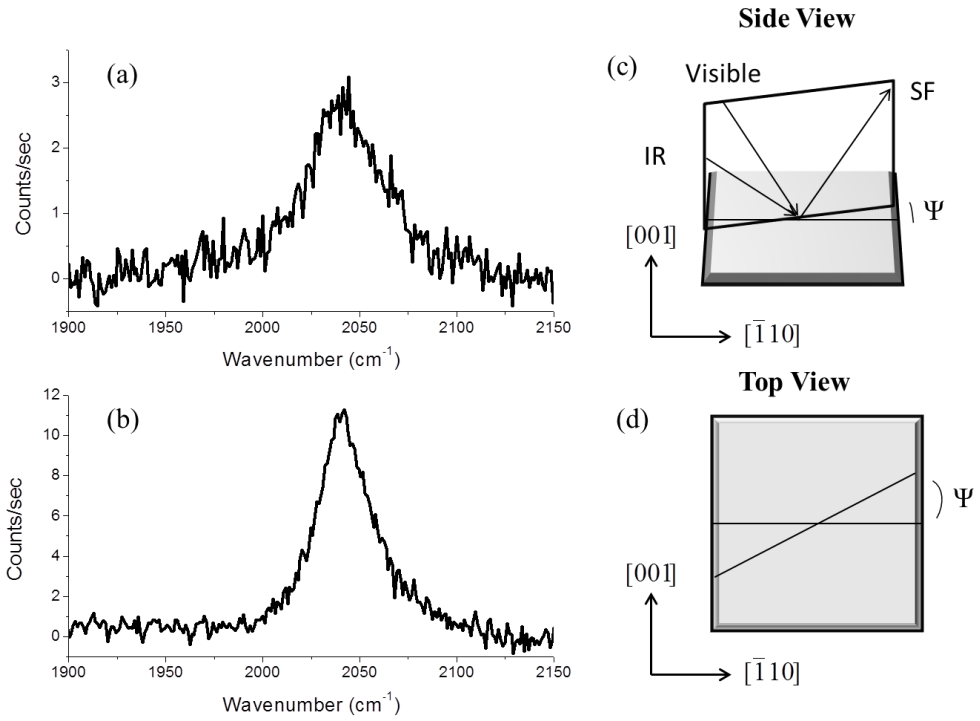

Figure 5.1. VSFGS spectra of ReC0A on (a) TiO_2 (001) and (b) TiO_2 (110) in the carbonyl stretching region in the PPP polarization combination when the azimuthal angle $\Psi = 90°$. (c) and (d) Geometry of the beams with respect to the sample surface illustrating the azimuthal angle Ψ from the (c) side and (d) top view.

Although both the (001) and (110) TiO_2 substrates do exhibit some nonresonant SF signal (results not shown), this was suppressed through delay of the visible pulse with respect to the IR pulse according to published procedures.[32] In this system, the visible pulse was delayed by ~0.5 ps for both samples. Although this effectively suppresses the nonresonant contribution, it simultaneously results in a decrease in the resonant VSFGS signal by a factor which may not be identical for both systems. Therefore, although the difference in VSFGS magnitude at 2040 cm^{-1} is used to make some qualitative statements

about the two ReC0A/TiO_2 systems, it was not used to deduce any quantitative differences.

As detailed in Chapter 2, in general the VSFGS response is given by:[1,2,4]

$$I(\omega_{SF}) \propto \left|\chi_{NR}^{(2)} e^{i\phi} + \chi_{R}^{(2)}\right|^2 I_{vis}(\omega_{vis}) I_{IR}(\omega_{IR})$$
$$\propto \left|\chi_{NR}^{(2)} e^{i\phi} + \sum_q \frac{A_q}{\omega_{IR} - \omega_q + i\Gamma_q}\right|^2 I_{vis}(\omega_{vis}) I_{IR}(\omega_{IR}) \qquad (5.1)$$

where $I_{vis}(\omega_{vis})$ and $I_{IR}(\omega_{IR})$ are the intensities of the two incident electric fields, $\chi_R^{(2)}$ and $\chi_{NR}^{(2)}$ are the resonant and nonresonant nonlinear susceptibility tensors, respectively, and $e^{i\phi}$ denotes the phase difference between them. The resonant nonlinear susceptibility can be approximated as a sum of Lorentzian functions, where A_q is the amplitude of a resonant SF-active vibration, ω_{IR} is the frequency of the incident tunable infrared beam, and ω_q and Γ_q are the frequency and damping constant of the q^{th} vibrational mode, respectively. The sum is over all vibrational modes of the interfacial molecules. When fitting a single vibrational mode, however, only a Lorenztian function needs to be utilized and the sum term can be dropped.

Equation 5.1 can be used to fit the experimental VSFGS spectra for ReC0A on TiO_2 (001) and (110) in order to quantify the amplitudes A_q and linewidths (damping constant) Γ_q of the resonant totally symmetric a' vibrational mode, as well as the magnitude and phase of the nonresonant response $\chi_{NR}^{(2)}$ from the TiO_2 single crystal substrates. Figure 5.2 shows the results of this fitting, where the parameters used for each surface are listed in Table 5.1. The fittings indicate that the TiO_2 nonresonant response is sufficiently suppressed for both surfaces, as can be seen from the small $\chi_{NR}^{(2)}$ values for both samples. Additionally, the larger amplitude and narrower linewidth for the

ReC0A/TiO_2 (110) system may indicate a more highly ordered system compared to ReC0A/TiO_2 (001), since this would be expected to yield higher VSFGS spectral intensities and a smaller degree of inhomogeneous broadening due to multiple adsorption geometries.

Although the differences in the VSFGS spectra at a particular azimuthal angle are useful for making qualitative observations, a more rigorous approach was needed in order to make quantitative statements about these two electrocatalyst-semiconductor systems. Specifically, in order to deduce the degree of in-plane molecular ordering for the ReC0A/TiO_2 (110) system, the VSFGS signal as a function of azimuthal angle was investigated. Although an isotropic distribution for ReC0A/TiO_2 (001) was previously noted, its azimuthal angle dependence was also monitored in order to provide a comparison for the ReC0A/TiO_2 (110) results.

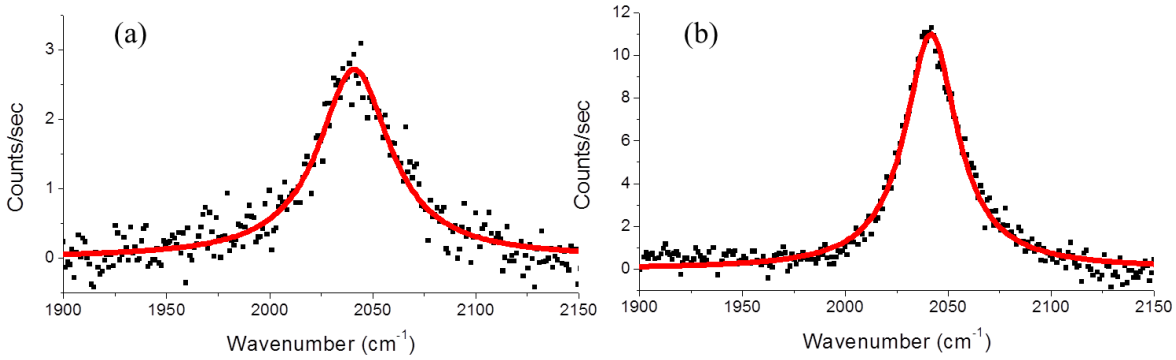

Figure 5.2. Fitted VSFGS spectra of ReC0A on (a) TiO_2 (001) and (b) TiO_2 (110) according to Equation 5.1. Fitting parameters are listed in Table 5.1.

Table 5.1. Fitting parameters for ReC0A/TiO_2 (001) and (110) VSFGS spectra.

	$\chi_{NR}^{(2)}$	φ (rad)	A_q	ω_q (cm^{-1})	Γ_q (cm^{-1})
ReC0A/TiO_2 (001)	0.0045	0.0006	34.854	2041.0	21.12
ReC0A/TiO_2 (110)	0.0167	0.0051	51.222	2041.5	15.45

5.2.2. Azimuthal Angular Dependence of the VSFGS Spectra

Previously, the ReC0A/TiO_2 system was studied with VSFGS and determined to have an isotropic distribution on the surface with an average molecular tilt angle of 0 – 22°.[31] Although the C_4 symmetry of the (001) surface indicated that an isotropic distribution should occur, it was unclear if the surface mediated the molecular ordering or if the molecules themselves preferred this distribution regardless of surface symmetry due to packing effects. Therefore, the TiO_2 (110) surface, which has an effective C_{2v} symmetry, provides an interesting comparison to determine the extent of surface-mediated ordering in ReC0A/TiO_2 systems. In order to determine the degree of anisotropy in these systems, VSFG spectra were obtained as a function of azimuthal angle. Figure 5.3 shows the integrated spectral intensities of the symmetric CO stretch as a function of azimuthal angle for both the ReC0A/TiO_2 (001) and (110) systems. In agreement with our previous work, ReC0A/TiO_2 (001) shows no azimuthal dependence, as evidenced by its circular polar plot. ReC0A/TiO_2 (110), however, shows a clear preferential alignment of the ReC0A molecules along the [001] direction of the TiO_2. The similar signal size at Ψ = 90° and 180° indicates that the molecules do not exhibit a

preferred forward or backward tilt along the [001] direction, but rather tilt equally in either direction. These results show that the structure of the ReC0A monolayer indeed reflects the effective C_{2v} symmetry of the TiO_2 (110) surface. This also indicates that the isotropic distribution observed for the ReC0A/TiO_2 (001) is most likely a direct result of the underlying (001) substrate symmetry (C_4). The ReC0A/TiO_2 (110) system also exhibited larger VSFGS signals at all azimuthal angles compared to ReC0A/TiO_2 (001), which supports the conclusion that there is a higher degree of molecular ordering for ReC0A on TiO_2 (110).

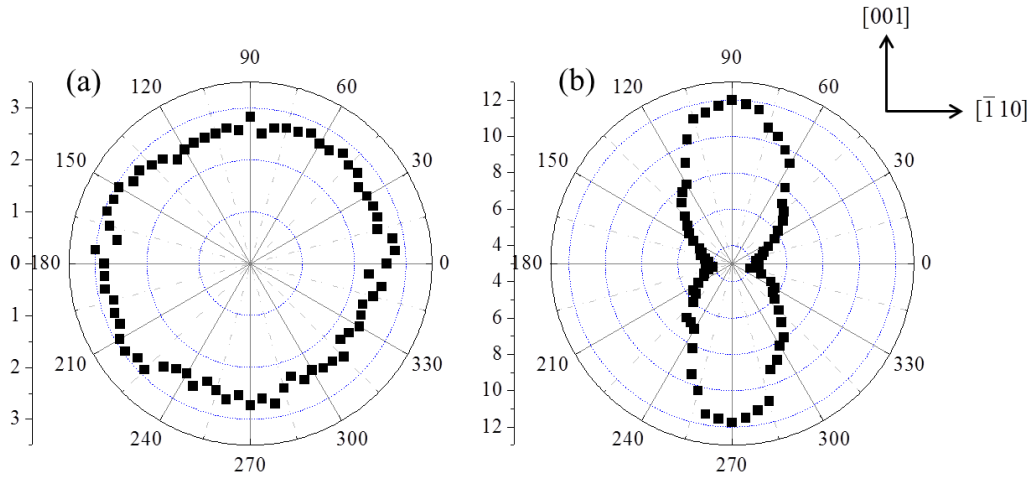

Figure 5.3. Polar plot of the experimentally measured azimuthal angle Ψ dependence of the VSFGS intensity for the totally symmetric a' mode of ReC0A on (a) TiO_2 (001) and (b) TiO_2 (110).

5.2.3. Orientation Analysis Based on Azimuthal Angular Dependence of the VSFGS Spectra

5.2.3.1. Theoretical Considerations

In order to quantify the molecular tilt angle in the ReC0A/TiO_2 (110) system, an analysis of the azimuthal dependence of the VSFGS spectra was performed. Assuming that the nonresonant background has been completely suppressed, we can see from Equation 5.1 that the VSFGS intensity is directly proportional to the square of the resonant nonlinear susceptibility $\chi_R^{(2)}$. Although $\chi_R^{(2}$ is a third rank tensor with 27 $\chi_{ijk}^{(2)}$ elements, only a few of these are nonvanishing due to symmetry properties of the interface.[31] In the case of a surface with C_{2v} symmetry (such as TiO_2 (110)), only 7 independent nonzero components remain: χ_{zzz}, χ_{xxz}, χ_{yyz}, χ_{xzx}, χ_{yzy}, χ_{zxx}, and χ_{zyy}. For a surface with C_4 symmetry (such as TiO_2 (001)), the situation is further simplified and only 4 independent nonzero components remain: χ_{zzz}, $\chi_{xxz} = \chi_{yyz}$, $\chi_{xzx} = \chi_{yzy}$, and χ_{zxx}, $= \chi_{zyy}$. These can be probed using the PPP polarization combination as a function of the azimuthal angle Ψ according to:

$$\begin{aligned}\chi^{(2)}_{eff,PPP}(\Psi) = &-L_{xx}(\omega_{SF})L_{xx}(\omega_{vis})L_{zz}(\omega_{IR})\cos\alpha_{SF}\cos\alpha_{vis}\sin\alpha_{IR}\chi_{xxz}(\theta,\psi,\phi+\Psi)\\ &- L_{xx}(\omega_{SF})L_{zz}(\omega_{vis})L_{xx}(\omega_{IR})\cos\alpha_{SF}\sin\alpha_{vis}\cos\alpha_{IR}\chi_{xzx}(\theta,\psi,\phi+\Psi)\\ &+ L_{zz}(\omega_{SF})L_{xx}(\omega_{vis})L_{xx}(\omega_{IR})\sin\alpha_{SF}\cos\alpha_{vis}\cos\alpha_{IR}\chi_{zxx}(\theta,\psi,\phi+\Psi)\\ &+ L_{zz}(\omega_{SF})L_{zz}(\omega_{vis})L_{zz}(\omega_{IR})\sin\alpha_{SF}\sin\alpha_{vis}\sin\alpha_{IR\,2}\chi_{zzz}(\theta,\psi,\phi+\Psi)\end{aligned}$$

(5.2)

where α is the incident angle and L_{ii} is the Fresnel factor for the denoted optical field. For a surface with C_{2v} symmetry, $\chi_{xxz}(\theta, \psi, \phi) = \chi_{yyz}(\theta, \psi, \phi + \pi/2)$; therefore, all seven nonzero $\chi_{ijk}^{(2)}$ elements can be measured using Equation 5.2 for both systems.

The macroscopic $\chi_{ijk}^{(2)}$ terms are related to microscopic second order hyperpolarizability elements $\beta_{\alpha\beta\gamma}$ for a given molecular system. The individual tensor elements are given by:

$$\chi_{ijk}^{(2)}(\theta,\psi,\phi) = N_s \sum_{\alpha\beta\gamma=abc} \left\langle R_{i\alpha} R_{j\beta} R_{k\gamma} \right\rangle \beta_{\alpha\beta\gamma}^{(2)} \qquad (3)$$

where N_s is the molecule number density and the operator $\langle\ \rangle$ denotes an orientational ensemble average over each Euler rotation transformation matrix element $R_{\lambda\lambda'}$ from the molecular coordinate $\lambda'(a,b,c)$ to the laboratory coordinate $\lambda'(x,y,z)$ through the Euler angles (θ,ψ,ϕ). If these $\beta_{\alpha\beta\gamma}$ elements are known, after the appropriate transformation according to Equation 5.2, it is possible to model the azimuthal dependence of the molecular VSFGS spectra according to Equation 5.3. As detailed in Chapter 4, assuming the system is near electronic resonance, the two contributing hyperpolarizability elements for the totally symmetric a' stretch of ReC0A are β_{ccc} and β_{ccb}, though the latter goes to zero due to symmetry constraints. We were thus able to model the azimuthal dependence of the VSFGS spectra in order to extract the average molecular tilt angle θ and the in-plane rotation angle ϕ.

5.2.3.2. Fitted Azimuthal Dependence for ReC0A on TiO_2 (001) and (110)

The calculated azimuthal orientation distribution function $|\chi_{PPP}(\Psi)|^2$ is compared with the experimental results for the a' mode of ReC0A on TiO_2 (001) and (110) in Figure 5.4. For ReC0A on TiO_2 (001), $\chi_{xxz} = \chi_{yyz}$, so that $|\chi_{PPP}(\Psi)|^2$ effectively becomes a constant. The fit in this case simply indicates the level of isotropy in the ReC0A/TiO_2 (001) system. The good match between the experimental and calculated results validates

our assumption that the ReC0A/TiO_2 (001) system does indeed have an isotropic distribution of ReC0A molecules on the surface.

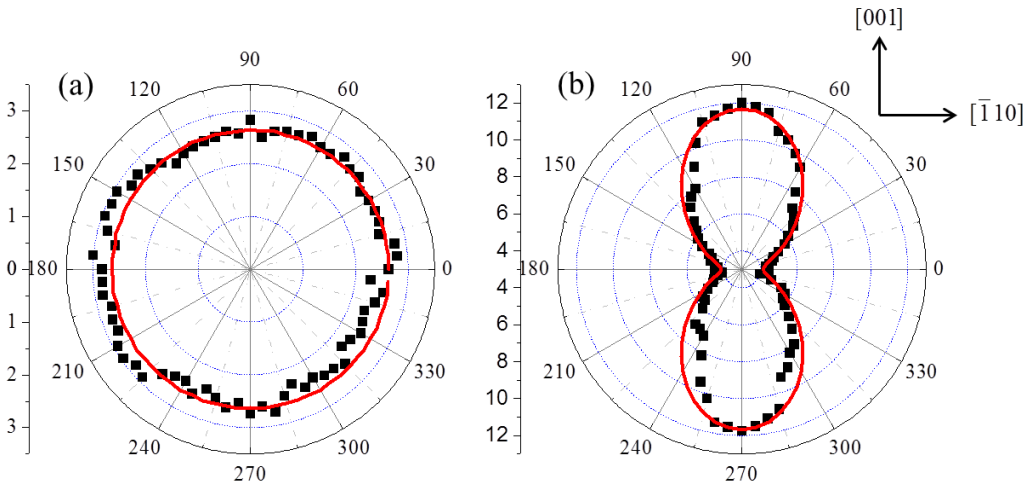

Figure 5.4. Experimentally measured (black squares) and calculated (red line) azimuthal angle Ψ dependence of the VSFGS intensity for the totally symmetric a' mode of ReC0A on (a) TiO_2 (001) and (b) TiO_2 (110). The VSFGS dependence is fit to a constant for TiO_2 (001) in order to illustrate the isotropic nature of the distribution. For ReC0A on TiO_2 (110), the VSFGS intensity is fit to Equation 5.2, where $\theta = 28°$ and $\phi = 0°$.

For ReC0A on TiO_2 (110), the calculated azimuthal orientation distribution function can be used to deduce quantitative information on the molecular ordering in this system. Assuming a δ-function distribution for both the average molecular tilt angle θ and the in-plane rotation angle ϕ, the fitting produces an average molecular tilt angle of 28° and an in-plane rotation angle of 0°. Thus we can conclude that ReC0A aligns preferentially along the [001] axis of the TiO_2 (110) surface with an average molecular

tilt angle of 28°, and the molecular alignment is clearly mediated by the TiO_2 (110) C_{2v} surface symmetry.

It should be noted that while the orientation angle was calculated using hyperpolarizability elements based on the near-resonant model outlined in Chapter 4, these results are also consistent with a model where the Raman transition moment is completely off-resonant. In this case, although we may see a change in the calculated molecular tilt angle, the results nevertheless indicate that when ReC0A is on TiO_2 (110), the molecules exhibit a clear preferential alignment along the [001] direction and mimic the substrate C_{2v} surface symmetry. Furthermore, the appreciable VSFGS signal seen for all azimuthal angles in the PPP polarization combination indicates that the a'(1) mode must maintain a significant projection on the z-axis. This is because with a significant tilt angle θ, the χ_{xxz}, χ_{xzx}, and χ_{zxx} terms of Equation 5.2 will dominate. In this case, when the incident beams are perpendicular to aligned molecules, these terms would become negligible and the VSFGS signal would go to zero. If the molecule maintains a substantial projection on the z-axis, however, the χ_{zzz} term will always contribute and thus VSFGS signal will be produced for all azimuthal angles, as seen in our results.

5.3. Summary

VSFGS has been used to deduce the degree of surface-induced ordering for a rhenium bipyridyl CO_2 reduction catalyst (ReC0A) on two single crystalline TiO_2 surfaces with different surface symmetries. We show that ReC0A has a well-defined anisotropic arrangement following the structure of the TiO_2 (110) surface, in contrast to an isotropic distribution on the more symmetric TiO_2 (001) surface. Specifically, Chapter

4 details our investigation of ReC0A on TiO_2 (001) (C_4 surface symmetry). Results indicate an isotropic distribution of the ReC0A molecules on the surface with an average in-plane tilt angle of 0 – 22°. In this Chapter, this work was extended to include ReC0A on TiO_2 (110), which exhibits C_{2v} surface symmetry. A clear preferential alignment of the ReC0A molecules along the [001] direction was observed, with an average molecular tilt angle of 28° and an in-plane rotation angle of 0°. These results show that the structure of the ReC0A monolayer indeed reflects the effective C_{2v} symmetry of the TiO_2 (110) surface. This further indicates that the isotropic distribution observed for the ReC0A/TiO_2 (001) is most likely a direct result of the underlying (001) substrate symmetry (C_4).

This study demonstrates the ability to prepare an electrocatalyst-semiconductor system with a preferred in-plane average molecular arrangement based on the underlying semiconductor surface symmetry. Since the average molecular orientation in these systems can significantly affect their catalytic performance, the ability to control the molecular ordering through careful selection of the underlying substrate may prove very useful. For example, sophisticated nanolithography techniques are now used to generate surfaces with specific and complex surface structure and symmetry. This study demonstrates that this class of electrocatalysts will bind preferentially to such surfaces, so that ordered catalytic arrays may be fabricated.

5.4 References

(1) Zhuang, X.; Miranda, P. B.; Kim, D.; Shen, Y. R. *Physical Review B* **1999**, *59*, 12632.

(2) Lambert, A. G.; Davies, P. B.; Neivandt, D. J. *Applied Spectroscopy Reviews* **2005**, *40*, 103.

(3) Wang, H. F.; Gan, W.; Lu, R.; Rao, Y.; Wu, B. H. *International Reviews in Physical Chemistry* **2005**, *24*, 191.

(4) Rao, Y.; Comstock, M.; Eisenthal, K. B. *Journal of Physical Chemistry B* **2006**, *110*, 1727.

(5) Ge, J. J.; Li, C. Y.; Xue, G.; Mann, I. K.; Zhang, D.; Wang, S. Y.; Harris, F. W.; Cheng, S. Z. D.; Hong, S. C.; Zhuang, X. W.; Shen, Y. R. *Journal of the American Chemical Society* **2001**, *123*, 5768.

(6) Hong, S. C.; Oh-e, M.; Zhuang, X. W.; Shen, Y. R.; Ge, J. J.; Harris, F. W.; Cheng, S. Z. D. *Phys Rev E* **2001**, *63*.

(7) Kim, D.; Oh-e, M.; Shen, Y. R. *Macromolecules* **2001**, *34*, 9125.

(8) Jayathilake, H. D.; Zhu, M. H.; Rosenblatt, C.; Bordenyuk, A. N.; Weeraman, C.; Benderskii, A. V. *Journal of Chemical Physics* **2006**, *125*.

(9) Lu, X. L.; Spanninga, S. A.; Kristalyn, C. B.; Chen, Z. *Langmuir* **2010**, *26*, 14231.

(10) Oh-e, M.; Kim, D.; Shen, Y. R. *Journal of Chemical Physics* **2001**, *115*, 5582.

(11) Sung, J.; Waychunas, G. A.; Shen, Y. R. *J Phys Chem Lett* **2011**, *2*, 1831.

(12) Sung, J. H.; Zhang, L. N.; Tian, C. S.; Waychunas, G. A.; Shen, Y. R. *Journal of the American Chemical Society* **2011**, *133*, 3846.

(13) Underwood, A. J. V. *Industrial and Engineering Chemistry* **1940**, *32*, 449.

(14) Balazs, G. B.; Anson, F. C. *Journal of Electroanalytical Chemistry* **1993**, *361*, 149.

(15) Raebiger, J. W.; Turner, J. W.; Noll, B. C.; Curtis, C. J.; Miedaner, A.; Cox, B.; DuBois, D. L. *Organometallics* **2006**, *25*, 3345.

(16) Benson, E. E.; Kubiak, C. P.; Sathrum, A. J.; Smieja, J. M. *Chemical Society Reviews* **2009**, *38*, 89.

(17) Christensen, P.; Hamnett, A.; Muir, A. V. G.; Timney, J. A.; Higgins, S. *Journal of the Chemical Society-Faraday Transactions* **1994**, *90*, 459.

(18) Yoshida, T.; Tsutsumida, K.; Teratani, S.; Yasufuku, K.; Kaneko, M. *J Chem Soc Chem Comm* **1993**, 631.

(19) Otoole, T. R.; Margerum, L. D.; Westmoreland, T. D.; Vining, W. J.; Murray, R. W.; Meyer, T. J. *J Chem Soc Chem Comm* **1985**, 1416.

(20) Cecchet, F.; Alebbi, M.; Bignozzi, C. A.; Paolucci, F. *Inorganica Chimica Acta* **2006**, *359*, 3871.

(21) Cheung, K. C.; Guo, P.; So, M. H.; Lee, L. Y. S.; Ho, K. P.; Wong, W. L.; Lee, K. H.; Wong, W. T.; Zhou, Z. Y.; Wong, K. Y. *J Organomet Chem* **2009**, *694*, 2842.

(22) Hawecker, J.; Lehn, J. M.; Ziessel, R. *J Chem Soc Chem Comm* **1984**, 328.

(23) Hawecker, J.; Lehn, J. M.; Ziessel, R. *Helv Chim Acta* **1986**, *69*, 1990.

(24) Yam, V. W. W.; Lau, V. C. Y.; Cheung, K. K. *Organometallics* **1995**, *14*, 2749.

(25) Hayashi, Y.; Kita, S.; Brunschwig, B. S.; Fujita, E. *Journal of the American Chemical Society* **2003**, *125*, 11976.

(26) Fujita, E. H., Y.; Kita, S.; Brunschwig, B. S. In *7th International Conference on Carbon Dioxide Utilization*; Sang-Eon Park, J.-S. C., Kyu-Wan Lee, Ed.; Elsevier: Seoul, Korea, 2004.

(27) Fujita, E.; Muckerman, J. T. *Inorg Chem* **2004**, *43*, 7636.

(28) Takeda, H.; Koike, K.; Inoue, H.; Ishitani, O. *Journal of the American Chemical Society* **2008**, *130*, 2023.

(29) Smieja, J. M.; Kubiak, C. P. *Inorganic Chemistry* **2010**, *49*, 9283.

(30) Juris, A.; Campagna, S.; Bidd, I.; Lehn, J. M.; Ziessel, R. *Inorganic Chemistry* **1988**, *27*, 4007.

(31) Anfuso, C. L.; Snoeberger, R. C.; Ricks, A. M.; Liu, W. M.; Xiao, D. Q.; Batista, V. S.; Lian, T. Q. *Journal of the American Chemical Society* **2011**, *133*, 6922.

(32) Lagutchev, A.; Hambir, S. A.; Dlott, D. D. *Journal of Physical Chemistry C* **2007**, *111*, 13645.

(33) Shen, Y. R. *The principles of nonlinear optics*; J. Wiley: New York, 1984.

Chapter 6: Orientation of a Series of Rhenium Bipyridyl CO_2-Reduction Catalysts on Single Crystalline TiO_2 (001) using Phase-Sensitive Vibrational Sum Frequency Generation Spectroscopy (PS-VSFGS)

6.1. Introduction

Research on interfacial and surface-dependent processes has driven the development of experimental techniques capable of obtaining a detailed structural and dynamical picture of these systems. Of particular interest is the molecule-semiconductor interface, which is relevant in many types of catalytic systems, photocatalytic and photovoltaic materials, and molecular electronics.[1-5] The efficiency and specificity of many of these processes are dependent on molecular orientation on the semiconductor surface. Determination of molecular orientation at interfaces has proven to be experimentally challenging; however, vibrational sum frequency generation spectroscopy (VSFGS) has been recognized in recent years as a useful technique for determining average molecular conformation at interfaces.[6-9] A second-order optical technique, it is forbidden in media with inversion symmetry but allowed at interfaces where inversion symmetry is necessarily broken. This gives SFG the distinct advantage over other optical techniques of surface specificity, and makes it an ideal tool for elucidating a molecular-level picture of molecule-semiconductor systems.

Molecule-semiconductor interactions are often particularly important in photo- and electrocatalytic systems. Several rhenium complexes with modified bipyridine ligands have been developed and explored in recent years for their ability to catalytically

reduce CO_2 to CO.[10-18] Interestingly, a rhenium bipyridyl complex was recently shown to have increased catalytic reductive ability when adsorbed to TiO_2 electrodes.[19] Characterizing the ReC0A/TiO_2 interface is thus important to fully understanding this important catalytic system.

Chapters 4 and 5 detail our investigation of the orientation of a rhenium bypyridyl complex (abbreviated ReC0A) on single crystalline TiO_2 (001) and (110), respectively, using a combination of vibrational sum frequency generation spectroscopy (VSFGS) and Density Functional Theory (DFT) calculations. ReC0A on TiO_2 (001) was found to have an isotropic surface distribution with an average molecular tilt angle of 0 – 22°.[20] The ReC0A/TiO_2 (110) system, on the other hand, was found to have an anisotropic surface distribution that followed the C_{2v} symmetry of the (110) surface, producing a preferential ReC0A alignment along the [001] axis with an average molecular tilt angle of 28°. The similar molecular tilt angles but very different azimuthal distributions indicate that in these systems the surface mediates the in-plane molecular ordering but has a less substantial effect on the out-of-plane molecular orientation. Just as there is a vested interest in the ability to produce preferentially *aligned* catalytic systems based on careful selection of the underlying substrate, the ability to predict and produce preferentially *tilted* catalytic systems may also prove beneficial for the improvement and development of catalytic devices. One potential method of doing this is through the extension of the molecular linkers which binds the ReC0A molecule to the TiO_2 surface.

Based on our previous results, we wished to extend these studies on molecular orientation to include other molecules in the ReC0A family. In particular, we chose to focus on a series of five rhenium bipyridyl complexes, $Re(L_nA)(CO)_3Cl$ [LnA=2,2'-

bipyridine-4,4'-$(CH_2)_n$-COOH, n=0-4] (abbreviated as ReCnA); their structures are shown in Figure 6.1. These molecules are known to adsorb to semiconductor surfaces through their carboxylate anchoring groups, which are attached to the bipyridine ligands through methyl spacers of varying lengths (n-CH_2 units).[21-23] These complexes have been shown to inject electrons into the semiconductor at different rates depending on the value of n.[22,23] However, it is currently unclear if this rate dependence is due to a change in the average orientation of these complexes on the semiconductor surface as n is increased. As the molecule increases in length, it may pack tightly together in a nearly upright configuration as alkanethiols are prone to do,[24] or begin to tilt closer to the TiO_2 surface as the linkers lose rigidity. A change in molecular conformation could be expected to affect the overall catalytic efficiency of such molecules, since the catalytic Re center must be free to coordinate a CO_2 molecule. Therefore a study of the average molecular orientation of the ReCnA family may elucidate the effect orientation plays on electron transfer and catalytic ability. It may also indicate our ability to preferentially control the average molecular tilt angle through careful selection of the length of the molecular linker for a given system.

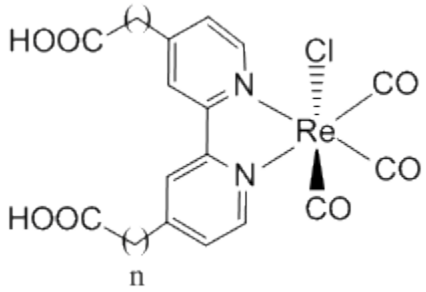

Figure 6.1. Schematic structure of ReCnA, where n refers to the number of CH_2 units between the carboxylate and bipyridine groups.

In this Chapter, we have investigated the average molecular orientation of the ReCnA series (n = 0 – 4) on a rutile TiO_2 (001) single crystal using a combination of phase-sensitive vibrational sum frequency generation spectroscopy (PS-VSFGS) and Density Functional Theory (DFT) calculations. The reasons for employing PS-VSFGS and its theoretical description are explained in the following sections. The (001) surface was chosen for its C_4 symmetry, which is known to yield an isotropic surface distribution for ReC0A and simplifies the analysis compared to less symmetric TiO_2 cuts.[20]

6.2. Results and Discussion

6.2.1. VSFGS Spectra of ReC0A and ReC1A on TiO_2 (001)

Figure 6.2 shows the VSFGS spectra of ReC0A and ReC1A on TiO_2 (001) in the PPP polarization combination. The FTIR spectra of each on nanocrystalline TiO_2 are also shown for comparison. The spectrum for ReC0A/TiO_2 (001) was reported previously and was thus examined in this experiment for comparison and reproducibility purposes. Its FTIR spectrum show three carbonyl bands: an in-phase symmetric a'(1) stretch v_3 at 2040 cm^{-1} and an unresolved band consisting of an anti-symmetric a" stretch v_2 (centered at ~1939 cm^{-1}) and out-of-phase symmetric a'(2) stretch v_1 (centered at ~1910 cm^{-1}); these stretches are illustrated in Figure 6.3. The VSFGS spectrum of ReC0A/TiO_2 (001) exhibits a SF-active band at 2040 cm^{-1} that can be assigned to the totally symmetric a' carbonyl stretch with no other spectral features in the region investigated. Previous analysis of the polarization-dependent VSFGS study of ReC0A on TiO_2 (001) indicates that the molecule exhibits an average molecular tilt angle of 0 – 22°.[20]

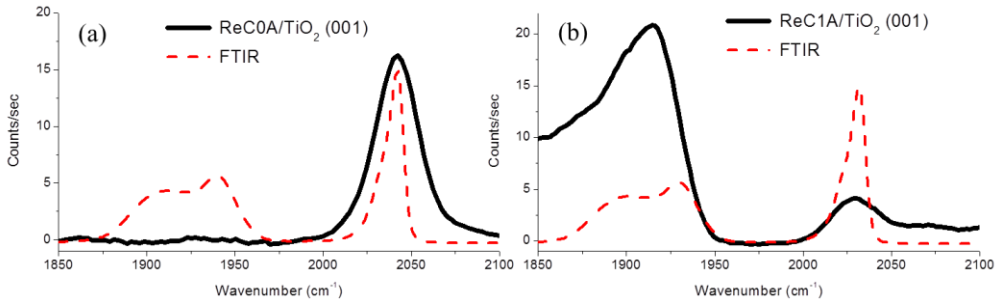

Figure 6.2. Normalized and averaged VSFGS spectra for (a) ReC0A and (b) ReC1A on TiO_2 (001) in the PPP polarization combination. Also shown for comparison is the FTIR spectrum of (a) ReC0A and (b) ReC1A on nanoporous TiO_2 (red dashed line).

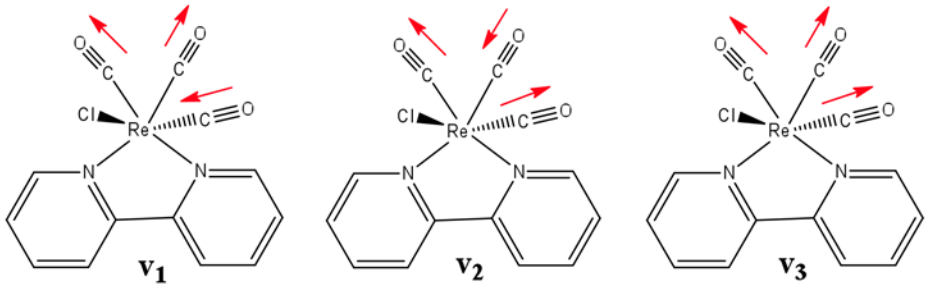

Figure 6.3. The three carbonyl stretches of ReCnA probed here: an out-of-phase symmetric a'(2) stretch (ν_1), an anti-symmetric a" stretch (ν_2), and an in-phase symmetric a'(1) stretch (ν_3).

Unlike the ReC0A/TiO_2 (001) system, the VSFGS spectrum of ReC1A/TiO_2 (001) displays two sharp features at 20430 and 1925 cm^{-1} and a broad feature that extends from 1925 cm^{-1} to the red beyond the investigated spectral region. We assign the 2030 cm^{-1} band to the totally symmetric a'(1) carbonyl stretch. The redshift of this mode for

ReCnA compared to ReC0A has been noted previously and can be attributed to increased electron density on the Re(I) metal center due to the insertion of the CH_2 spacers.[25] These spacers reduce the amount of electron delocalization into the carboxylate groups on the bipyridine ligand, thereby decreasing its electron withdrawing capabilities and increasing the electron density on the metal center. This feature is approximately four times smaller than the corresponding feature in the ReC0A/TiO_2 (001) spectrum.

We attribute the broad component below 1925 cm^{-1} to a combination of the anti-symmetric a" stretch (v_2) and/or out-of-phase symmetric a'(2) stretch (v_1) with the nonresonant response from the TiO_2 (001) single crystal, where the nonresonant response causes the resonant band(s) to tail off to the red. A similar effect can be seen for the symmetric a' stretch at 2030 cm^{-1}, where the nonresonant signal leads to an above-baseline VSFGS signal far to the blue of the resonant band. We speculate that the increased nonresonant contribution in the ReC1A/TiO_2 (001) spectra is due to a lower resonant VSFGS response compared to the ReC0A/TiO_2 (001) system, so that the two contributions have similar magnitudes. The difference in resonant intensities may indicate that the ReC1A/TiO_2 (001) system exhibits less molecular ordering, i.e. a larger distribution of molecular tilt angles, which will cause contributions in equivalent but opposite directions to average out and yield an overall smaller VSFGS signal. A more disordered and thus less dense packing arrangement may also decrease the molecular surface density, which may also decrease the VSFGS signal size.

For the ReC0A/TiO_2 (001) system, any nonresonant response can be suppressed through delay of the visible pulse with respect to the IR pulse according to published procedures.[26] However, this simultaneously decreases the resonant signal intensity in the

VSFGS spectrum. For ReC1A/TiO_2 (001), the spectral features are too weak to allow for this nonresonant suppression, as the resonant features will also be eliminated. Unfortunately, this nonresonant contribution inhibits quantitative analysis of the ReC1A homodyne VSFG spectrum.

One possible solution to this dilemma is the use of phase-sensitive vibrational sum frequency generation spectroscopy (PS-VSFGS), which can separate the real and imaginary portions of the VSFGS spectrum based on their $\pi/2$ phase difference. The imaginary component contains any vibrational resonances, while the real component is the derivative of the imaginary plus any nonresonant response.[27] Phase-sensitive detection has the further advantage that the signal scales linearly with the chromophore density whereas it scales quadratically in the so-called (traditional) homodyne case.[28] This results in VSFGS spectra that are comparable to linear absorption spectra.

6.2.2. Theoretical Description of Phase-Sensitive Vibrational Sum Frequency Generation Spectroscopy (PS-VSFGS)

The theory of sum frequency generation has been examined in detail in Chapter 2 and thus will be only briefly outlined here. In general, the SFG response is given by:[6,29-32]

$$I(\omega_{SF}) \propto \left| \chi^{(2)}_{eff} E_{vis}(\omega_{vis}) E_{IR}(\omega_{IR}) \right|^2 \qquad (6.1)$$

where $E_{vis}(\omega_{vis})$ and $E_{IR}(\omega_{IR})$ are two incident electric fields. The effective nonlinear susceptibility $\chi^{(2)}_{eff}$ takes the form of:

$$\chi^{(2)}_{eff} = \left[\hat{\mathbf{e}}(\omega) \cdot \mathbf{L}(\omega)\right] \cdot \chi^{(2)} : \left[\mathbf{L}(\omega_1) \cdot \hat{\mathbf{e}}(\omega_1)\right]\left[\mathbf{L}(\omega_2) \cdot \hat{\mathbf{e}}(\omega_2)\right] \qquad (6.2)$$

where $\hat{\mathbf{e}}(\Omega)$ and $\mathbf{L}(\Omega)$ are the unit polarization vectors and Fresnel factors at frequency Ω, respectively, and $\chi^{(2)}$ is the nonlinear susceptibility tensor. $\chi^{(2)}$ can typically be decomposed into a sum of resonant ($\chi_R^{(2)}$) and nonresonant ($\chi_{NR}^{(2)}$) terms:

$$\chi^{(2)} = \chi_R^{(2)} + \chi_{NR}^{(2)} \tag{6.3}$$

The nonresonant portion of the susceptibility may result from both the interfacial molecules and the media on either side of the interface, and is typically considered to be the result of electronic transitions. The resonant portion of the nonlinear susceptibility results solely from the interfacial molecules and is a measure of their response to the incident electric fields. A full description of the form of $\chi_R^{(2)}$ is given in Chapter 2.

In the case where $\chi_R^{(2)}$ is much larger than $\chi_{NR}^{(2)}$, the projection of a particular vibrational mode on the laboratory axis can be determined by monitoring the SFG response as a function of the incident and generated polarizations. However, when $\chi_R^{(2)}$ is equal to or smaller than $\chi_{NR}^{(2)}$, it can be difficult to accurately quantify each contribution, prohibiting orientation analysis. This is the case for ReCnA/TiO_2 (001) when n = 1 – 4; we speculate that this is due to a lower VSFG response from the ReCnA (n = 1 – 4) systems compared to the ReC0A system, causing the resonant signal to be comparable to the nonresonant response from the TiO_2 substrate. In this case, phase-sensitive VSFGS (PS-VSFGS) can be used to distinguish the resonant and nonresonant contributions.

In the PS-VSFGS detection scheme, the phase and intensity of the sample SF field are measured by combining it with a stable broad "local oscillator" field, which is separated by a time τ with respect to the sample SF signal. The intensity of the phase-sensitive signal is thus:

$$I_{PS-VSFGS} = |\chi_s^{(2)} E_{Vis} E_{IR} + \chi_{lo}^{(2)} E_{Vis} E_{IR} e^{i2\pi\omega\tau}|^2$$
$$= \left|\chi_s^{(2)} E_{Vis} E_{IR}\right|^2 + \left|\chi_{lo}^{(2)} E_{Vis} E_{IR}\right|^2 + 2\,\mathrm{Re}[\chi_{lo}^{(2)} \chi_s^{(2)} E_{vis}^2 E_{IR}^2 e^{i2\pi\omega\tau}] \quad (6.4)$$

where χ_S and χ_{LO} refer to the nonlinear susceptibility of the sample and local oscillator, respectively. The time separation between the signal and local oscillator beams causes an interference pattern in the frequency domain with fringes that have a period inversely proportional to the optical path difference, i.e. $1/\tau$. The height of the fringes is determined by the magnitude of the so-called "cross-term", given by the last term in Equation 6.4. This term contains the desired sample information χ_S and can be separated from the other contributions through careful signal processing.[27,33] Specifically, the spectrum is first inverse Fourier Transformed into the time domain, where the $\mathrm{Re}[\chi_s^{(2)}\chi_{lo}^{(2)}E_{vis}^2E_{IR}^2\, e^{i2\pi\omega\tau}]$ cross-term is separated from the other terms by a time τ and can thus be isolated by application of a boxcar function. The result is then Fourier Transformed back into the frequency domain to yield:

$$I_{PS-VSFGS}(\omega) = \chi_{lo}^{(2)} \chi_s^{(2)} E_{vis}^2 E_{IR}^2 e^{i2\pi\omega\tau} \quad (6.7)$$

In order to extract the relevant molecular information contained in $\chi_s^{(2)}$, the resulting spectrum must be normalized against a standard sample of known $\chi^{(2)}$. In this experiment, a gold film was used. As gold has no resonances in the investigated spectral region, its response is purely real and flat and so $\chi_{Au}^{(2)}$ can be considered a constant. The sample spectrum can thus be normalized by the processed gold spectrum to yield the $\chi_s^{(2)}$ of interest:

$$\frac{\chi_{lo}^{(2)} \chi_s^{(2)} E_{vis}^2 E_{IR}^2 e^{i2\pi\omega\tau}}{\chi_{lo}^{(2)} \chi_{Au}^{(2)} E_{vis}^2 E_{IR}^2 e^{i2\pi\omega\tau}} e^{i\phi} = \frac{\chi_s^{(2)}}{\chi_{Au}^{(2)}} e^{i\phi} \quad (6.8)$$

The $e^{i\theta}$ term is included to describe any phase difference between the sample and gold spectra which can result from slightly different positioning between the ReCnA/TiO_2 and gold samples. This can be subsequently corrected by application of a phasing factor.

The phase-sensitive detection scheme has the advantage that $\chi_s^{(2)}$ is directly measured such that the real and imaginary parts can be separated and investigated individually. This is vital to our experiment because the imaginary component of $\chi_s^{(2)}$ contains the vibrational information while the real component is the derivative of the imaginary part plus any nonresonant responses. The average conformation of the molecules on the TiO_2 (001) surface can then be deduced by modeling the imaginary SF spectra as a function of molecular orientation.

6.2.3. Raw Phase-Sensitive Vibrational Sum Frequency Spectra of ReC0A/TiO_2 (001) and Au and Detailed Signal Processing Methods

The raw PS-VSFGS spectra of both ReC0A/TiO_2 (001) and a bare gold sample are shown in Figure 6.4, where y-cut quartz is used to generate the nonresonant local oscillator signal. Both spectra are in fact interferograms, though the interference pattern occurs over a much narrower spectral range for ReC0A/TiO_2 (001) compared to bare gold. This is expected, since interference between the sample/reference and local oscillator can only occur over regions where both have a nonzero spectral intensity. As ReC0A/TiO_2 (001) only exhibits SF signal at 2000 – 2050 cm^{-1}, its raw PS-VSFGS spectrum should only show interference over this spectral range. Gold, however, exhibits a broad nonresonant response and should therefore interfere with the local oscillator over all frequencies, as is seen in Figure 6.4b.

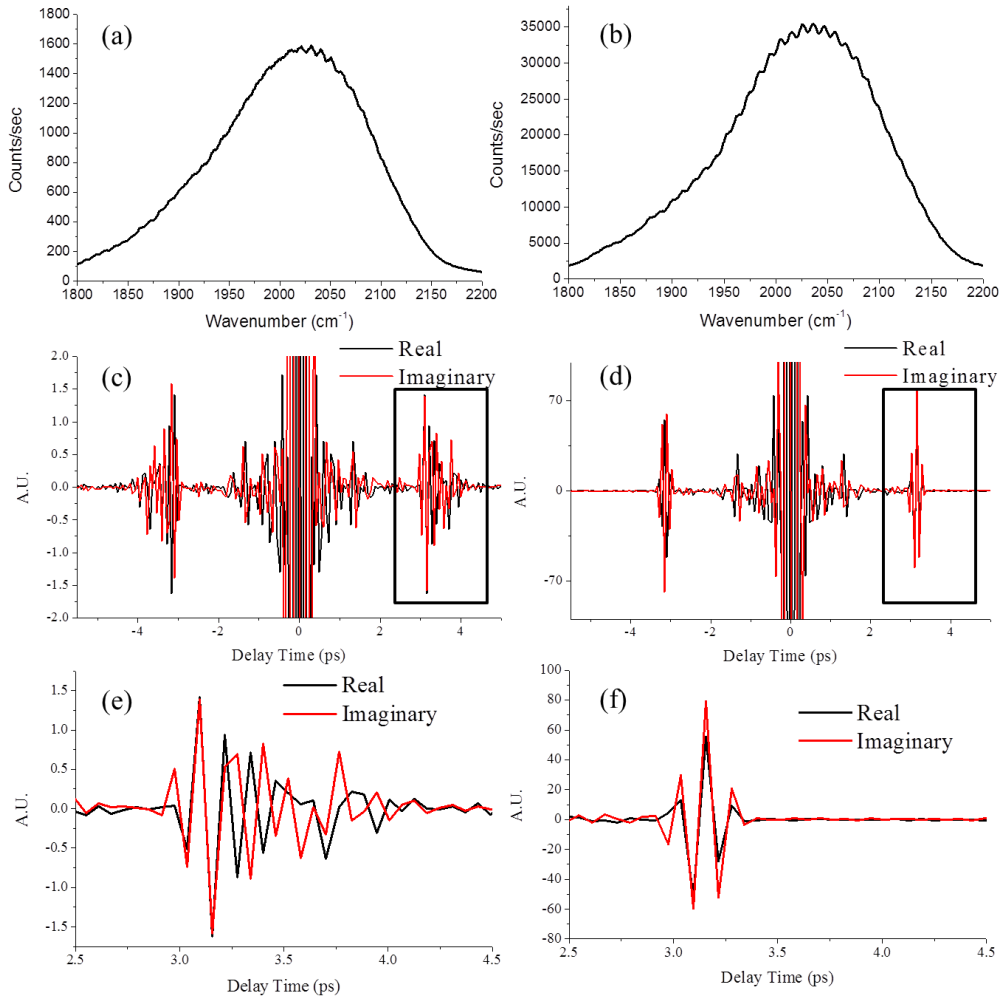

Figure 6.4. Raw PS-VSFGS spectra of (a) ReC0A/TiO_2 (001) and (b) a bare gold sample, where y-cut quartz is used to generate the nonresonant local oscillator signal. (c) and (d) Inverse Fourier Transforms of spectra shown in (a) and (c), respectively, where the homodyne contributions occur at $\tau = 0$ and the cross-terms occur at approximately $\tau = \pm 3.2$ ps. (e) and (f) Magnified view of the cross term indicated by the black box in (c) and (d), respectively.

The inverse Fourier Transforms of the PS-VSFGS spectra of ReC0A/TiO_2 (001) and bare gold are also shown in Figure 6.4, where the homodyne contributions occur at τ

= 0 and the cross-terms occur at approximately $\tau = \pm 3.2$ ps. In order to extract the relevant molecular information contained in $\chi_s^{(2)}$, the cross-term at $\tau = 3.2$ ps can be isolated from the larger contributions at $\tau = 0$ through utilization of a boxcar function, represented by the black box in Figures 6.4c and 6.4d. Figures 6.4e and 6.4f show a magnified view of the isolated cross-term for ReC0A/TiO_2 (001) and bare gold, respectively. The longer decay time for ReC0A/TiO_2 (001) can be attributed to the long-lived (~1 ps) vibrational free-induction decay (FID) of the a'(1) mode, compared to the instantaneous nonresonant response exhibited by gold.

Once the appropriate cross-term has been isolated, each spectrum can be Fourier Transformed back into the frequency domain, yielding another spectral interferogram. To produce a useful spectrum, the spectral interferogram of ReC0A/TiO_2 (001) must be normalized by that of bare gold. This will eliminate any contributions from the nonlinear susceptibility of the local oscillator, as shown in Equation 6.5. Assuming the nonlinear response from gold is real and constant, this should yield the real and imaginary spectra of $\chi_s^{(2)}$, normalized by some constant value. The spectral interferograms of ReC0A/TiO_2 (001) and bare gold are shown in Figure 6.5, as well as the appropriately normalized real and imaginary spectra of $\chi_s^{(2)}$ for ReC0A/TiO_2 (001). The imaginary component of the normalized spectrum corresponds to the resonant a'(1) symmetric stretch at 2040 cm^{-1}, while the real component corresponds to the derivative of the imaginary feature as well as a broad nonresonant feature. The nonresonant feature is attributed to the TiO_2 substrate and appears here because the PS-VSFGS experimental arrangement necessitates that the visible and IR beams precisely overlap temporally in order to generate the instantaneous nonresonant local oscillator signal. In the homodyne VSFGS arrangement, however, the

visible pulse is typically delayed with respect to the IR pulse. In this case, the instantaneous nonresonant response of the TiO_2 substrate has decayed entirely before the visible pulse arrives, while the vibrational FID of the a'(1) mode can be upconverted by the delayed visible pulse in order to generate the SF signal. The nonresonant contribution is thus suppressed while the resonant features remain.

The processed PS-VSFGS spectra can be compared with the homodyne spectrum according to:

$$I_{\text{homo}} = \left| \chi^{(2)}_{\text{Re}} + \chi^{(2)}_{\text{Im}} \right|^2 \qquad (6.9)$$

Figure 6.5d thus compares the previously obtained homodyne spectrum with the absolute value squared of the summed real and imaginary components of $\chi_s^{(2)}$ as determined from the PS-VSFGS spectra. Overall the spectra show very good agreement, except the PS-VSFGS spectrum shows an additional broad component above 2040 cm^{-1} which we once again attribute to the nonresonant signal of TiO_2. This discrepancy actually highlights the advantage of utilizing PS-VSFGS, as the resonant and nonresonant contributions seen in Figure 6.5d are completely separated in Figure 6.5c. This technique should enable us to isolate the resonant features of the VSFGS spectra for each molecule in the ReCnA series and thus allow for quantitative orientation analysis. In addition, the PS-VSFGS retains the phase information between different vibrational modes, which is lost in homodyne-detected VSFGS. This additional information provides a more complete picture of the ReCnA/TiO_2 (001) interface and may aid in determining the average molecular orientation.

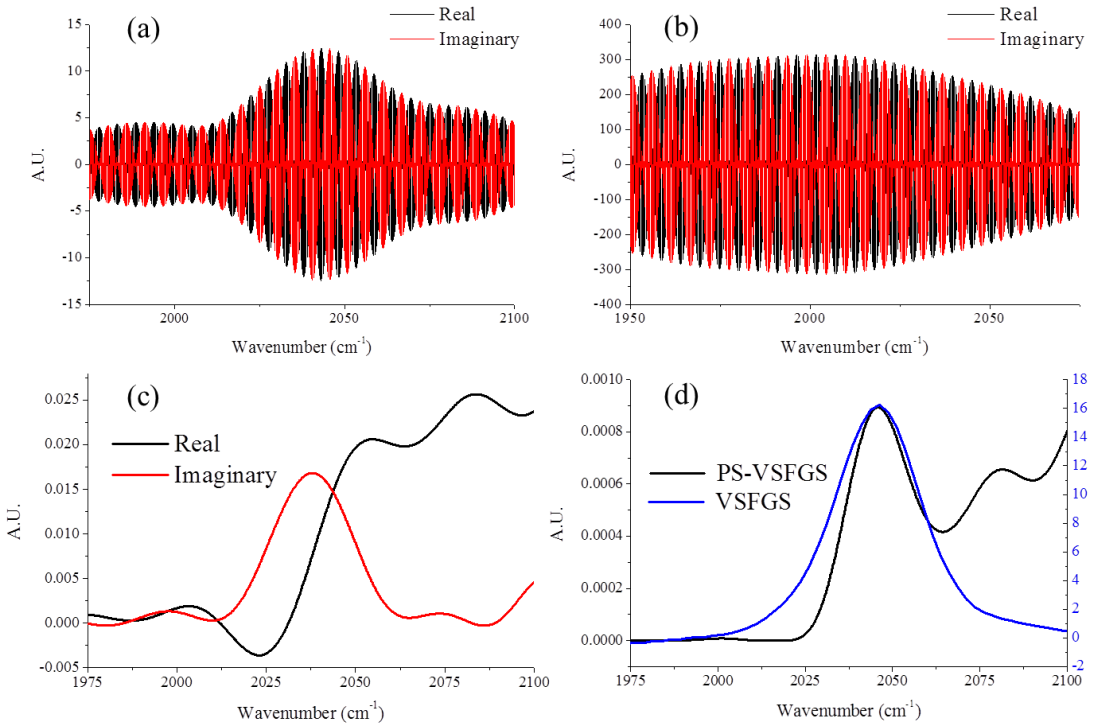

Figure 6.5. Final spectral interferograms of (a) ReC0A/TiO_2 (001) and (b) bare gold obtained after inverse Fourier Transform of the raw PS-VSFGS spectra, isolation of the cross-term at τ = 3.2 ps using a boxcar function, and subsequent Fourier Transform back into the frequency domain. (c) Real and imaginary $\chi_s^{(2)}$ spectra for ReC0A/TiO_2 (001) after normalization with the bare gold reference. (d) Comparison of the absolute value squared of the summed real and imaginary components of $\chi_s^{(2)}$ shown in (c) with the homodyne-detected VSFGS spectrum of ReC0A/TiO_2 (001). The color of the y-axis indicates which spectrum it is associated with.

6.2.4. Processed Phase-Sensitive Vibrational Sum Frequency Generation Spectra of ReCnA (n = 0 – 4) on TiO_2 (001)

The homodyne- and phase-sensitive-detected SFG spectra of the ReC0A complex on TiO_2 (001) in the carbonyl stretching region are shown in Figure 6.6. The FTIR spectrum of ReC0A on nanocrystalline TiO_2 is also shown for comparison As in the homodyne case, all complete PS-VSFGS spectra shown here were measured and subsequently pieced together over several spectral windows in order to eliminate excessive noise enhancement due to low mid-IR intensity. The imaginary PS-VSFGS component of ReC0A on TiO_2 (001) exhibits the a'(1) totally symmetric stretch at 2040 cm^{-1} also seen in the homodyne and FTIR spectra with no other bands observable at our signal-to-noise level. The real component of the ps-VSFGS spectrum is the derivative of the imaginary spectrum combined with a broad nonresonant feature, as described above. The good agreement between the homodyne and phase-sensitive VSFG spectra indicates that the alternative detection scheme employed in PS-VSFGS does not affect the experimental results.

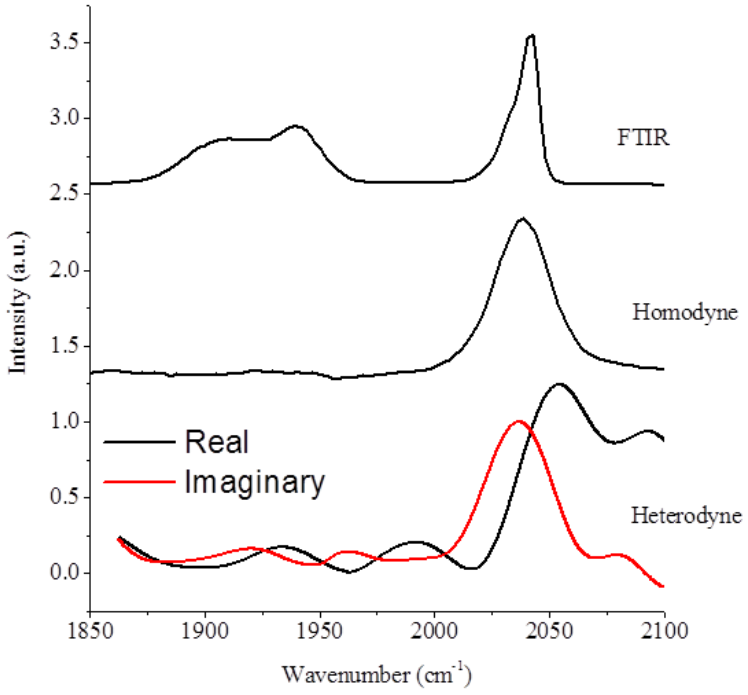

Figure 6.6. (top) FTIR spectrum of ReC0A on nanocrystalline TiO_2. (middle) Homodyne-detected and (bottom) phase-sensitive-detected VSFGS spectra of ReC0A on single crystal TiO_2 (001). Spectra are offset for clarity.

The homodyne- and phase-sensitive-detected VSFG spectra of ReC1A on TiO_2 (001) are shown in Figure 6.7 along with the FTIR of ReC1A on nanocrystalline TiO_2. As detailed in Section 6.2.1, the homodyne SFG spectrum of ReC1A displays two sharp features at 2030 and 1925 cm^{-1} and a broad feature that extends from 1925 cm^{-1} to the red beyond the investigated spectral region, which we attribute to the nonresonant response of the TiO_2 substrate. By contrast, the imaginary phase-sensitive spectrum displays two clear bands at 2030 and 1925 cm^{-1}, which we assign to the totally symmetric a'(1) carbonyl stretch and the anti-symmetric a'' and/or a'(2) modes, respectively. The a'(1) mode is out of phase relative to the a'(2) and a'' modes and they thus show up as positive

and negative peaks, respectively, in the PS-VSFGS imaginary spectrum. The real part of the phase-sensitive spectrum consists of the derivative of the imaginary spectrum on a broad and rather featureless background, consistent with a large nonresonant response. Figure 6.7 demonstrates that the PS-VSFGS technique is capable of efficiently separating the nonresonant and resonant SF responses into the real and imaginary PS-VSFGS spectra, respectively. The imaginary $\chi_s^{(2)}$ spectra can be simulated as a function of molecular tilt angle in order to determine the average molecular orientation.

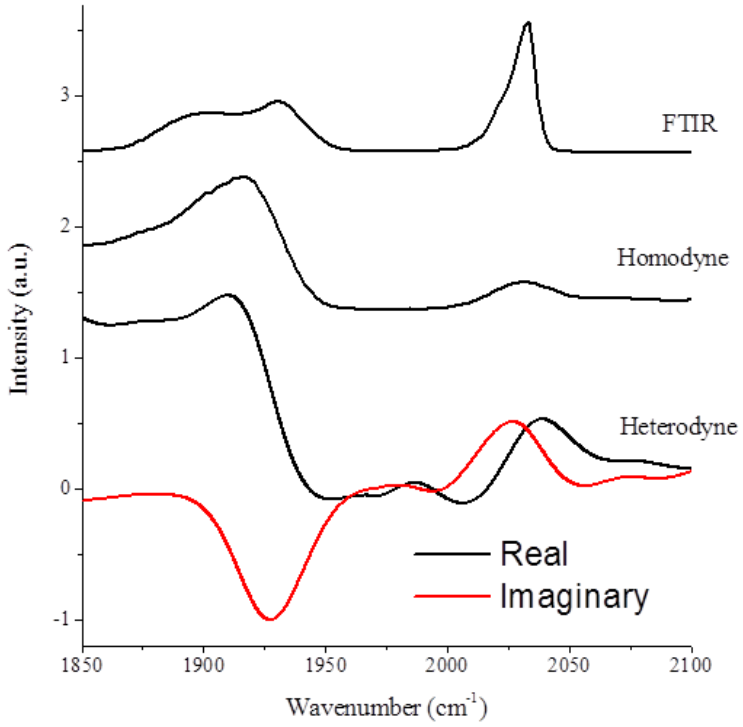

Figure 6.7. (top) FTIR spectrum of ReC1A on nanoporous TiO_2. (middle) Homodyne-detected and (bottom) phase-sensitive-detected VSFGS spectra of ReC1A on single crystal TiO_2 (001). Spectra are offset for clarity.

Based on the successful results for ReC1A/TiO_2 (001) shown in Figure 6.7, the entire ReCnA series (n = 0 – 4) on TiO_2 (001) was investigated using PS-VSFGS; the resulting spectra are shown in Figure 6.8. Although ReC0A only exhibits the a'(1) carbonyl stretch at 2040 cm^{-1}, the imaginary spectra of all other complexes show a sharp peak at 2030 cm^{-1} and broad peak around 1910 – 1940 cm^{-1}. We again assign the 2030 cm^{-1} band to the totally symmetric a'(1) carbonyl stretch. The hitherto unobserved low frequency band(s) can be assigned to the anti-symmetric a'' and/or a'(2) modes. The VSFG activity of either mode indicates that the extra methyl group(s) in the carboxyl linkers in ReCnA (n = 1 – 4) cause the orientation of the molecule on the TiO_2 (001) surface to substantially deviate from the surface normal. For each ReCnA (n = 1 – 4) spectrum, the real component of the phase-sensitive spectrum consists of the derivative of the imaginary spectrum on a broad, offset background, consistent with a large nonresonant response. The phase-sensitive detection scheme allows for the efficient separation of these two components and thus a quantitative orientation analysis could be performed.

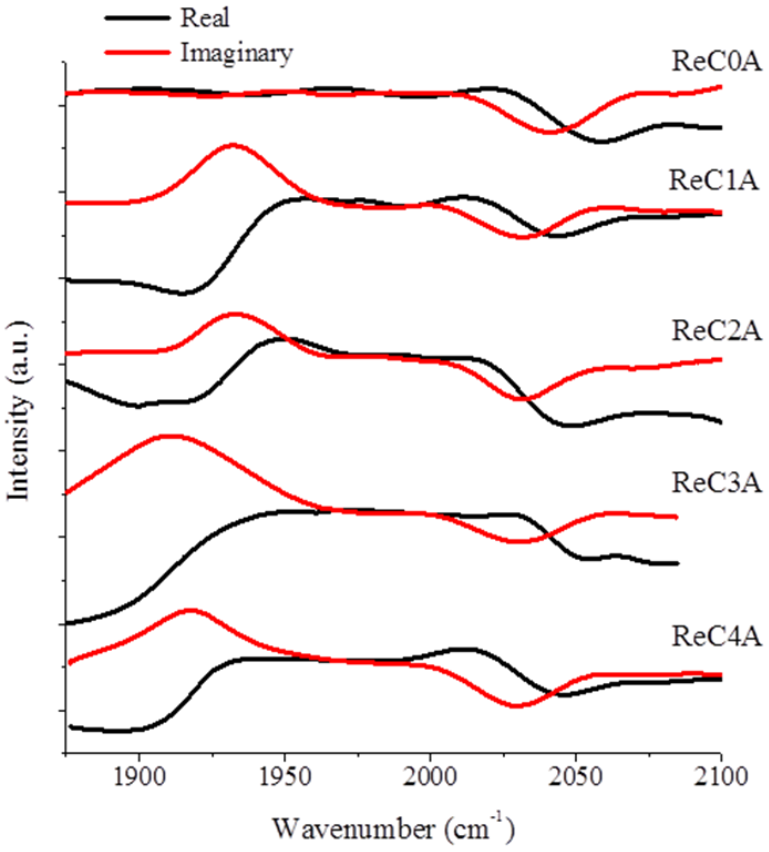

Figure 6.8. PS-VSFGS spectra of ReCnA (n = 0 – 4) on single crystal TiO_2 (001). Spectra are offset for clarity.

6.2.5. Theoretical Analysis of the PS-VSFGS Spectra of ReCnA (n = 0 – 4) on TiO_2 (001)

6.2.5.1. Determining Molecular Orientation from PS-VSFGS Spectra

In order to determine the average molecular orientation for each complex on the TiO_2 (001) surface, theoretical analysis was performed by Dequan Xiao *et al.* at Yale University. The anaylsis was based on *ab initio* simulation of the imaginary traces of the

phase-sensitive SFG spectra. A detailed description of the procedure for simulating the imaginary VSFGS spectra using the *ab initio* parameters of polarizability derivatives and dipole moment derivatives with respect to the normal mode coordinates can be found in their previous work.[48] For this study, the $\chi_R^{(2)}$ response was simulated for the PPP polarization combination.[6]

The orientation of the ReCnA chromophore on the TiO_2 (001) surface can be described in terms of the Euler angles θ, ϕ, and ψ, which transform the molecule from the molecular coordinates (a, b, c) to the surface Cartesian coordinates (X, Y, Z). An illustration of this process is shown in Figure 6.9. The three Euler angles are defined as follows: θ is the angle between the Z-axis and the normal of the bipyridyl plane (the c-axis), ψ is the angle between the long-axis (the b-axis) and the interaction line (the i-axis) of the ab plane and the XY plane, and ϕ is the angle between the i-axis and the Y-axis. Due to the C_4 symmetry of the rutile (001) surface, the Re-bipyridyl complexes can be distributed isotropically around the Z-axis, thus ϕ has an even distribution in the range of 0 – 360°. The θ and ψ angles are to be determined for each complex.

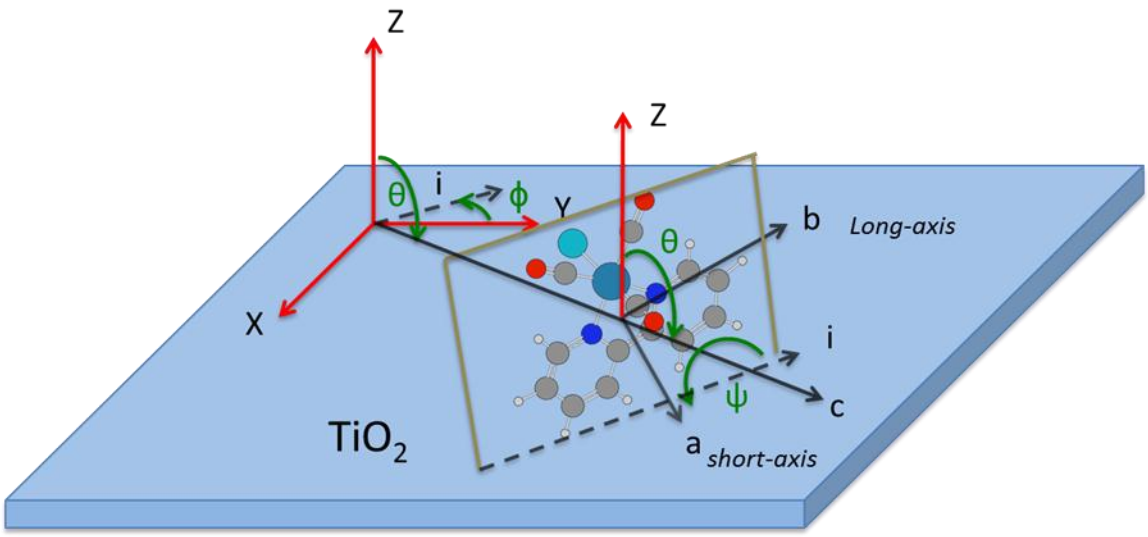

Figure 6.9.[1] Schematic illustration of the orientation angles describing the Re-bipyridyl complexes on the TiO_2 rutile (001) surface. Indexes X, Y and Z represent the Cartesian coordinate system of the surface, while indexes a, b and c represent the molecular coordinate system. These coordinate systems are related through the Euler transformation angles θ, ϕ, and ψ.

[1]With permission from D. Xiao *et al*.[34]

Table 6.1.[1] Intensity ratios (R_{amp}) of the low-frequency peak at ~1925 cm^{-1} relative to the high-frequency peak at ~2030 cm^{-1} for the ReCnA complexes shown in Figure 6.8.

ReCnA, n=	0	1	2	3	4
R_{amp}	0	-1.96	-1.04	-2.85	-1.19

[1]With permission from D. Xiao *et al*.[34]

To determine these orientation angles, the intensity ratio (R_{amp}) between the low frequency peak at ~1925 cm^{-1} and the high frequency peak at ~2030 cm^{-1} was calculated for each complex in Figure 6.8; the results are listed in Table 6.1. For ReC0A, $R_{amp} = 0$, as no peak appears in the lower frequency peak region. For n = 1 – 4, R_{amp} varies periodically with n. The imaginary SFG spectra of each ReCnA/TiO_2 (001) complex were then simulated by independently scanning every 5° for both the θ and ψ angles. The intensity ratios (R_{amp}) were calculated for the simulated spectra for particular sets of θ and ψ and compared to the experimental R_{amp} values listed in Table 6.1; the results are compared in Figure 6.10.

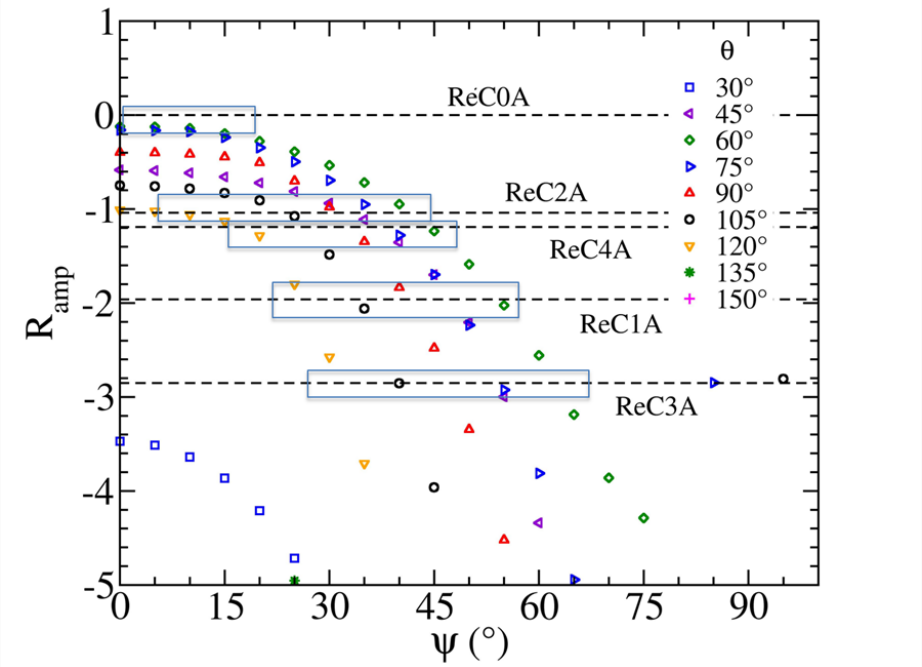

Figure 6.10.[1] Dependence of R_{amp} (i.e. intensity ratios of the lower frequency peak at ~1925 cm^{-1} to the higher frequency peak at ~2030 cm^{-1}) on the orientation angles θ and ψ for the simulated PS-VSFGS spectra.

[1]With permission from D. Xiao *et al.*[34]

We find that each experimental R_{amp} value corresponds to several sets of possible θ and ψ angles. For example, for R_{amp} = -1.19 in ReC4A, the possible sets of (θ, ψ) are: (60°, 50°), (75°, 40°), (45°, 35°), (90°, 35°), (105°, 25°), and (120°, 20°). To determine the correct orientation angles for each complex, the experimental PS-VSFGS spectrum was compared to the simulated spectrum for the selected sets of (θ, ψ) angles. The particular set of (θ, ψ) that resulted in the best fit between the experimental and simulated spectra was determined to be the correct set of orientation angles. The results for the ReCnA (n = 0 – 4) complexes are given in Table 6.2. The corresponding simulated VSFG spectra for these orientation angles are compared with the experimental PS-VSFGS spectra in Figure 6.11, where the experimental spectra have been shifted to match the calculated frequencies (corresponding to free ReC0A). For each complex, the simulated imaginary SFG spectrum matches fairly well with the experimental PS-VSFG spectrum.

Table 6.2.[1] Determined orientation angles (θ, ψ) for the ReCnA/TiO_2 (001) series, where n = 0 – 4. η is the complementary angle of θ.

ReCnA, n=	0	1	2	3	4
θ	75°	105°	75°	45°	45°
η	15°	-15°	15°	45°	45°
ψ	0°	35°	35°	55°	35°

[1]With permission from D. Xiao *et al*.[34]

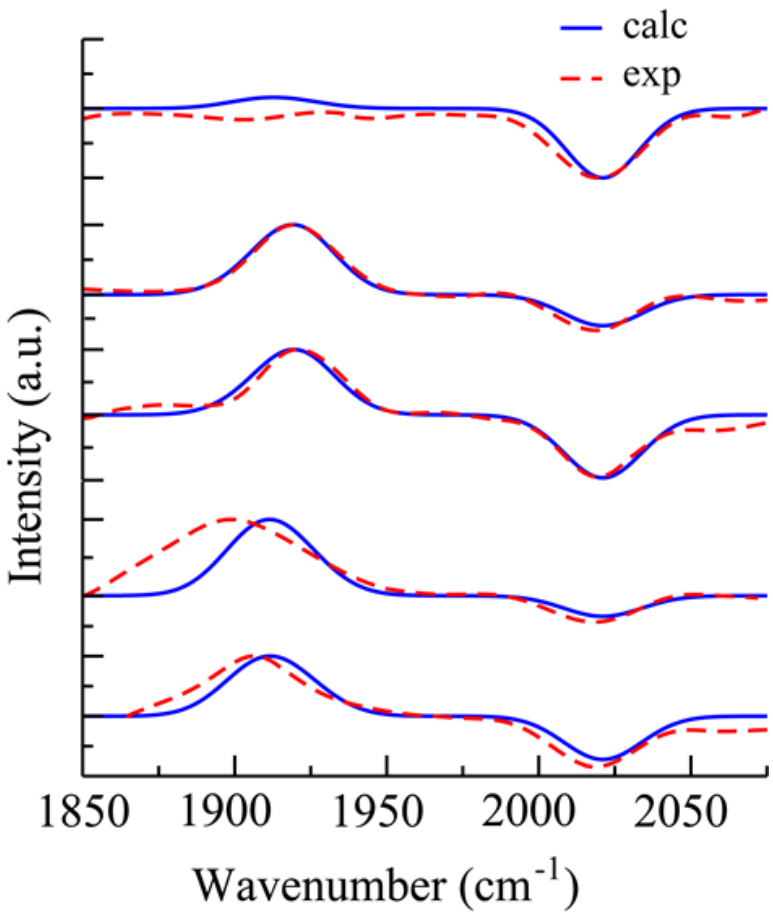

Figure 6.11.[1] Simulated imaginary SFG spectra (blue solid traces) with the determined orientation angles (θ, ψ) for the ReCnA/TiO_2 series (n = 0 – 4, from top to bottom), compared to the experimental PS-VSFGS spectra (red dash traces). Spectra are offset for clarity.

[1]With permission from D. Xiao *et al.*[34]

As shown in Table 6.2, both θ and ψ change significantly as n increases from 0 to 4. For convenience, we will describe the molecular orientation in terms of the η angle (as opposed to θ), as it represents the tilt angle between the molecular a-b plane and the laboratory Z-axis. In general, both η and ψ increase as n increases. Specifically, for n = 0

– 2, η remains relatively small, maintaining a magnitude of 15°; for n = 3 – 4, η increases to 45°. Meanwhile, the ψ-angle is 0 when n = 0, but as n increases from 1 to 4 n increases from 1 to 4, the ψ-angle increases up to 35° or higher. For n = 1, 2, or 4, ψ is 35°; and for n = 3, ψ is 55°.

The increase of η and ψ with n indicates that the short and long axes of the Re-bipyridyl ring increasingly tilt towards the TiO_2 (001) surface as the linking groups lengthen. We attribute this to a conformational change of the two linker groups in ReCnA as the number of methyl units increases. When n = 0, there is no -CH_2- linker, and the Re-bipyridyl ring is directly attached to its two carboxylic anchoring groups. In this case, their conformation on the surface should be very similar, so that the length of the two anchoring groups (i.e. from the bipyridyl ring to the TiO_2 surface) is nearly equal. It is thus reasonable that the long-axis of the bipyridyl plane is aligned parallel to the TiO_2 surface (i.e. ψ = 0) for ReC0A on TiO_2 (001). Meanwhile, the η angle is 15°, indicating the short-axis of the bipyridyl ring is tilted relative to the Z-axis by 15°. As n increases from 1 to 4, the average conformation of the two linkers can become very different, as the σ-bonds between -CH_2- groups can rotate freely. This results in unequal lengths of the two linking/anchoring groups. As the number of methyl groups increases, the length difference between the two linking groups can become increasingly different. As a result, the molecule tends to tilt further towards the TiO_2 surface. This is reflected in the increase of ψ and η to the range of 35 – 55° when n = 3 or 4, indicating that both the short and long axes of the bipyridyl ring are tilted significantly relative to the TiO_2 surface.

Given the larger number of average conformations as the anchoring groups lengthen, we speculate that there are also a greater number of exhibited molecular orientations with increasing n. This conclusion is consistent with the overall smaller VSFGS signal in the homodyne-detected experiment. Since the experimental PS-VSFGS spectra are the average of all molecular conformations, this may explain the spectral broadening at ~1915 cm^{-1} and poorer fit of the ReC3A and ReC4A complexes compared to ReCnA (n = 1 – 2).

6.2.5.2. Density Functional Theory (DFT) Calculations of ReCnA on TiO_2 (001)

Dequan Xiao *et al.* at Yale University sampled several possible binding conformations for the ReCnA complexes on the TiO_2 surface, and found that the average orientation angles deduced from the phase-sensitive SFG spectra are indeed accessible. Due to the large number of possible conformations as the chain length (n) increases, performing a global search would be prohibitively computationally expensive. Therefore, these results do not represent the global minimum, but rather the minimum of the sampled conformations as detailed Chapter 3. They are therefore indicative of the accessibility of the deduced orientation angles rather than the energetically minimized structures.

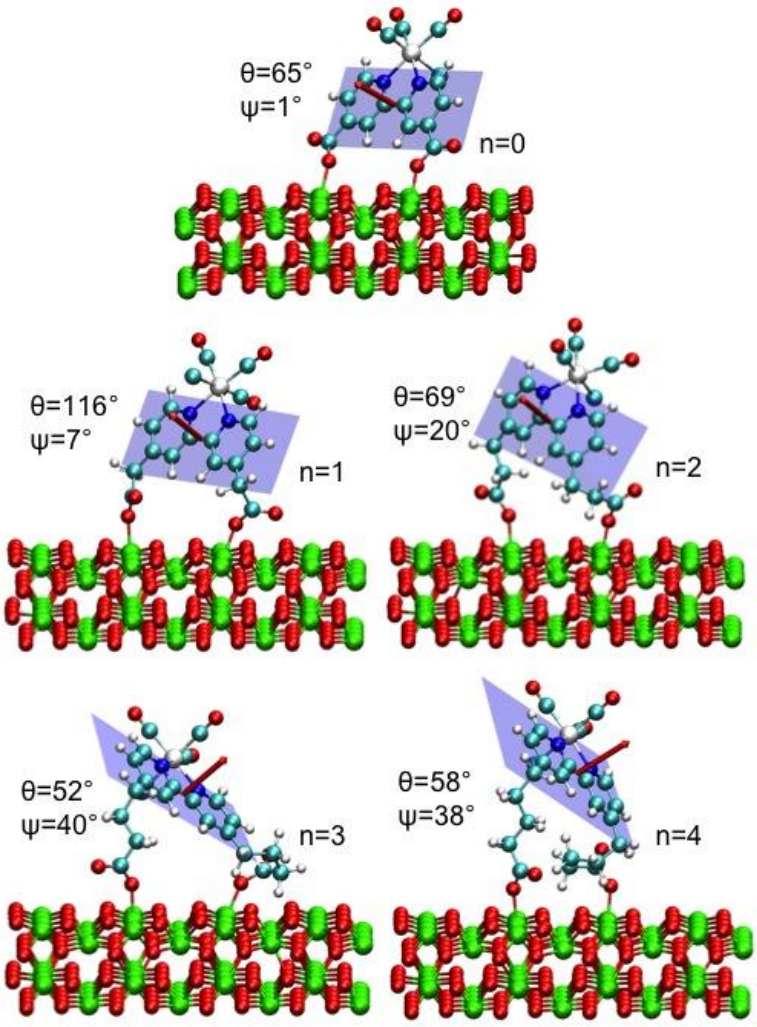

Figure 6.12.[1] Optimized binding structures of ReCnA (n = 0 – 4) on TiO_2 (001) with orientation angles (θ and ψ) close to the average orientation angles deduced from the phase-sensitive VSFG spectra (in Table 6.2).

[1]With permission from D. Xiao *et al*.[34]

Figure 6.12 shows the optimized binding structures for each ReCnA (n = 0 – 4) complex on the TiO_2 rutile (001) surface, where the optimized orientation angles (see Table 6.3) are close to the deduced average angles (see Table 6.2). The optimized conformations showed an increase in the orientation angles of the complexes with

increasing n, indicating that the ReCnA complexes tilt progressively more towards the TiO_2 surface as the methyl linkers lengthen. Additionally, as shown in Figure 6.12, as n increases from 0 to 4, the conformation difference between the two anchoring groups shows a tendency to enlarge. As a result, both the short axis (from a vertical orientation) and long axis (from a horizontal orientation) of the bipyridyl plane are tilted considerably relative to the TiO_2 surface. These results verify our anticipated correlation between the bipyridyl ring tiltation with the conformational change of the anchoring groups.

Table 6.3.[1] Orientation angles obtained via geometry optimization.

ReCnA, n=	0	1	2	3	4
θ	66°	106°	70°	51°	58°
H	24°	-16°	20°	39°	32°
Ψ	0°	8°	21°	40°	38°

[1]With permission from D. Xiao *et al*.[34]

6.2.5.3. Comparison with Previous Results

The orientation of ReC0A on TiO_2 (001) was investigated previously using homodyne-detected VSFGS and Density Functional Theory calculations (see Chapter 4 for details).[20] Polarization analysis of the a'(1) band in VSFGS spectra obtained using the PPP, SSP, and SPS polarization combinations indicated an average molecular tilt angle of 0 – 22°. Since only the high frequency mode was investigated, the direction of the tilt (i.e. η vs. ψ) was not determined.

In the present work, analysis of the PS-VSFGS spectra indicates an average molecular orientation where $\eta = 15°$ and $\psi = 0°$. It should be pointed out that the simulated spectra for ReC0A consistently overestimate the contribution of the two low frequency modes. This experimental result is consistent with our previous investigation of ReC0A on TiO_2 (001), in which the two lower frequency modes were not observed in the VSFGS spectra.[20] We speculated that this may be due to a near-resonance effect originating from the nearby MLCT band at ~420 nm, which would enhance the Raman cross section of the a'(1) mode but not the a'(2) or a" modes.[35,36] Based on this, a simplified model of the hyperpolarizability elements was used in the analysis. In the current work, the hyperpolarizability elements of free (unadsorbed) ReC0A were calculated directly from the IR and Raman transition dipole moments, as described in Chapter 3. An analysis of the Raman polarizability derivatives as a function of the sum frequency wavelength indicates negligible resonance effect of the MLCT transition. However, these calculations do not account for the effects of the adsorption of ReC0A on TiO_2, which causes a red-shift in the MLCT transition, as seen in Figure 6.13. This red-shift can be attributed to the stabilization of the π^* orbital of bipyridine due to its strong interaction with the empty d orbitals of the bonded Ti atoms. This may push the system closer to near-resonance. These effects are expected to be much less significant for the ReCnA (n = 1 – 4) complexes, since the CH_2 spacer(s) reduce the amount of electron delocalization into the carboxylate groups, thus insulating the molecule from the effects of TiO_2 adsorption. If the ReC0A/TiO_2 system is approaching near-resonance as explained above, we can expect this to further enhance the difference between the high and low frequency modes, which is more consistent with the experimental results. This

may also explain the much larger signal size for ReC0A on TiO_2 (001) compared to ReCnA (n = 1 – 4).

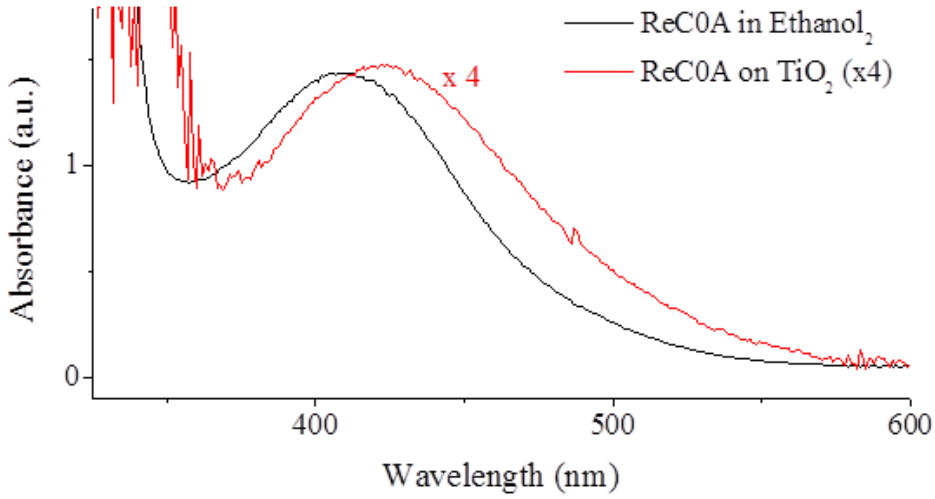

Figure 6.13. UV-visible absorption spectra of ReC0A in ethanol and ReC0A adsorbed onto a nanocrystalline TiO_2 film.

6.3. Summary

Phase-sensitive VSFG spectroscopy has been used to determine the adsorption geometry of a family of model electrocatalysts, ReCnA (n = 0 – 4), on a single crystal TiO_2 (001) surface. The imaginary PS-VSFGS spectra exhibited phase-sensitive VSFG peaks in the regions of 2030 – 20 40 cm^{-1} and 1925 cm^{-1}, originating from a combination of CO stretches. The intensity ratio (R_{amp}) of the two peaks in the PS-VSFGS spectra is associated with the average molecular orientation of each ReCnA complex relative to the TiO_2 (001) surface. Imaginary PS-VSFGS traces were simulated by Dequan Xiao *et al.* at Yale University with varying orientation angles in order to reproduce the experimental

spectra. Based on the experimental R_{amp} values and simulated imaginary spectra, the orientation angles for each complex in ReCnA (n = 0 – 4) were determined. These orientation angles were found to be closely correlated with the average lengths of the two linking anchoring groups. Specifically, as the number of methyl groups in the linkers increases, the short and long axes of the π-conjugated ring of the ReCnA complex tilt further towards the TiO_2 surface. We attribute this to the fact that the average conformation of the two linkers can become very different as n increases, as the σ-bonds between -CH_2- groups can rotate freely. We additionally speculate that, given the larger number of average conformations as the anchoring groups lengthen, it is likely that there are a greater number of exhibited molecular orientations with increasing n, all of which are sampled in the PS-VSFGS experiment. Increasing the length of the anchoring groups thus produces a more tilted and likely less ordered array of molecules on the semiconductor surface. This study thus demonstrates the ability to prepare an electrocatalyst-semiconductor system with a preferred average molecular arrangement based on the anchoring groups, though the ability to select a specific tilt angle may come at the cost of reducing overall systematic ordering.

6.4. References

(1) Prezhdo, O. V.; Duncan, W. R.; Prezhdo, V. V. *Accounts of Chemical Research* **2008**, *41*, 339.

(2) Adams, D. M.; Brus, L.; Chidsey, C. E. D.; Creager, S.; Creutz, C.; Kagan, C. R.; Kamat, P. V.; Lieberman, M.; Lindsay, S.; Marcus, R. A.; Metzger, R. M.;

Michel-Beyerle, M. E.; Miller, J. R.; Newton, M. D.; Rolison, D. R.; Sankey, O.; Schanze, K. S.; Yardley, J.; Zhu, X. *Journal of Physical Chemistry B* **2003**, *107*, 6668.

(3) Kamat, P. V.; Meisel, D. *Current Opinion in Colloid & Interface Science* **2002**, *7*, 282.

(4) O'Regan, B.; Gratzel, M. *Nature* **1991**, *353*, 737.

(5) Gratzel, M. *MRS Bulletin* **2005**, *30*, 23.

(6) Zhuang, X.; Miranda, P. B.; Kim, D.; Shen, Y. R. *Physical Review B* **1999**, *59*, 12632.

(7) Lambert, A. G.; Davies, P. B.; Neivandt, D. J. *Applied Spectroscopy Reviews* **2005**, *40*, 103.

(8) Wang, H. F.; Gan, W.; Lu, R.; Rao, Y.; Wu, B. H. *International Reviews in Physical Chemistry* **2005**, *24*, 191.

(9) Rao, Y.; Comstock, M.; Eisenthal, K. B. *Journal of Physical Chemistry B* **2006**, *110*, 1727.

(10) Hawecker, J.; Lehn, J. M.; Ziessel, R. *J Chem Soc Chem Comm* **1984**, 328.

(11) Hawecker, J.; Lehn, J. M.; Ziessel, R. *Helv Chim Acta* **1986**, *69*, 1990.

(12) Yam, V. W. W.; Lau, V. C. Y.; Cheung, K. K. *Organometallics* **1995**, *14*, 2749.

(13) Hayashi, Y.; Kita, S.; Brunschwig, B. S.; Fujita, E. *Journal of the American Chemical Society* **2003**, *125*, 11976.

(14) Fujita, E. H., Y.; Kita, S.; Brunschwig, B. S. In *7th International Conference on Carbon Dioxide Utilization*; Sang-Eon Park, J.-S. C., Kyu-Wan Lee, Ed.; Elsevier: Seoul, Korea, 2004.

(15) Fujita, E.; Muckerman, J. T. *Inorg Chem* **2004**, *43*, 7636.

(16) Takeda, H.; Koike, K.; Inoue, H.; Ishitani, O. *Journal of the American Chemical Society* **2008**, *130*, 2023.

(17) Benson, E. E.; Kubiak, C. P.; Sathrum, A. J.; Smieja, J. M. *Chemical Society Reviews* **2009**, *38*, 89.

(18) Smieja, J. M.; Kubiak, C. P. *Inorganic Chemistry* **2010**, *49*, 9283.

(19) Cecchet, F.; Alebbi, M.; Bignozzi, C. A.; Paolucci, F. *Inorganica Chimica Acta* **2006**, *359*, 3871.

(20) Anfuso, C. L.; Snoeberger, R. C.; Ricks, A. M.; Liu, W. M.; Xiao, D. Q.; Batista, V. S.; Lian, T. Q. *JACS* **2011**, *133*, 6922.

(21) She, C. A., Neil A.; Guo, Jianchang; Liu, Fang; Goh, Wan-Hee; Chen, Dai-Tao; Mohler, Debra L.; Tian, Zhong-Qun; Hupp, Joseph T.; Lian, Tianquan. *Journal of Physical Chemistry B* **2005**, *109*, 19345.

(22) Anderson, N. A.; Ai, X.; Chen, D.; Mohler, D. L.; Lian, T. *Journal of Physical Chemistry B* **2003**, *107*, 14231.

(23) She, C.; Guo, J.; Irle, S.; Morokuma, K.; Mohler, D. L.; Zabri, H.; Odobel, F.; Youm, K. T.; Liu, F.; Hupp Joseph, T.; Lian, T. *J. Phys. Chem. A.* **2007**, *111*, 6832.

(24) Fenter, P.; Eisenberger, P.; Liang, K. S. *Phys Rev Lett* **1993**, *70*, 2447.

(25) Asbury, J. B.; Hao, E.; Wang, Y.; Lian, T. *J. Phys. Chem. B* **2000**, *104*, 11957.

(26) Lagutchev, A.; Hambir, S. A.; Dlott, D. D. *Journal of Physical Chemistry C* **2007**, *111*, 13645.

(27) Pool, R. E.; Versluis, J.; Backus, E. H. G.; Bonn, M. *Journal of Physical Chemistry B* **2011**, *115*, 15362.

(28) Bredenbeck, J.; Ghosh, A.; Nienhuys, H.-K.; Bonn, M. *Accounts of Chemical Research* **2009**, *42*, 1332.

(29) Shen, Y. R. *The principles of nonlinear optics*; J. Wiley: New York, 1984.

(30) Feller, M. B.; Chen, W.; Shen, Y. R. *Physical Review A: Atomic, Molecular, and Optical Physics* **1991**, *43*, 6778.

(31) Hirose, C.; Akamatsu, N.; Domen, K. *Journal of Chemical Physics* **1992**, *96*, 997.

(32) Rao, Y.; Tao, Y. S.; Wang, H. F. *Journal of Chemical Physics* **2003**, *119*, 5226.

(33) Mondal, J. A.; Nihonyanagi, S.; Yamaguchi, S.; Tahara, T. *JACS* **2010**, *132*, 10656.

(34) Anfuso, C. L.; Xiao, D.; Ricks, A. M.; Negre, C. F. A.; Batista, V. S.; Lian, T. **2012**, to be submitted.

(35) Waterland, M. R.; Howell, S. L.; Gordon, K. C. *Journal of Physical Chemistry A* **2007**, *111*, 4604.

(36) Gamelin, D. R.; George, M. W.; Glyn, P.; Grevels, F.-W.; Johnson, F. P. A.; Klotzbuecher, W.; Morrison, S. L.; Russell, G.; Schaffner, K.; Turner, J. J. *Inorg Chem* **1994**, *33*, 3246.

Chapter 7: Vibrational Relaxation of a Rhenium CO_2-Reduction Catalyst on Semiconductor and Metal Surfaces

7.1. Introduction

Vibrational energy flow within catalytic adsorbates on electrodes is related to a number of complex chemical surface processes, such as adsorption, desorption, and reaction.[1] Vibrational energy dynamics can differ significantly between molecules in solution and at surfaces due to the interaction with the electrode in the latter case; this can subsequently stabilize or destabilize the catalytic intermediates towards reaction. Additionally, the dynamics (and catalytic activity) can vary depending on the surface and the nature of the adsorbate-substrate coupling, which is dependent on a number of parameters including the nature of the substrate electronic structure. Metals, for instance, exhibit a continuum of electronic states, so that conduction electrons may be excited from just below to just above the Fermi level by an arbitrarily small amount of energy in a process known as electron-hole pair (EHP) excitation.[2] Semiconductors, on the other hand, have larger, more discrete bandgaps, inhibiting this relaxation pathway.

Numerous studies have focused on the flow of vibrational energy for adsorbates on surfaces and found that several relaxation pathways exist, including energy transfer to other internal vibrational modes of the adsorbate, to other nearby adsorbates, and to the surface, through either coupling to substrate phonons or through the excitation of electron-hole pairs in the substrate.[3,4] Unfortunately, although numerous methods exist to investigate vibrational energy dynamics in the bulk, accessing the relatively small number of molecules at surfaces has proven experimentally challenging. In this regard,

vibrational sum frequency generation spectroscopy (VSFGS) has proven to be a useful technique for performing interfacial vibrational spectroscopy.[5-8] As a second-order optical technique, it is forbidden in media with inversion symmetry but allowed at the interface where the inversion symmetry is necessarily broken. VSFGS is thus surface-specific, giving it a distinct advantage over other optical techniques and allowing for a molecular-level picture of interfacial systems.

Although primarily used for static vibrational spectroscopy, the VSFGS technique has also been extended to include time-resolved measurements.[1] Until recently, these studies were primarily based on narrowband infrared (IR) sources with picosecond time resolution, limiting their applicability to systems exhibiting picosecond molecular dynamics.[9-23] Additionally, the narrowband IR pulses used meant that only a single vibrational band could be probed at one time, prohibiting the simultaneous monitoring of intermediate excited states. The recent advent of regeneratively amplified Ti:Sapphire laser systems, which are capable of producing short ($\leq$ 150 fs) amplified pulses, have now opened the door to performing broadband time-resolved VSFGS (BB-TR-VSFGS) on the femtosecond time scale. Use of broadband IR pulses allows for the collection of an entire vibrational spectrum (~100 – 150 cm^{-1} spectral window) within a single laser shot,[24] while the faster time scale allows for the monitoring of ultrafast vibrational dynamics. In the case of IR-pumped BB-TR-VSFGS, this permits simultaneous monitoring of the ground-state bleach, excited state absorption, and any nearby coupled vibrational transitions. The kinetics of these transitions can be compared to deduce vibrational lifetimes and relaxation pathways on the femtosecond time scale. Several such studies have now been performed, elucidating femtosecond vibrational dynamics of

interfacial systems.[1,25-31] However, to date, these studies have primarily been performed on liquid/liquid or liquid/air interfaces. Although these systems are fundamentally interesting, a great deal of fascinating chemistry occurs at the air/solid and liquid/solid interfaces, such as many types of catalysis and electrochemical reactions.

Thus far, only diatomic[9-23] and small polyatomic[11-15] adsorbates (< 8 atoms) have been investigated on metal and semiconductor surfaces using TR-VSFGS, and these studies have been limited to the use of narrowband IR and picosecond timescales. We are interested in extending these studies to include BB-TR-VSFGS of model adsorbate/electrode interfaces, and furthermore we wish to investigate the vibrational energy dynamics in relevant catalytic systems. Several tricarbonyl rhenium(I) complexes and their derivatives have been explored in recent years for the catalytic reduction of CO_2 to CO.[32-40] Although these catalysts are free to diffuse in homogeneous systems, the catalytic reaction is driven by the electron transfer process at the electrode. Therefore, most of the electrocatalytic processes occur at the electrode surface.[41,42] Additionally, numerous studies have reported enhanced catalytic turnover in heterogeneous systems, where these complexes are immobilized on the electrode surface.[42-46] The coordination of these catalysts to electrode surfaces may affect the efficiency of electron transfer and electrocatalytic reduction,[47-51] which are also intricately related to the rates and mechanisms of vibrational energy flow for adsorbates on electrodes.[1] A detailed study of the vibrational energy flow for these adsorbed complexes may shed light on the complicated reaction dynamics in these electrocatalytic systems. Additionally, comparison of the vibrational energy dynamics at metal and semiconductor surfaces may

help elucidate the mechanism of vibrational relaxation and the extent of adsorbate-substrate vibrational coupling for each system.

In this Chapter, we have investigated the vibrational energy dynamics of $Re(CO)_3Cl(dcbpy)$ (dcbpy = 4,4′-dicarboxy-2,2′-bipyridine) (ReC0A, shown in Figure 7.1a) on rutile TiO_2 (110) and ReC0A modified to chemisorb on a gold substrate (ReC0-Au, shown in Figure 7.1b) using IR-pumped BB-TR-VSFGS on the femtosecond time scale. In particular, we have concentrated on elucidating the vibrational dynamics of the CO stretching modes shown in Figure 7.1c. Since CO_2 reduction is known to occur at the rhenium center, monitoring the vibrational dynamics of the carbonyl stretches should shed light on the vibrational energy flow rates and mechanisms most relevant to the catalytic process.

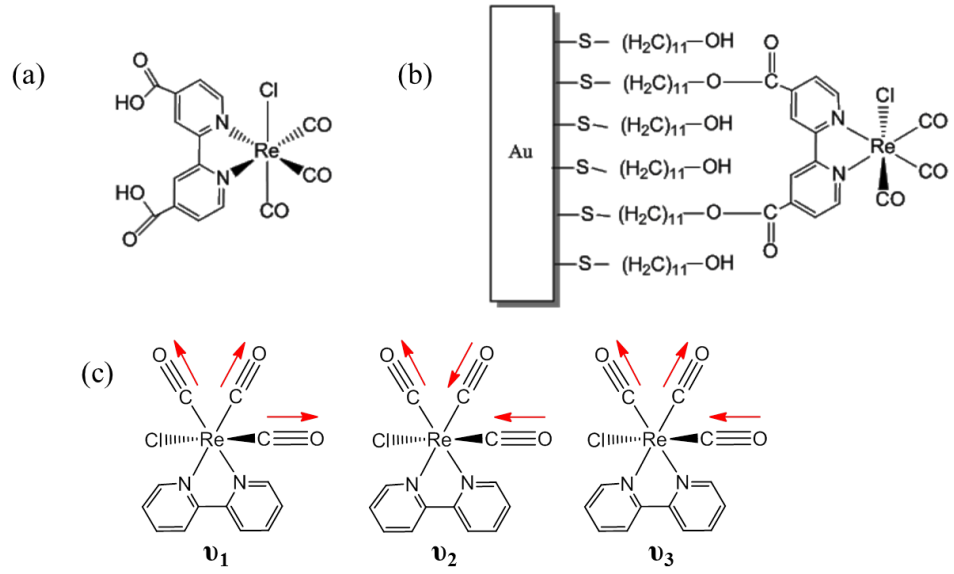

Figure 7.1. Schematic structure of (a) ReC0A and (b) ReC0-Au. (c) The three carbonyl stretches of ReC0A-type complexes: an in-phase symmetric a'(1) stretch (υ_1), an anti-symmetric a" stretch (υ_2), and an out-of-phase symmetric a'(2) stretch (υ_3).

7.2. Theory of Time-Resolved Vibrational Sum Frequency Generation Spectroscopy

The theory of sum frequency generation has been examined in detail in Chapter 2 and thus will be only briefly outlined here. In general, the sum frequency response is given by:[5,6,8]

$$I(\omega) \propto \left|\chi^{(2)}\right|^2 I_1(\omega_1) I_2(\omega_2) \qquad (7.1)$$

where $I_1(\omega_1)$ and $I_2(\omega_2)$ are the two incident fields and $\chi^{(2)}$ is the second order susceptibility tensor. $\chi^{(2)}$ can typically be decomposed into a sum of resonant ($\chi_R^{(2)}$) and nonresonant ($\chi_{NR}^{(2)}$) terms:

$$\chi^{(2)} = \chi_{NR}^{(2)} + \chi_R^{(2)} \qquad (7.2)$$

In the case of broadband VSFGS, a narrowband visible pulse and a broadband infrared pulse are overlapped spatially and temporally at an interface to produce the SF response, which is resonantly enhanced when the IR frequency coincides with that of a molecular vibration. In this case, the resonant portion of the nonlinear susceptibility can be expressed as:

$$\chi_R^{(2)} \propto \sum_q \frac{A_q}{\omega_q - \omega_{IR} + i\Gamma_q} e^{\varphi_q} \qquad (7.3)$$

where ω_{IR} is the frequency of the incident IR pulse and A_q, ω_q, Γ_q, and φ_q are the amplitude, frequency, linewidth, and relative phase of the q^{th} vibrational mode, respectively. The sum is over all vibrational modes of the interfacial molecules. The amplitude term for a particular transition is given by:

$$A_v \propto \boldsymbol{\mu}_{v'v} \boldsymbol{\alpha}_{vv'} \left(N_v - N_{v'}\right) \qquad (7.4)$$

where $\boldsymbol{\mu}_{\upsilon\upsilon'}$ is the IR transition moment, $\boldsymbol{\alpha}_{\upsilon\upsilon'}$ is the Raman transition moment, and $N_{\upsilon} - N_{\upsilon'}$ is the population difference between the two levels of the transition. Based on these equations, we can write an expression for the VSFGS spectra of a particular system.

In an IR pump-VSFG probe experiment, the sample is first excited by an intense infrared pump at a resonant vibrational frequency, and VSFGS is used to subsequently probe the system at various delay times after the pump pulse. Let us consider the case where we are exciting a single vibrational mode, the a'(1) (υ_1) mode. In the absence of an excitation pump pulse, the population of the first excited state is assumed to be negligible and $N_{0,q} = N_T = 1$. Assuming we are monitoring a single vibrational mode, we can write for the unpumped system:

$$\chi_{un}^{(2)} = \chi_{NR}^{(2)} + \frac{A_{01}}{\omega_{01} - \omega_{IR} + i\Gamma_{01}} e^{i\phi} \qquad (7.5)$$

where A_{01}, ω_{01}, and Γ_{01} are the amplitude, frequency, and linewidth of the $0 \rightarrow 1$ transition of the resonant SF mode.

Following excitation, the nonlinear susceptibility $\chi^{(2)}$ evolves over time. Specifically, the population transfer from the $\upsilon = 0$ to the $\upsilon = 1$ state induces a ground state bleach (GSB) at probe frequencies corresponding to the $0 \rightarrow 1$ transition and an excited state absorption (EA) at probe frequencies corresponding to the $1 \rightarrow 2$ transition. Additional bands may appear over time due to coupling of the initially excited mode with other nearby modes in the molecule. Assuming the pump intensity is sufficiently low that only a single vibrational mode is directly excited, the nonlinear susceptibility after excitation becomes:

$$\chi_{p}^{(2)} = \chi_{NR}^{(2)} + \left(\frac{A_{01}(N_0 - N_1)}{\omega_{01} - \omega_{IR} + i\Gamma_{01}} + \frac{A_{12}(N_1 - N_2)}{\omega_{12} - \omega_{IR} + i\Gamma_{12}} + \frac{A_{01}^{C}(N_1^{C} - N_{11})}{\omega_{01}^{C} - \omega_{IR} + i\Gamma_{01}^{C}}\right) e^{i\phi} \qquad (7.6)$$

where A_{12}, ω_{12}, and Γ_{12} are the amplitude, frequency, and linewidth of the $1 \rightarrow 2$ transition of the resonant SF mode, N_1^C is the population of the coupled mode(s), and A_{01}^C, ω_{01}^C, and Γ_{01}^C are the amplitude, frequency, and linewidth of the $0 \rightarrow 1$ transition with one quantum of vibration in the coupled mode(s). Here, we have made the assumption that all three resonant terms will have approximately the same phase with respect to the nonresonant background.

To simplify Equation 7.6, we can write the total population N_T in terms of the ground and excited state vibrational populations, as well the sum population of any modes to which the excited mode may couple, which we denote N_1^C.

$$N_T = N_0(t) + N_1(t) + N_1^C(t) = 1 \qquad (7.7)$$

where $N_0(t)$ is the time-dependent ground state population of the a'(1) mode, $N_1(t)$ is the time-dependent excited state population of the a'(1) mode, and $N_1^C(t)$ is the time-dependent population of any modes coupled to this vibration. We include the last term for our particular systems because carbonyl stretching modes are known to couple with each other in a number of metal carbonyl systems.[52-54] After a specific CO mode is excited (i.e. $|00\rangle \rightarrow |10\rangle$), it may equilibrate with another anharmonically coupled CO mode with a characteristic coupling time $\tau_{v\text{-}v}$ (i.e. $|10\rangle \rightarrow |01\rangle$). The coupled modes will then relax together with a population relaxation lifetime T_1.

Two-dimensional vibrational spectra of a very similar rhenium bipyridyl complex show that all three CO stretch modes are coupled.[55] We can thus expect that we may see a similar effect in the ReC0A/TiO_2 and ReC0-Au vibrational dynamics. Based on this, we can model the spectra according to the vibrational relaxation scheme shown in Figure 7.2. In this model, we can assume that the initial IR excitation directly generates only the

|100> state (with one quanta in the a'(1) mode). Population in |100>, $N_1(t)$, creates a GSB in the a'(1) band (transition 1 in Figure 7.2) and an associated EA (transition 2). It is strongly coupled with |010> and |001> states (with one quanta in the a" and a'(2) modes, respectively) with a population equilibration time of $\tau_{v\text{-}v}$. The coupled states will then relax together with a vibrational relaxation time T_1. Population in the |010> and |001> levels will contribute to both the GSB (transition 1) as well as two new EA peaks (transitions 3 and 4). However, the 2D vibrational spectra of a similar complex indicate that transitions 2, 3 and 4 all have the same frequency and will thus be indistinguishable in our experiment.[55] We can therefore use a single term $N_1^C(t)$ to describe the total (sum) time-dependent population of the coupled |010> and |001> states. The GSB and EA associated with the a'(2) and a" modes are shifted outside the IR frequency window used in the time-resolved measurements described here and thus we can neglect these terms in Equation 7.6.

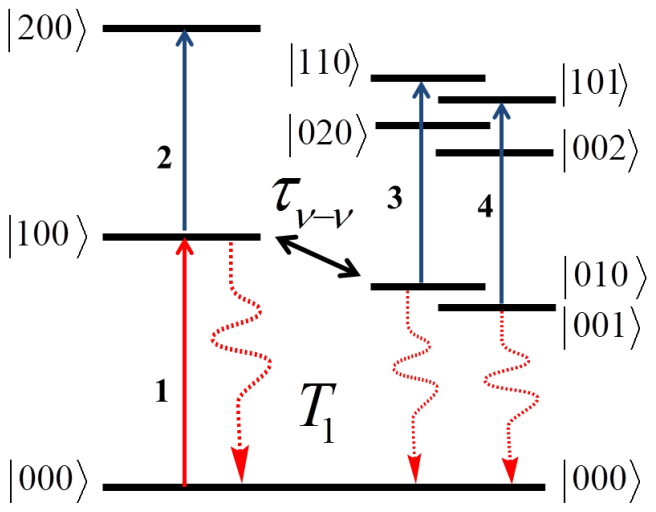

Figure 7.2. Vibrational energy level scheme of the coupled CO stretching modes of ReC0A-type complexes.

We can assume that after the initial IR excitation and equilibration, we will only have significant population in the |000>, |100>, |010>, and |001> states. We can therefore neglect terms N_2 and N_{11} (the population of the |110> or |101> states). The IR pump-VSFG probe signal is thus given by:

$$\begin{aligned}\Delta I &\propto \left|\chi_p^{(2)}\right|^2 - \left|\chi_{un}^{(2)}\right|^2 \\ &\propto \left|\chi_{NR}^{(2)} + \left(\frac{A_{01}(N_0 - N_1)}{\omega_{01} - \omega_{IR} + i\Gamma_{01}} + \frac{A_{12}N_1}{\omega_{12} - \omega_{IR} + i\Gamma_{12}} + \frac{A_{01}^C N_1^C}{\omega_{01}^C - \omega_{IR} + i\Gamma_{01}^C}\right)e^{i\phi}\right|^2 \\ &\quad - \left|\chi_{NR}^{(2)} + \frac{A_{01}}{\omega_{01} - \omega_{IR} + i\Gamma_{01}}e^{i\phi}\right|^2\end{aligned} \tag{7.8}$$

Equation 7.8 can be used to describe the origins of the transient response in TR-VSFGS spectra for a given adsorbate-substrate system. This expression can be simplified for both small and large values of $\chi_{NR}^{(2)}$, though the final manifestation will be slightly different for each scenario. This will be described in detail for both ReC0A/TiO_2 (110) and ReC0-Au in the following sections.

7.3. Results and Discussion

7.3.1. ReC0A on TiO_2 (110)

7.3.1.1. Static VSFGS Spectra of ReC0A on TiO_2 (110)

Prior to performing time-resolved measurements, static VSFGS spectra were recorded of ReC0A on TiO_2 (110), as shown in Figure 7.3. As detailed in previous Chapters, ReC0A on TiO_2 displays three CO stretching modes: a symmetric a'(1) stretch at 2040 cm^{-1} and an unresolved band at ~1925 cm^{-1} consisting of an anti-symmetric a" stretch at 1939 cm^{-1} and a symmetric a'(2) stretch at ~ 1910 cm^{-1}.[56] In the VSFGS spectra of ReC0A on TiO_2 (110), only the high frequency a'(1) symmetric stretch appears; as

such, only this portion of the spectrum is shown. Following the description above, we can fit this spectrum according to:

$$I(\omega_{SF}) \propto A_T \left| A_{NR,Au} + \frac{A_1}{\omega_1 - \omega_{IR} + i\Gamma_1} e^{i\phi_1} \right|^2 I_{vis}(\omega_{vis}) I_{IR}(\omega_{IR}) \quad (7.9)$$

where υ_1 refers to the high-frequency a'(1) mode shown in Figure 7.1c. The results of this fitting are shown in Figure 7.3, and the fitting parameters are given in Table 7.1.

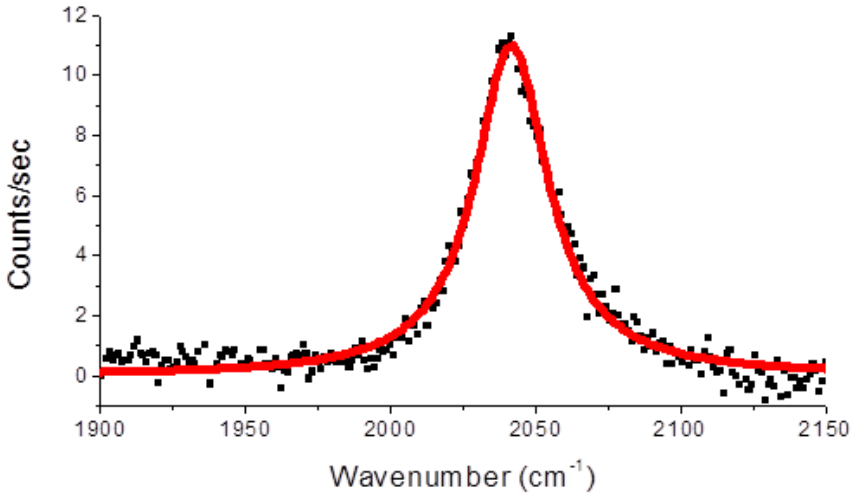

Figure 7.3. Static VSFGS spectrum of ReC0A on TiO_2 (110).

Table 7.1. Fitting parameters for the VSFGS spectrum of ReC0A on TiO_2 (110) shown in Figure 7.3 according to Equation 7.9.

Mode (i)	$A_{NR}^{(2)}$	ϕ_q (rad)	A_q	ω_q (cm^{-1})	Γ_q (cm^{-1})
a'(1) (υ_1)	0.0167	0.0051	51.222	2041.5	15.45

7.3.1.2. Time-resolved VSFGS Spectra of ReC0A on TiO_2 (110)

The vibrational dynamics of ReC0A on TiO_2 (110) were investigated by monitoring the symmetric a'(1) stretch at 2040 cm^{-1} following broadband IR excitation. Briefly, the sample was irradiated by an intense IR pump pulse centered at 2040 cm^{-1}, and its response was monitored by collecting VSFGS spectra at various delay times τ_D after excitation, where τ_D is the time between the pump and probe IR pulses. Spectra were taken at each delay time with and without a preceding pump pulse and used to generate transient VSFGS spectra according to:

$$\Delta I \propto \left(\left| \chi_p^{(2)} \right|^2 - \left| \chi_{un}^{(2)} \right|^2 \right) I_{vis}(\omega_{vis}) I_{IR}(\omega_{IR}) \qquad (7.10)$$

The resulting spectra are shown in Figure 7.4. Spectra at negative delay times (where $\tau_D < 0$) were averaged and subtracted from all spectra at positive delay times in order to improve the signal-to-noise ratio. Transient spectra at early delay times consist of an instantaneous GSB of the symmetric CO stretch at ~2040 cm^{-1} and a corresponding EA at ~2020 cm^{-1}. Spectra at longer delay times show both the recovery of the GSB and the decay of the EA on similar time scales, indicating the relaxation of the molecules back to the ground vibrational state. Their kinetics, which are compared in Figure 7.5, indicate bi-exponential decay of the $\upsilon = 1$ population.

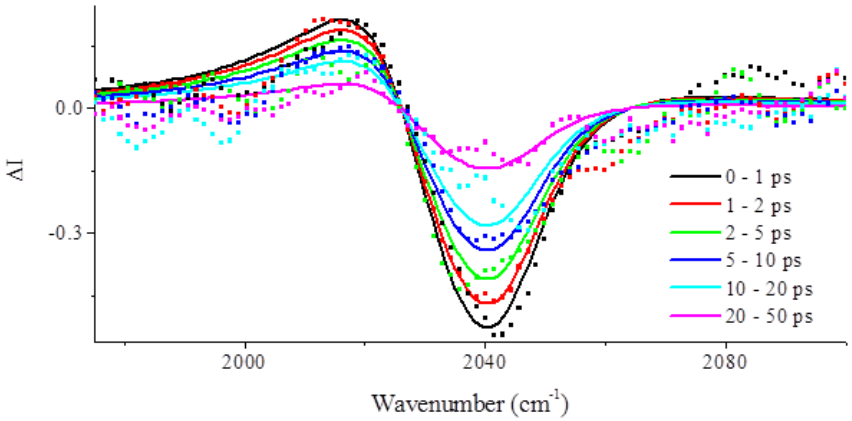

Figure 7.4. Transient VSFGS spectra of the a'(1) mode of ReC0A on TiO_2 (110) (squares) compared with results of the fitting according to Equation 7.11 (solid lines) using the parameters listed in Table 7.2.

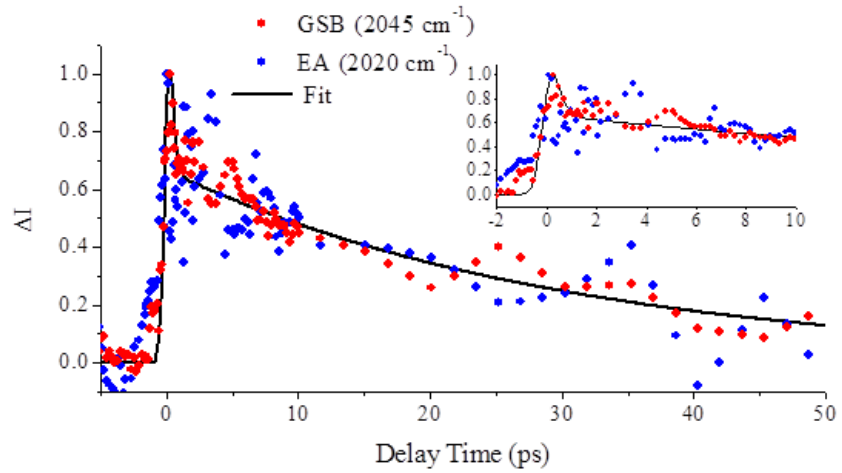

Figure 7.5. Kinetics of the GSB at 2045 cm^{-1} and EA at 2020 cm^{-1} for ReC0A on TiO_2 (110) (circles) compared with the fit to Equation 7.14 (solid line). For comparison purposes, the bleach has been inverted and both kinetic traces have been normalized. Inset shows the kinetics at early time delays.

In order to quantify the spectral features in Figure 7.4, we must consider the explicit expressions for the pumped and unpumped $\chi^{(2)}$. As detailed above, for a sufficiently low IR pump intensity, we can assume that a single vibrational mode is excited to the υ = 1 level. The transient response can thus be modeled according to Equation 7.8, which we can expand for the particular case of ReC0A on TiO_2 (110). In this case, we know from the fit of the static spectrum that $|A_{NR}|$ is negligible. Additionally, from the pumped vs. unpumped spectra, we see an approximately 4% depletion of the GSB. Since the VSFGS signal is proportional to the square of the population difference between the υ = 0 and υ = 1 states, we know that we are only exciting ~1% of the ReC0A molecules. Based on this, we can expand Equation 7.8 and keep only the terms that are proportional the total population N_T (where N_T = 1), yielding:

$$\begin{aligned}\Delta I \propto & \frac{-2A_{01}^2(2N_1(t)+N_1^C(t))}{(\Gamma_{01}^2+(\omega_{01}-\omega_{IR})^2} + \frac{2A_{01}A_{12}\Gamma_{01}\Gamma_{12}N_1(t)}{(\Gamma_{01}^2+(\omega_{01}-\omega_{IR}))(\Gamma_{12}^2+(\omega_{12}-\omega_{IR}))} \\ & + \frac{4A_{01}A_{12}(\omega_{01}-\omega_{IR})(\omega_{12}-\omega_{IR})N_1(t)}{(\Gamma_{01}^2+(\omega_{01}-\omega_{IR}))(\Gamma_{12}^2+(\omega_{12}-\omega_{IR}))} + \frac{2A_{01}A_{01}^C\Gamma_{01}\Gamma_{01}^C N_1^C(t)}{(\Gamma_{01}^2+(\omega_{01}-\omega_{IR}))(\Gamma_{01}^C+(\omega_{01}^C-\omega_{IR}))} \\ & + \frac{4A_{01}A_{01}^C(\omega_{01}-\omega_{IR})(\omega_{01}^C-\omega_{IR})N_1^C(t)}{(\Gamma_{01}^2+(\omega_{01}-\omega_{IR}))(\Gamma_{01}^C+(\omega_{01}^C-\omega_{IR}))} \end{aligned} \quad (7.11)$$

We must also account for frequency-dependent IR intensity term $I_{IR}(\omega_{IR})$ (not shown in Equation 7.11 for brevity) by referencing the spectrum against the response from bare Au, i.e. $|A_{Au}|^2 I(\omega_{IR})I(\omega_{vis})$. Since A_{Au} is considered to be constant, this term can effectively be ignored.

Before the IR pump-VSFGS probe spectra can be fit according to Equation 7.11, several key assumptions must be made. First, as shown in Equation 7.4, the amplitude terms A_{01} and A_{12} are the products of the infrared and Raman transition moments for the particular transition. In the harmonic oscillator approximation, both of these are

proportional to $(j + 1)^{1/2}$.[57-60] Therefore, we find that $A_{12} = 2\,A_{01}$. From the 2DIR spectrum of a similar rhenium bipyridyl complex,[61] we can see that the |100> → |200>, |010> → |110>, and |001> → |101> transitions all have the same frequency; therefore we can also say that $\omega_{01}{}^{C} = \omega_{12}$. We further assume that $A_{01}{}^{C} = A_{01}$ and $\Gamma_{01}{}^{C} = \Gamma_{12}$.

Within this model, the time-dependent populations $N_1(t)$ and $N_1{}^{C}(t)$ can be described by bi-exponential kinetics:

$$N_1(t) = A_1 e^{-t/\tau_1} + A_2 e^{-t/\tau_2} \qquad (7.12)$$

$$N_1^{C}(t) = -A_1 e^{-t/\tau_1} + A_2 e^{-t/\tau_2} \qquad (7.13)$$

where A_i are normalized amplitude constants and τ_i are the corresponding time constants. The overall time evolution of the GSB or EA is thus given by:

$$\Delta I \propto 2N_1(t) + N_1^{C}(t) \propto A_1 e^{-t/\tau_1} + 3A_2 e^{-t/\tau_2} \qquad (7.14)$$

The IR pump-VSFG probe spectra and kinetics were simultaneously fit according to Equations 7.11 and 7.14; the results are shown in Figures 7.4 and 7.5. Overall, the fit shows that the transient spectra can be described very well by the proposed model. We can now see that the GSB results from the first term in Equation 7.11 while the EA results from the other four terms. It should be noted that the EA peak is actually a cross-peak resulting from the spectral overlap of the |000> → |100> transition with transitions 2, 3 and 4 in Figure 7.2. However, the time evolution of both this peak and the GSB are proportional to $2N_1(t) + N_1{}^{C}$, so that their kinetics can be directly compared. The spectral fitting parameters are given in Table 7.2.

The vibrational relaxation kinetics for ReC0A on TiO_2 (110) are also well described by this model, and are characterized by a nearly instrument response-limited rise at $\tau_D = 0$ (τ_0 = ~60 fs) followed by a bi-exponential decay. The decay kinetics are

characterized by a fast initial recovery (τ_1 = 0.23 ps) of 27% of the GSB transient signal, and full recovery of the ground state within tens of picoseconds (τ_2 = 30.35 ps). The fitting parameters are listed in Table 7.3.

Table 7.2. Fitting parameters for the transient VSFGS spectra of ReC0A on TiO_2 (110) shown in Figure 7.4. In the fit we assume $\omega_{01}{}^{C} = \omega_{12}$ and $\Gamma_{01}{}^{C} = \Gamma_{12}$.

Transition	$\omega_{j,j+1}$ (cm^{-1})	$\Gamma_{j,j+1}$ (cm^{-1})
$\upsilon = 0 \rightarrow 1$	2045	14
$\upsilon = 1 \rightarrow 2$	2026	14

Table 7.3. Fitting parameters for the kinetics of ReC0A on TiO_2 (110) shown in Figure 7.5.

τ_0 (ps)	A_1	τ_1 (ps)	A_2	τ_2 (ps)
0.059 (±0.02)	0.27	0.23 (±0.5)	0.24	30.35 (±5)

In discussing the ultrafast component of the kinetics, it must be mentioned that TR-VSFGS suffers from an artifact due to coherent interactions between the pump and probe beams.[62] This interaction causes a coherent transient near $\tau_D = 0$ that is in addition to the transient population term. However, it is also known that if the vibrational dephasing time T_2 is equal to or greater than the IR pump pulsewidth τ_P, this artifact will be negligible. Assuming the transition is homogeneously broadened, we can estimate the effective dephasing time T_2 from the vibrational linewidth [$T_2 = 1/\pi c \Delta\upsilon$]. For ReC0A on TiO_2, this yields T_2 = 0.72 ps, so that the ratio T_2/τ_P = 4.7. In this case, the vibrational

coherence should not have a significant influence on the extracted decay constants and the transient changes can be attributed to the vibrational population relaxation.

There are three primary methods available for vibrational relaxation in this system: intramolecular vibrational energy relaxation (IVR), intermolecular vibrational energy transfer, and direct energy transfer to the substrate. Let us first discuss the latter two possibilities before returning to IVR.

Adsorption studies for the similarly-sized N3 dye on rutile TiO_2 single crystals estimate a full surface coverage between 0.6 – 1.7 molecules/nm^2 compared to an average molecular size of 1 nm^2, indicating dense molecular packing.[63,64] Although the ReC0A molecule is slightly smaller than N3, as it has only one bipyridyl group, we can expect that it also has the potential to pack tightly on the TiO_2 surface, thus allowing for intermolecular vibrational energy transfer. However, this process is known to typically occur on a longer time scale than IVR for large polyatomic molecules such as ReC0A.[65] Therefore, while this mechanism may account for the longer time dynamics, it is unlikely that it may account for the fast vibrational relaxation.

The molecule may also relax by transferring its vibrational energy to the substrate. For semiconductors, this typically involves the emission of multiple substrate phonons. This can occur through direct energy transfer to the surface, to both substrate phonons and other lower frequency modes in the molecule, or first to lower frequency modes of the molecule followed by rapid energy transfer to the substrate. The first two options require the coupling of multiple phonon modes to the symmetric CO stretch, which typically leads to vibrational lifetimes of tens to hundreds of picoseconds.[59,66]

Therefore, while this may account for the slow vibrational relaxation, it cannot account for the fast relaxation component.

In this case, intramolecular vibrational energy relaxation (IVR) is the most likely explanation for the ultrafast (τ_1 = 0.23 ps) relaxation from the υ = 1 state. IVR may also contribute to the slower relaxation component, since there are a large number of available low-frequency vibrational modes to which the excited symmetric CO stretch can transfer its excess energy. This result is consistent with several previous studies on the vibrational relaxation dynamics of metal carbonyl complexes, which also show a bi-exponential decay of the υ = 1 population. In these reports, the ultrafast decay component is attributed to rapid coupling between the different carbonyl stretching modes, while the slower decay component reflects the total vibrational population relaxation time from these coupled modes.[52-54,67,68] Based on these studies, we tentatively assign the ultrafast component to υ-υ coupling between the three CO stretches of ReC0A. The slower (τ_2 = 30.35 ps) component is thus assigned to the vibrational relaxation of the coupled modes, though the exact relaxation mechanism cannot be deduced at this time.

7.3.2. ReC0-Au

7.3.2.1. Static VSFGS Spectra of ReC0-Au

Prior to performing time-resolved measurements, static VSFGS spectra were recorded of ReC0-Au, as shown in Figure 7.6. The ATIR-FTIR spectrum of the ReC0-Au complex is shown for comparison in Figure 7.6c. As detailed above, ReC0 complexes display three CO stretching modes: for ReC0-Au, there is a symmetric a'(1) stretch at 2025 cm^{-1} and an unresolved band at ~1915 cm^{-1} consisting of an anti-symmetric a"

stretch at 1926 cm^{-1} and a symmetric a'(2) stretch at ~ 1890 cm^{-1}.[56] In the VSFGS spectra, the high frequency a'(1) symmetric stretch appears as a peak on the nonresonant Au background (vertical black dashed lined), while the low frequency a'(2) and a" stretches appear as an unresolved dip on the nonresonant Au background (vertical red dashed line). The a'(1) mode is out of phase relative to the a'(2) and a'' modes and they thus show up as positive and negative peaks, respectively. Since the high and low frequency modes are separated by > 100 cm^{-1}, it is difficult to resolve all three modes with sufficient mid-IR intensity within a single IR window, as seen in Figure 7.6a. Therefore, spectra were collected over several spectral windows to ensure adequate mid-IR intensity over the entire spectral range. The IR profile of each spectral window was determined from the nonresonant response of bare Au, as shown in Figure 7.6b.

In order to quantify the nonresonant Au response and the resonant ReC0 features, the spectra in Figure 7.6a can be fit according to Equations 7.1 – 7.3. For the three vibrational modes seen here, we can write:

$$I(\omega_{SF}) \propto A_T \left| A_{NR,Au} + \frac{A_1}{\omega_1 - \omega_{IR} + i\Gamma_1} e^{i\phi_1} + \frac{A_2}{\omega_2 - \omega_{IR} + i\Gamma_2} e^{i\phi_2} + \frac{A_3}{\omega_3 - \omega_{IR} + i\Gamma_3} e^{i\phi_3} \right|^2 I_{vis}(\omega_{vis}) I_{IR}(\omega_{IR}) \quad (7.15)$$

where A_T is a constant, the nonresonant Au response (A_{Au}) is assumed to be flat over the investigated spectral region, and the three CO modes are modeled as Lorentzian functions with amplitude A_i, central frequency ω_i, and linewidth Γ_i; modes 1, 2, and 3 refer to the a'(1), a", and a'(2) modes, respectively. The $e^{i\phi}$ terms denote the phase difference between the resonant and nonresonant contributions, as well as between the different vibrational resonances. The frequency-dependent IR intensity, $I_{IR}(\omega_{IR})$, was determined from the nonresonant response of bare Au.

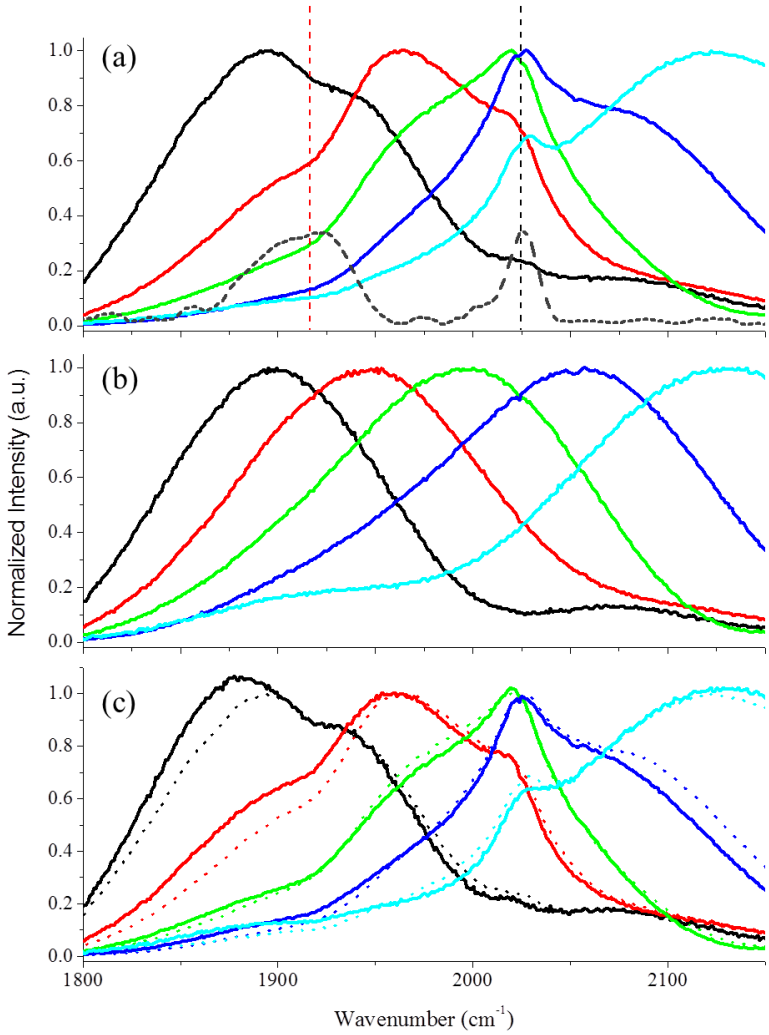

Figure 7.6. (a) Normalized static VSFGS spectra of ReC0-Au recorded with different central IR wavelengths. The a'(1) symmetric stretch is indicated by the vertical black dashed lined, and the asymmetric a" and symmetric a'(2) stretches are indicated by the vertical red dashed line. Also shown is the ATR-FTIR spectrum of the ReC0-Au sample for comparison (gray dashed line). (b) Normalized static VSFGS spectra of Au corresponding to the central IR wavelengths used in (a); corresponding spectral windows are indicated with the same color. (c) Fits (solid lines) to spectra shown in (a) (dashed lines) according to Equation 7.15 using the parameters in Table 7.4.

Table 7.4. Fitting parameters for the ReC0-Au spectra shown in Figure 7.6c according to Equation 7.15.

Mode (i)	A_i	φ_i (rad)	ω_i (cm^{-1})	Γ_i (cm^{-1})
a'(1) (1)	3.2	$\pi/2$	2022	15
a'' (2)	3	$3\pi/2$	1920	25
a'(2) (3)	1.5	$3\pi/2$	1895	25

Equation 7.15 was used to fit the VSFGS spectra of ReC0-Au. Figure 7.6c shows the results the fitting procedure, showing overall good agreement. Any inconsistencies are believed to result from imperfect characterization of the IR profile for each spectral window, which was determined from the response of bare Au. Spectral drift and slight changes in sample position may cause discrepancies in the measured spectra. From the fit, we are able to determine the relative phases for the three resonant modes; the a'(1) mode is $\pi/2$ out of phase with Au, and $3\pi/2$ out of phase with the a'' and a'(2) modes. Knowledge of the phase between these modes and the Au NR response helps to simplify the analysis for the time-resolved study.

The parameters in Table 7.4 can also be used to visualize the ReC0 resonant response ($|\chi_R|^2$) in the absence of a nonresonant background, as seen in Figure 7.7. This representation is useful because it retains the phase information between the three vibrational modes, yet the spectrum is no longer convoluted with the strong Au response. This is in contrast to a VSFGS experiment with no nonresonant background, in which the peaks all appear positive and no relative phase information can be ascertained. The phase information in the former case arises from the cross terms between the resonant and

nonresonant $\chi^{(2)}$ terms when Equation 7.6 is expanded. For simplicity, consider the case of only the a'(1) mode, which is completely separated from the lower frequency modes:

$$I(\omega_{SF}) \propto \left|\chi^{(2)}_{NR,Au} + \chi^{(2)}_{a'(1)} e^{i\phi_{a'(1)}}\right|^2 I_{vis}(\omega_{vis}) I_{IR}(\omega_{IR})$$
$$\propto \left[\left|\chi^{(2)}_{NR,Au}\right|^2 + \left|\chi^{(2)}_{a'(1)}\right|^2 + 2\,\mathrm{Re}\,\chi^{(2)}_{NR,Au}\chi^{(2)}_{a'(1)} e^{i\phi_{a'(1)}}\right] I_{vis}(\omega_{vis}) I_{IR}(\omega_{IR}) \quad (7.16)$$

When there is no nonresonant response (i.e. $\chi_R = 0$), the first and third term of Equation 7.16 go to zero and only the $\left|\chi^{(2)}_{a'(1)}\right|^2$ term remains; thus no phase information can be ascertained. However, when the nonresonant response is equal to or larger than the resonant response, as in the case of ReC0-Au, the cross term dominates over the $\left|\chi^{(2)}_{a'(1)}\right|^2$ term, so the latter can be neglected. Subsequent subtraction of the nonresonant response and normalization by the frequency-dependent IR profile (given by the bare Au spectrum) yields the purely resonant response χ_R.

The resulting normalized, corrected spectrum for ReC0 is shown in Figure 7.7. This spectrum is obtained by removing the Au response from all spectra shown in Figure 7.6a, normalizing with respect to bare Au, and then piecing the spectrum together to ensure sufficient mid-IR intensity over the entire spectral range investigated. This can be compared to the spectrum obtained from Equation 7.15 using the parameters in Table 7.4 when the nonresonant response $|\chi_{NR}|^2$ is subtracted. The two spectra show good agreement, indicating that the relative phases deduced from the fit are valid and the spectra can be accurately described using Equation 7.15. The clear resonant signatures and knowledge of the relative phases provide an avenue for investigating the vibrational dynamics in this system. The symmetric a'(1) stretch at 2025 cm^{-1} is particularly

appealing for this purpose, as it is isolated from the other resonances and can be cleanly separated from the Au background.

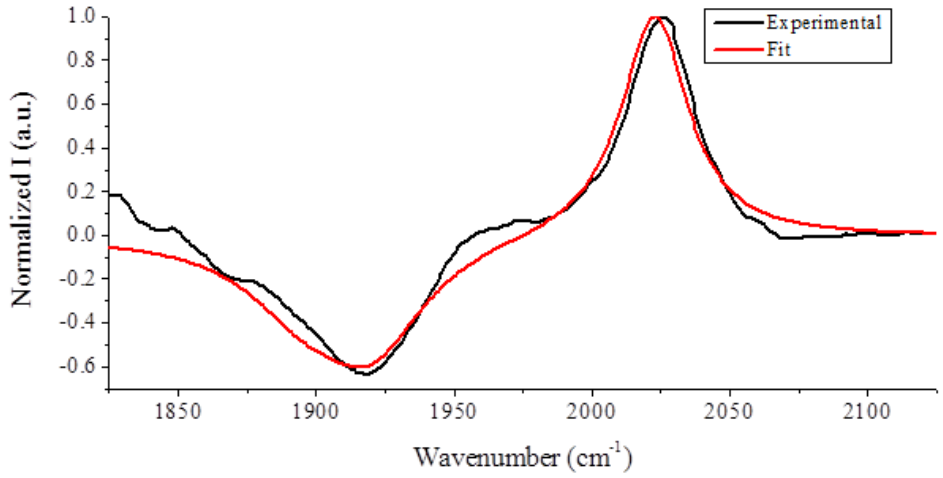

Figure 7.7. Normalized, corrected spectrum of ReC0 obtained from the spectra shown in Figure 7.6a (black line). Also shown is the spectrum obtained from Equation 7.15 using the parameters in Table 7.4 when the nonresonant response $|\chi_{NR}|^2$ is subtracted (red line).

7.3.2.2. Time-resolved VSFGS Spectra of ReC0-Au

The vibrational dynamics of the ReC0-Au system were investigated by monitoring the vibrational relaxation of the symmetric a'(1) stretch at 2025 cm^{-1} following IR excitation. The a'(1) mode was monitored because it is completely separated from the two lower frequency modes, simplifying the IR-pump VSFG-probe spectra and their analysis. Pump-probe spectra were generated according to Equation 7.10; the resulting spectra are shown in Figure 7.8. The spectra at delay time $\tau_D = 0$ have been corrected for the instantaneous response of the gold substrate to the pump pulse,

which has been noted previously.[69,70] Additionally, spectra where $\tau_D < 0$ were averaged and subtracted from all spectra at positive delay times in order to improve the signal-to-noise ratio. At early delay times, the TR-VSFGS spectra consist of an instantaneous GSB of the CO stretch at ~2025 cm^{-1} and a corresponding EA at ~2005 cm^{-1}. Spectra at longer delay times show both the recovery of the GSB and the decay of the EA on similar time scales, indicating the relaxation of the molecules back to the ground vibrational state. Their kinetics are compared in Figure 7.9 and indicate bi-exponential decay of the $\upsilon = 1$ population.

Once again, in order to quantify the spectral features in Figure 7.8, we must consider the explicit expressions for the pumped and unpumped $\chi^{(2)}$. In the case of ReC0-Au, we can discern from the fit of the static spectra that the nonresonant response of Au is much larger than the resonant response from ReC0. In this case, after expansion of Equation 7.8, only terms containing $A_{NR,Au}$ will dominate. We have also established that the phase difference between gold and the a'(1) mode is $\phi = \pi/2$. We can further assume that the excited state a'(1) mode is nearly parallel with the ground state a'(1) mode, and will therefore have the same phase. If we expand Equation 7.8 and include this information, we find that three terms dominate over all others:

$$\Delta I \propto 2A_{NR}\left[\frac{-A_{01}\Gamma_{01}(2N_1(t)+N_1^c(t))}{(\omega_{01}-\omega_{IR})^2+\Gamma_{01}^{\ 2}}+\frac{A_{12}\Gamma_{12}N_1(t)}{(\omega_{12}-\omega_{IR})^2+\Gamma_{12}^{\ 2}}+\frac{A_{01}^C\Gamma_{01}^C N_1^C(t)}{(\omega_{01}^C-\omega_{IR})^2+\Gamma_{01}^{C\,2}}\right] \tag{7.17}$$

Equation 7.17 has omitted the frequency-dependent intensity terms which must be eliminated through reference to a Au substrate, i.e. $|A_{Au}|^2 I(\omega_{IR})\, I(\omega_{vis})$.

In order to fit the IR pump-VSFGS probe spectra according to Equation 7.17, we can employ the same key assumptions as for ReC0A on TiO_2: $A_{12} = 2A_{01}$, $\omega_{01}^{\ C} = \omega_{12}$,

$A_{01}{}^{C} = A_{01}$ and $\Gamma_{01}{}^{C} = \Gamma_{12}$. Additionally, similar to ReC0A on TiO_2, we can use this model to describe the bi-exponential time-dependent populations $N_1(t)$ and $N_1{}^{C}(t)$. Once again, the overall time evolution of the GSB or EA is given by Equation 7.14.

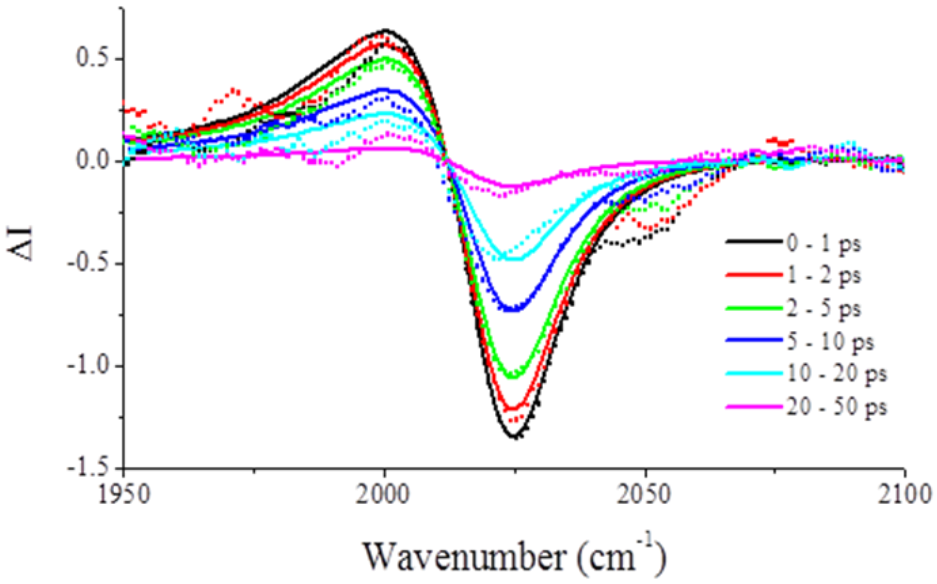

Figure 7.8. Transient VSFGS spectra of the a'(1) mode of ReC0-Au (squares) compared with results of the fitting according to Equation 7.17 (solid lines) using the parameters listed in Table 7.5.

Table 7.5. Fitting parameters for the transient VSFGS spectra of ReC0-Au shown in Figure 7.8 according to Equation 7.17. In the fit we assume $\omega_{01}{}^{C} = \omega_{12}$ and $\Gamma_{01}{}^{C} = \Gamma_{12}$.

Transition	$\omega_{j,j+1}$ (cm^{-1})	$\Gamma_{j,j+1}$ (cm^{-1})
$\upsilon = 0 \rightarrow 1$	2023	13.5
$\upsilon = 1 \rightarrow 2$	2009	22

The IR pump-VSFG probe spectra and kinetics were simultaneously fit according to Equations 7.17 and 7.14; the results are shown in Figures 7.8 and 7.9. Overall, the fit shows that the transient spectra can be described very well by the proposed model. We can now see that the GSB results from the first term in Equation 7.17, while the EA results from the second and third terms. The spectral fitting parameters are given in Table 7.5. The vibrational relaxation kinetics for ReC0-Au are well described by a nearly instrument response-limited rise at $\tau_D = 0$ (τ_0 = ~50 – 60 fs) followed by a bi-exponential decay. The decay kinetics are characterized by a fast initial recovery (τ_1 = 0.26 ps) of 21% of the transient GSB signal, and full recovery of the ground state within tens of picoseconds (τ_2 = 14.8 ps). The fitting parameters are listed in Table 7.6.

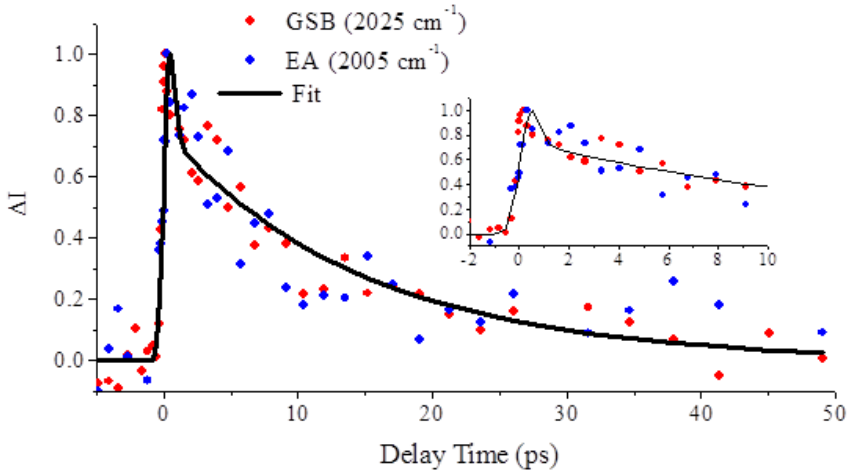

Figure 7.9. Kinetics of the GSB at 2025 cm^{-1} and EA at 2005 cm^{-1} for ReC0-Au compared with the fit to Equation 7.14. For comparison purposes, the bleach has been inverted and both kinetic traces have been normalized. Inset shows the kinetics at early time delays.

Table 7.6. Fitting parameters for the kinetics shown in Figure 7.9 according to Equation 7.14 for ReC0-Au.

τ_0 (ps)	A_1	τ_1 (ps)	A_2	τ_2 (ps)
0.055 (±0.02)	0.21	0.26 (±0.1)	0.26	14.8 (±6)

Analogous to the case for ReC0A on TiO_2, we can consider three mechanisms for vibrational relaxation in this system: intramolecular vibrational energy relaxation (IVR), intermolecular vibrational energy transfer, and direct energy transfer to the substrate.

For ReC0-Au, the ReC0 complex is not directly adsorbed on the surface, but rather is tethered to the Au surface through undecane linkers. A similar procedure was recently reported for a ReC0 complex tethered to silane where the packing density was estimated to be ~1.8 molecules/nm^2,[71] similar to our estimate for ReC0A on TiO_2. The system is thus also available for intermolecular vibrational energy transfer, though this mechanism may only account for the longer time dynamics.

Vibrational energy transfer to metal substrates may occur either through the generation of electron-hole pairs (EHP) or through the emission of multiple substrate phonons. Generation of EHP typically dominates other relaxation pathways, so that in cases where EHP generation has been proposed as the primary decay mechanism, the systems exhibit single exponential kinetics.[10,12,17] This decay pathway is therefore incongruent with our bi-exponential kinetics. Phonon emission may occur through direct energy transfer to the surface, to both substrate phonons and other lower frequency modes in the molecule, or first to lower frequency modes of the molecule followed by rapid energy transfer to the substrate. These options all require the coupling of multiple

modes to the symmetric CO stretch, which is associated with vibrational lifetimes of tens to hundreds of picoseconds. Therefore, while this may account for the slow vibrational relaxation, it cannot account for the fast relaxation component.

Considering this, IVR is again the most likely explanation for the ultrafast relaxation and may also be responsible for the slower component. We again tentatively assign the ultrafast (τ_1 = 0.26 ps) component to υ-υ coupling between the three CO stretches of ReC0A and the slower (τ_2 = 14.8 ps) component to the vibrational relaxation of the coupled modes. The exact mechanism for the slow relaxation cannot be deduced at this time, and may have contributions from IVR, intermolecular energy transfer, and/or energy transfer to the substrate.

7.3.3. Transient IR-Pump IR-Probe Spectra of ReC0A in DMF

In order to distinguish between the various vibrational relaxation mechanisms discussed thus far, the vibrational dynamics of ReC0A in solution (DMF) were also investigated. Since this system has a very different local environment compared to ReC0A on TiO_2 and ReC0-Au and is not coordinated in any way to a semiconductor or metal surface, a comparison of the dynamics for these three systems may shed light on the precise decay mechanisms at play.

The vibrational dynamics of ReC0A in DMF were monitored using standard IR-pump IR-probe transient absorption techniques. Briefly, the sample was irradiated by an intense IR pump pulse centered at 2025 cm^{-1}, and its response was monitored by a subsequent IR probe pulse at various delay times τ_D after excitation, where τ_D is the time

between the pump and probe IR pulses. Spectra were taken at delay times τ_D with and without a preceding pump pulse and used to generate transient VSFGS spectra.

Typically, transient spectra are generated via:

$$\Delta I \propto -\log\left[\frac{I_{pumped}}{I_{unpumped}}\right] \propto A_{pumped} - A_{unpumped} \qquad (7.18)$$

The transient signal is thus directly proportional to the change in absorbance (ΔA or ΔOD), which in turn is proportional to the population of the ground and excited states ($A_i = \sigma l N_i$).

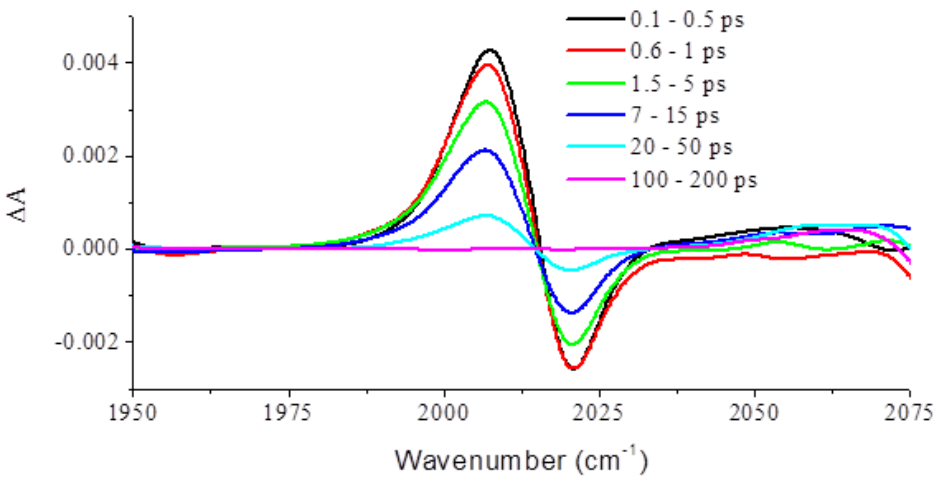

Figure 7.10. Transient IR-pump IR-probe spectra of the a'(1) mode of ReC0A in DMF at indicated delay times.

Figure 7.10 shows the transient spectra of ReC0A in DMF after broadband IR excitation centered at 2025 cm^{-1}. Early time transient spectra are characterized by the instantaneous bleach of the ground state CO stretch at ~2020 cm^{-1} and the resultant

excited-state absorption (EA) at ~2005 cm^{-1}. Spectra at longer delay times show a recovery of the bleach component and a corresponding decay of the EA on similar time scales, indicating the relaxation of the molecules back to the ground vibrational state. Figure 7.11 compares their kinetics, which once again indicate bi-exponential decay of the $\upsilon = 1$ population.

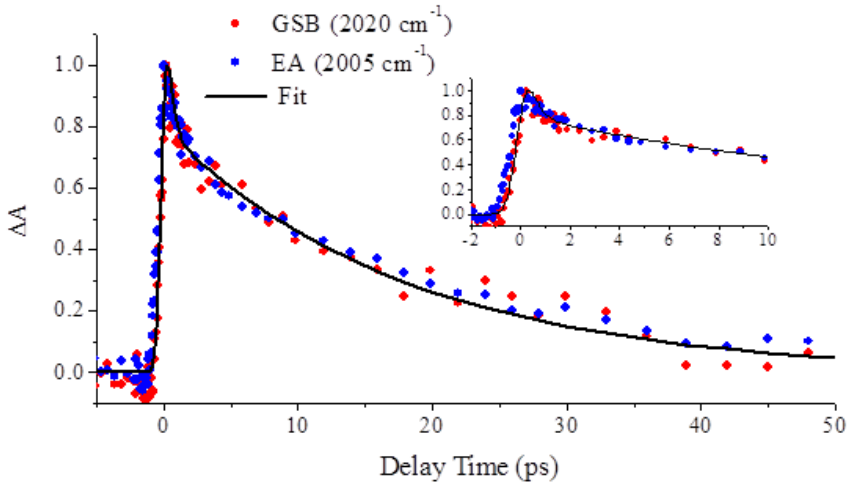

Figure 7.11. Kinetics of the EA at 2005 cm^{-1} (red line) and GSB at 2020 cm^{-1} (black line) compared with the fit to Equation 7.14. For comparison purposes, the bleach has been inverted and both kinetic traces have been normalized. Inset shows early time delays.

Table 7.7. Fitting parameters for the kinetics shown in Figure 7.11 according to Equation 7.14 for ReC0A in DMF.

τ_0 (ps)	A_1	τ_1 (ps)	A_2	τ_2 (ps)
0.042 (±0.02)	0.22	0.33 (±0.4)	0.26	18.0 (±4)

To quantify the vibrational relaxation process, the GSB and EA kinetics were simultaneously fit to the multi-exponential in Equation 7.14. The results of the fitting are seen in Figure 7.11, and the parameters are given in Table 7.7. Similar to ReC0A on TiO_2 and ReC0-Au, the vibrational relaxation kinetics for ReC0A in DMF are characterized by a nearly instrument response-limited rise at $\tau_D = 0$ (τ_0 = ~40 – 50 fs), followed by a bi-exponential decay. The decay is characterized by a fast initial recovery (τ_1 = 0.33 ps) of 22% of the GSB transient signal, and full recovery of the ground state within tens of picoseconds (τ_2 = 18.0 ps).

Since ReC0A is in solution in this experiment, vibrational relaxation may only occur through IVR and intermolecular vibrational energy transfer. According to our previous argument, we tentatively assign the ultrafast decay to υ-υ coupling between the three CO stretches of ReC0A and the slower decay to the vibrational relaxation of the coupled modes. In this case, the slower decay may only be attributed to IVR and intermolecular vibrational energy transfer.

7.3.4. Comparison of All Three Systems

In order to distinguish between the various decay mechanisms discussed so far, the vibrational dynamics of ReC0A were compared for all three systems. Figure 7.12 compares the normalized experimental and fitted kinetic traces for the GSB of the a'(1) mode for ReC0A in DMF, ReC0A on TiO_2 (110), and ReC0-Au. For all three systems, the GSB is linearly proportional to the sum population $2N_1(t) + N_1^C(t)$ and therefore the kinetics should be directly comparable. The determined time constants for each system are reproduced in Table 7.8 for easier comparison. All three systems show similar

kinetics, with a smaller but appreciable ultrafast component (< 1 ps) followed by larger, slower recovery component (tens of picoseconds).

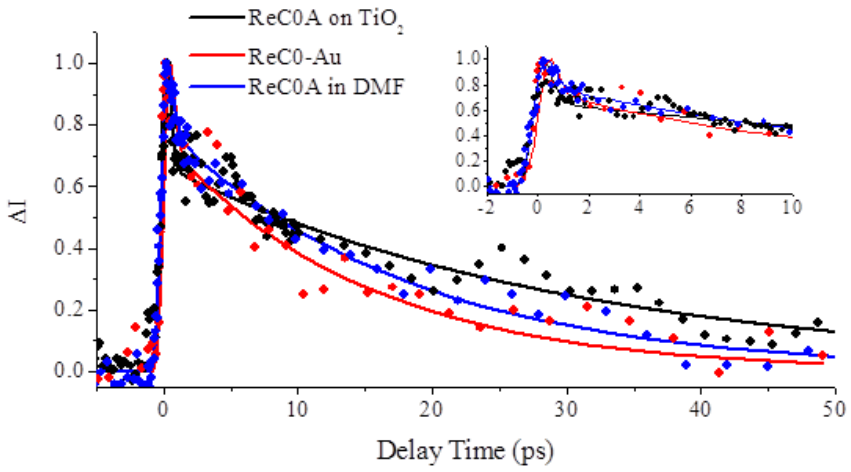

Figure 7.12. Normalized and inverted GSB kinetics for ReC0A on TiO_2 (110), ReC0-Au, and ReC0A in DMF. Squares represent experimental data; lines represent fits. Inset shows the kinetics at early delay times.

Table 7.8. Fitting parameters for the kinetics of ReC0A on TiO_2 (110), ReC0-Au, and ReC0A in DMF.

Substrate/Solvent	τ_0 (ps)	A_1	τ_1 (ps)	A_2	τ_2 (ps)
TiO_2	0.059 (±0.02)	0.27	0.23 (±0.5)	0.24	30.35 (±5)
Au	0.055 (±0.02)	0.21	0.26 (±0.1)	0.26	14.8 (±6)
DMF	0.042 (±0.02)	0.22	0.33 (±0.4)	0.26	18.0 (±4)

The time scale of the ultrafast relaxation is the same for all three systems within the error of the fit, indicating that the mechanism for the ultrafast decay is most likely the same. Since these three systems have different local environments but similar molecular structures, this supports the previous conclusion that this component can be attributed to υ-υ coupling between the three carbonyl stretching modes shown in Figure 1c, as has been observed for a number of other metal carbonyl systems.[52-54,67,68]. The slower decay component is thus assigned to the overall relaxation of the coupled CO stretches.

Interestingly, the a'(1) mode exhibits a significantly longer slow component for ReC0A on TiO_2 compared to ReC0-Au and ReC0A in DMF. However, the long-time kinetics for ReC0-Au and ReC0A in DMF are nearly identical, implying that their relaxation pathways are the same. This rules out energy transfer to the substrate for ReC0-Au, since this pathway is not available for ReC0A in DMF. Furthermore, due to the very different local environments, we expect that the intermolecular relaxation rate would be different in the two systems; the similar kinetics therefore suggest that the slow decay of the N_1 population is due to intramolecular vibratonal energy transfer (IVR).

In this context, the different long-time kinetics for ReC0A on TiO_2 may be due to interactions with the substrate or a different IVR rate. We expect ReC0A may have stronger interactions with the substrate compared to ReC0-Au due to its closer proximity, since the ReC0A molecule is separated from the Au surface by ~10 A in ReC0-Au. However, if energy transfer to TiO_2 played a significant role for this system, we would expect the decay rate to *increase* rather than decrease; therefore, we can also rule out energy transfer to the substrate for ReC0A on TiO_2. The different long-time kinetics must

therefore be due to different IVR rates for this system compared to ReC0-Au and ReC0A in DMF.

One explanation is that electronic interactions between ReC0A and TiO_2 influence the vibrational lifetime in this system. This interaction is evidenced by the difference in the ground and excited state vibrational frequencies of the a'(1) mode for ReC0A/TiO_2 compared to ReC0-Au and ReC0A in DMF. In ReC0-Au and ReC0A in DMF, the $\upsilon = 0 \rightarrow 1$ transition of the a'(1) mode occurs at ~2020 – 2025 cm^{-1}, compared to ~2045 cm^{-1} for ReC0A on TiO_2. The excited state ($\upsilon = 1 \rightarrow 2$) transitions are similarly shifted. The higher vibrational frequencies for ReC0A on TiO_2 indicate a reduced electron density on the rhenium atom. This is caused by electron donation from the molecule to bonded Ti atoms, thereby withdrawing electrons from the metal center. This diminishes the metal's ability to undergo π back-bonding to the π* antibonding molecular orbitals of the CO ligands. The reduced electron density in these orbitals leads to an increased vibrational frequency and a longer vibrational lifetime.[72,73]

This effect has been well-documented for numerous metalloporphyrin complexes,[72,73] and more recently reported for a ReC0-type complex.[71] In the metalloporphyrin complexes, vibrational relaxation was attributed to intramolecular anharmonic coupling from the CO ligand to the metalloporphyrin via the metalloporphyrin-CO π-bonds, rather than the metal-CO σ-bonds. Altering the degree of back-bonding from the metal to the CO affects both the CO vibrational frequency and the strength of the anharmonic coupling. Specifically, increased back-bonding decreases the CO bond order, thus lowering the vibrational frequency, and simultaneously increases the degree of anharmonic coupling, thus shortening the vibrational lifetime. We propose that

a similar effect is seen for the ReC0-type complexes studied here. The blue-shift in the vibrational frequencies for ReC0A on TiO_2 indicates a concurrent weakening of the anharmonic coupling between the symmetric CO stretch and the Re-bipyridyl complex, which leads to a longer vibrational lifetime compared to the ReC0-Au and ReC0A in DMF. We expect that all three CO stretching modes would be affected equally by the reduced electron density at the metal atom, and thus would not expect the coupling between these modes to be affected. This explains the similar ultrafast component but different long-time kinetics for the three systems.

7.4. Summary

Broadband time-resolved vibrational sum frequency generation spectroscopy has been used to monitor the vibrational relaxation dynamics for ReC0 complexes on Au and TiO_2 surfaces. IR transient absorption spectroscopy was used to monitor the vibrational relaxation of the excited a'(1) mode of ReC0A in DMF in order to develop a more complete understanding of the vibrational dynamics in these systems. All three systems exhibited bi-exponential relaxation from the $\upsilon = 1$ state consisting of an ultrafast (sub-picosecond) initial relaxation followed by a complete recovery of the ground vibrational state within tens of picoseconds. The ultrafast decay is assigned to rapid υ-υ coupling between the three CO stretching modes, while the slower decay is assigned to the total vibrational population relaxation from the coupled CO modes. The coupled population relaxation back to the $\upsilon = 0$ state is facilitated by multi-quantum vibrational energy transfer to other modes within the molecule.

Although all three systems exhibited similar ultrafast decay times, the excited a'(1) mode persisted for significantly longer for ReC0A on TiO_2 compared to ReC0-Au and ReC0A in DMF. This is attributed to electronic interactions between ReC0A and TiO_2; specifically, the adsorption of ReC0A on TiO_2 results in diminished electron density on the rhenium center, which reduces the metal's π back-bonding to the CO π* orbital, thereby increasing the a'(1) vibrational frequency. This simultaneously reduces the anharmonic coupling between the a'(1) mode and the Re-bipyridyl complex, thereby increasing the vibrational lifetime. These results indicate that coordination of the catalyst to the electrode surface may affect the mechanism for vibrational relaxation at the catalytic rhenium center for ReC0A on TiO_2, but not for the ReC0-Au system. This is likely due to the long distance between ReC0A and the Au surface (~10 A) in the latter case. This may have interesting implications for the catalytic activity of the ReC0A complex on TiO_2, as decreasing the degree of π back-bonding increases the CO bond order but simultaneously decreases the strength of the Re-C bond.[71,74]

7.5. References

(1) Arnolds, H.; Bonn, M. *Surf Sci Rep* **2010**, *65*, 45.

(2) Gadzuk, J. W. *Physical Review B* **1981**, *24*, 1651.

(3) Wodtke, A. M.; Tully, J. C.; Auerbach, D. J. *International Reviews in Physical Chemistry* **2004**, *23*, 513.

(4) Tully, J. C. *Annual Review of Physical Chemistry* **2000**, *51*, 153.

(5) Zhuang, X.; Miranda, P. B.; Kim, D.; Shen, Y. R. *Physical Review B* **1999**, *59*, 12632.

(6) Lambert, A. G.; Davies, P. B.; Neivandt, D. J. *Applied Spectroscopy Reviews* **2005**, *40*, 103.

(7) Wang, H. F.; Gan, W.; Lu, R.; Rao, Y.; Wu, B. H. *International Reviews in Physical Chemistry* **2005**, *24*, 191.

(8) Rao, Y.; Comstock, M.; Eisenthal, K. B. *Journal of Physical Chemistry B* **2006**, *110*, 1727.

(9) Morin, M.; Jakob, P.; Levinos, N. J.; Chabal, Y. J.; Harris, A. L. *Journal of Chemical Physics* **1992**, *96*, 6203.

(10) Morin, M.; Levinos, N. J.; Harris, A. L. *Journal of Chemical Physics* **1992**, *96*, 3950.

(11) Harris, A. L.; Rothberg, L.; Dhar, L.; Levinos, N. J.; Dubois, L. H. *Journal of Chemical Physics* **1991**, *94*, 2438.

(12) Harris, A. L.; Levinos, N. J.; Rothberg, L.; Dubois, L. H.; Dhar, L.; Shane, S. F.; Morin, M. *J Electron Spectrosc* **1990**, *54*, 5.

(13) Harris, A. L.; Rothberg, L.; Dubois, L. H.; Levinos, N. J.; Dhar, L. *Phys Rev Lett* **1990**, *64*, 2086.

(14) Harris, A. L.; Levinos, N. J. *Journal of Chemical Physics* **1989**, *90*, 3878.

(15) Sass, M.; Lobau, J.; Lettenberger, M.; Laubereau, A. *Chemical Physics Letters* **1999**, *311*, 13.

(16) Graener, H.; Laubereau, A. *Chemical Physics Letters* **1987**, *133*, 378.

(17) Matranga, C.; Wehrenberg, B. L.; Guyot-Sionnest, P. *J. Phys. Chem. B* **2002**, *106*, 8172.

(18) Matranga, C.; Guyot-Sionnest, P. *J. Chem. Phys.* **2000**, *112*, 7615.

(19) Guyotsionnest, P.; Lin, P. H.; Hiller, E. M. *Journal of Chemical Physics* **1995**, *102*, 4269.

(20) Guyotsionnest, P.; Tadjeddine, A. *Chemical Physics Letters* **1990**, *172*, 341.

(21) Han, X.; Balgar, T.; Hasselbrink, E. *Journal of Chemical Physics* **2009**, *130*.

(22) Han, X.; Lass, K.; Hasselbrink, E. *Journal of Physics-Condensed Matter* **2008**, *20*.

(23) Lass, K.; Han, X.; Hasselbrink, E. *Surface Science* **2006**, *600*, 4275.

(24) Hommel, E. L.; Ma, G.; Allen, H. C. *Analytical Sciences* **2001**, *17*, 1325.

(25) Zhang, Z.; Piatkowski, L.; Bakker, H. J.; Bonn, M. *Nat Chem* **2011**, *3*, 888.

(26) Ghosh, A.; Smits, M.; Bredenbeck, J.; Dijkhuizen, N.; Bonn, M. *Rev Sci Instrum* **2008**, *79*.

(27) Vanselous, H.; Dewan, S.; Isaienko, O.; Borguet, E. *Abstracts of Papers of the American Chemical Society* **2011**, *242*.

(28) Nihonyanagi, S.; Eftekhari-Bafrooei, A.; Borguet, E. *Journal of Chemical Physics* **2011**, *134*.

(29) Eftekhari-Bafrooei, A.; Borguet, E. *Journal of the American Chemical Society* **2009**, *131*, 12034.

(30) Eftekhari-Bafrooei, A.; Nihonyanagi, S.; Borguet, E. *Springer Series Chem* **2009**, *92*, 361.

(31) Rao, Y.; Turro, N. J.; Eisenthal, K. B. *Journal of Physical Chemistry C* **2010**, *114*, 17703.

(32) Hawecker, J.; Lehn, J. M.; Ziessel, R. *J Chem Soc Chem Comm* **1984**, 328.

(33) Hawecker, J.; Lehn, J. M.; Ziessel, R. *Helv Chim Acta* **1986**, *69*, 1990.

(34) Juris, A.; Campagna, S.; Bidd, I.; Lehn, J. M.; Ziessel, R. *Inorganic Chemistry* **1988**, *27*, 4007.

(35) Yam, V. W. W.; Lau, V. C. Y.; Cheung, K. K. *Organometallics* **1995**, *14*, 2749.

(36) Hayashi, Y.; Kita, S.; Brunschwig, B. S.; Fujita, E. *Journal of the American Chemical Society* **2003**, *125*, 11976.

(37) Fujita, E. H., Y.; Kita, S.; Brunschwig, B. S. In *7th International Conference on Carbon Dioxide Utilization*; Sang-Eon Park, J.-S. C., Kyu-Wan Lee, Ed.; Elsevier: Seoul, Korea, 2004.

(38) Fujita, E.; Muckerman, J. T. *Inorg Chem* **2004**, *43*, 7636.

(39) Takeda, H.; Koike, K.; Inoue, H.; Ishitani, O. *Journal of the American Chemical Society* **2008**, *130*, 2023.

(40) Smieja, J. M.; Kubiak, C. P. *Inorg Chem* **2010**, *49*, 9283.

(41) Kumar, B.; Smieja, J. M.; Sasayama, A. F.; Kubiak, C. P. *Chem Commun* **2012**, *48*, 272.

(42) Kumar, B.; Smieja, J. M.; Kubiak, C. P. *Journal of Physical Chemistry C* **2010**, *114*, 14220.

(43) Otoole, T. R.; Margerum, L. D.; Westmoreland, T. D.; Vining, W. J.; Murray, R. W.; Meyer, T. J. *J Chem Soc Chem Comm* **1985**, 1416.

(44) Christensen, P.; Hamnett, A.; Muir, A. V. G.; Timney, J. A.; Higgins, S. *Journal of the Chemical Society-Faraday Transactions* **1994**, *90*, 459.

(45) Cecchet, F.; Alebbi, M.; Bignozzi, C. A.; Paolucci, F. *Inorganica Chimica Acta* **2006**, *359*, 3871.

(46) Cheung, K. C.; Guo, P.; So, M. H.; Lee, L. Y. S.; Ho, K. P.; Wong, W. L.; Lee, K. H.; Wong, W. T.; Zhou, Z. Y.; Wong, K. Y. *J Organomet Chem* **2009**, *694*, 2842.

(47) O'Regan, B.; Gratzel, M. *Nature* **1991**, *353*, 737.

(48) Kamat, P. V.; Meisel, D. *Current Opinion in Colloid & Interface Science* **2002**, *7*, 282.

(49) Adams, D. M.; Brus, L.; Chidsey, C. E. D.; Creager, S.; Creutz, C.; Kagan, C. R.; Kamat, P. V.; Lieberman, M.; Lindsay, S.; Marcus, R. A.; Metzger, R. M.; Michel-Beyerle, M. E.; Miller, J. R.; Newton, M. D.; Rolison, D. R.; Sankey, O.; Schanze, K. S.; Yardley, J.; Zhu, X. *Journal of Physical Chemistry B* **2003**, *107*, 6668.

(50) Gratzel, M. *MRS Bulletin* **2005**, *30*, 23.

(51) Prezhdo, O. V.; Duncan, W. R.; Prezhdo, V. V. *Accounts of Chemical Research* **2008**, *41*, 339.

(52) Beckerle, J. D.; Casassa, M. P.; Cavanagh, R. R.; Heilweil, E. J.; Stephenson, J. C. *Chemical Physics* **1992**, *160*, 487.

(53) Tokmakoff, A.; Sauter, B.; Fayer, M. D. *Journal Of Chemical Physics* **1994**, *100*, 9035.

(54) Yan, S. X.; Seidel, M. T.; Zhang, Z. Y.; Leong, W. K.; Tan, H. S. *Journal of Chemical Physics* **2011**, *135*.

(55) Bredenbeck, J.; Helbing, J.; Hamm, P. *Journal of Chemical Physics* **2004**, *121*, 5943.

(56) Asbury, J. B.; Wang, Y.; Lian, T. *Bull. Chem. Soc. Japan* **2002**, *75*, 973.

(57) Guyotsionnest, P. *Phys Rev Lett* **1991**, *67*, 2323.

(58) Hirose, C.; Akamatsu, N.; Domen, K. *J. Chem. Phys.* **1992**, *96*, 997.

(59) Chin, R. P.; Blase, X.; Shen, Y. R.; Louie, S. G. *Europhys Lett* **1995**, *30*, 399.

(60) Bandara, A.; Kubota, J.; Onda, K.; Wada, A.; Kano, S. S.; Domen, K.; Hirose, C. *Surface Science* **1999**, *427-28*, 331.

(61) Cervetto, V.; Helbing, J.; Bredenbeck, J.; Hamm, P. *Journal of Chemical Physics* **2004**, *121*, 5935.

(62) Harris, A. L.; Rothberg, L. *Journal of Chemical Physics* **1991**, *94*, 2449.

(63) Lu, Y. F.; Choi, D. J.; Nelson, J.; Yang, O. B.; Parkinson, B. A. *Journal of the Electrochemical Society* **2006**, *153*, E131.

(64) Katoh, R.; Yaguchi, K.; Murai, M.; Watanabe, S.; Furube, A. *Chemical Physics Letters* **2010**, *497*, 48.

(65) Wondrazek, F.; Seilmeier, A.; Kaiser, W. *Chemical Physics Letters* **1984**, *104*, 121.

(66) Guyotsionnest, P.; Dumas, P.; Chabal, Y. J. *J Electron Spectrosc* **1990**, *54*, 27.

(67) Tokmakoff, A.; Sauter, B.; Kwok, A. S.; Fayer, M. D. *Chemical Physics Letters* **1994**, *221*, 412.

(68) Golonzka, O.; Khalil, M.; Demirdoven, N.; Tokmakoff, A. *Journal of Chemical Physics* **2001**, *115*, 10814.

(69) Sun, C. K.; Vallee, F.; Acioli, L. H.; Ippen, E. P.; Fujimoto, J. G. *Physical Review B* **1994**, *50*, 15337.

(70) Guo, C. L.; Rodriguez, G.; Taylor, A. J. *Phys Rev Lett* **2001**, *86*, 1638.

(71) Rosenfeld, D. E.; Gengeliczki, Z.; Smith, B. J.; Stack, T. D. P.; Fayer, M. D. *Science* **2011**, *334*, 634.

(72) Hill, J. R.; Ziegler, C. J.; Suslick, K. S.; Dlott, D. D.; Rella, C. W.; Fayer, M. D. In *J. Phys. Chem.* 1996; Vol. 100, p 18023.

(73) Dlott, D. D.; Fayer, M. D.; Hill, J. R.; Rella, C. W.; Suslick, K. S.; Ziegler, C. J. In *J. Am. Chem. Soc.* 1996; Vol. 118, p 7853.

(74) Hocking, R. K.; Hambley, T. W. *Organometallics* **2007**, *26*, 2815.